2007-03

Spread spectrum signal characteristic estimation using exponential averaging and an ad-hoc chip rate estimator

Weber, John Baltzer

Monterey California. Naval Postgraduate School

NAVAL POSTGRADUATE SCHOOL

MONTEREY, CALIFORNIA

DISSERTATION

SPREAD SPECTRUM SIGNAL CHARACTERISTIC ESTIMATION USING EXPONENTIAL AVERAGING AND AN AD-HOC CHIP RATE ESTIMATOR

by

John Baltzer Weber

March 2007

Dissertation Supervisor: Clark Robertson

Approved for public release; distribution is unlimited

THIS PAGE INTENTIONALLY LEFT BLANK

REPORT DOCUMENTATION PAGE			Form Approved OMB No. 0704-0188
Public reporting burden for this collection of information is estimated to average 1 hour per response, including the time for reviewing instruction, searching existing data sources, gathering and maintaining the data needed, and completing and reviewing the collection of information. Send comments regarding this burden estimate or any other aspect of this collection of information, including suggestions for reducing this burden, to Washington headquarters Services, Directorate for Information Operations and Reports, 1215 Jefferson Davis Highway, Suite 1204, Arlington, VA 22202-4302, and to the Office of Management and Budget, Paperwork Reduction Project (0704-0188) Washington DC 20503.			
1. AGENCY USE ONLY ***(Leave blank)***	**2. REPORT DATE** March 2007	**3. REPORT TYPE AND DATES COVERED** Dissertation	
4. TITLE AND SUBTITLE: Spread Spectrum Signal Characteristic Estimation Using Exponential Averaging and an AD-Hoc Chip rate Estimator			**5. FUNDING NUMBERS**
6. AUTHOR(S) John Baltzer Weber			
7. PERFORMING ORGANIZATION NAME(S) AND ADDRESS(ES) Naval Postgraduate School Monterey, CA 93943-5000			**8. PERFORMING ORGANIZATION REPORT NUMBER**
9. SPONSORING / MONITORING AGENCY NAME(S) AND ADDRESS(ES) N/A			**10. SPONSORING / MONITORING AGENCY REPORT NUMBER**
11. SUPPLEMENTARY NOTES The views expressed in this thesis are those of the author and do not reflect the official policy or position of the Department of Defense or the U.S. Government.			
12a. DISTRIBUTION / AVAILABILITY STATEMENT Approved for public release; distribution is unlimited			**12b. DISTRIBUTION CODE**

13. ABSTRACT ***(maximum 200 words)***

This dissertation investigates two methods of spread spectrum (SS) signal characteristic estimation for the two principle types of SS systems, frequency-hopped (FH) and direct sequence SS. The exponential averaging detector is used to detect and estimate the hopped frequencies of a SS-FH signal in the presence of interference signals as well as additive-white-Gaussian-noise (AWGN). The detection method provides an estimate of the AWGN plus inference spectrum using exponential averaging and then generates an estimate of the desired signal spectrum by combining the estimated AWGN plus interference spectrum with the composite (desired signal plus interference plus AWGN) spectrum. Finally, this dissertation evaluates the detector's performance as a function of the exponential coefficient, the combining method, the probability of false alarm, signal-to-AWGN ratio, and signal-to-interference ratio.

The second method of SS signal characteristic estimation uses a digital ad-hoc chip rate estimator (ACRE). The ACRE is used to estimate the chip rate of a half-sine pulse shaped SS direct-sequence signal. The ACRE is explained in relation to its similarities and contrasts to the chip rate detector. The components and performance of the ACRE are presented for standard-ACRE, ACRE with additional filtering, and ACRE with incrementing. The additional filtering results in a reduced chip rate search range but yields improved estimation performance and incrementing has the potential for parallel processing, resulting in dramatically decreased computational time, without loss of performance.

14. SUBJECT TERMS Detection, Estimation, Spread Spectrum, Direct Sequence, Frequency Hopped, Chip-Rate, Frequency Hops			**15. NUMBER OF PAGES** 156
			16. PRICE CODE
17. SECURITY CLASSIFICATION OF REPORT Unclassified	**18. SECURITY CLASSIFICATION OF THIS PAGE** Unclassified	**19. SECURITY CLASSIFICATION OF ABSTRACT** Unclassified	**20. LIMITATION OF ABSTRACT** UL

NSN 7540-01-280-5500 Standard Form 298 (Rev. 2-89)
Prescribed by ANSI Std. 239-18

THIS PAGE INTENTIONALLY LEFT BLANK

Approved for public release; distribution is unlimited

SPREAD SPECTRUM SIGNAL CHARACTERISTIC ESTIMATION USING EXPONENTIAL AVERAGING AND AN AD-HOC CHIP RATE ESTIMATOR

John Baltzer Weber
Lieutenant, United States Navy
A.S. Mathematics, Monterey Peninsula College, 1996
B.S.E.E., University of Arizona, 1999
B.S. Engineering Mathematics, University of Arizona, 1999
M.S.E.E., Naval Postgraduate School, 2003

Submitted in partial fulfillment of the requirements for the degree of

DOCTOR OF PHILOSOPHY IN ELECTRICAL ENGINEERING

from the

NAVAL POSTGRADUATE SCHOOL
March 2007

Author: _____
John Baltzer Weber

Approved by:

_____
Clark Robertson
Professor of Electrical
& Computer Engineering
Dissertation Committee Chair

_____
David C. Jenn
Professor of Electrical
& Computer Engineering

_____
Monique P. Fargues
Associate Professor of Electrical
& Computer Engineering

_____
Frank Kragh
Assistant Professor of Electrical
& Computer Engineering

_____
Carlos F. Borges
Professor of Mathematics

Approved by: _____
Jeffrey B. Knorr, Chairman, Department of Electrical & Computer Engineering

Approved by: _____
Julie Filizetti, Associate Provost for Academic Affairs

THIS PAGE INTENTIONALLY LEFT BLANK

ABSTRACT

This dissertation investigates two methods of spread spectrum (SS) signal characteristic estimation for the two principle types of SS systems, frequency-hopped (FH) and direct sequence SS. The exponential averaging detector is used to detect and estimate the hopped frequencies of a SS-FH signal in the presence of interference signals as well as additive-white-Gaussian-noise (AWGN). The detection method provides an estimate of the AWGN plus inference spectrum using exponential averaging and then generates an estimate of the desired signal spectrum by combining the estimated AWGN plus interference spectrum with the composite (desired signal plus interference plus AWGN) spectrum. Finally, this dissertation evaluates the detector's performance as a function of the exponential coefficient, the combining method, the probability of false alarm, signal-to-AWGN ratio, and signal-to-interference ratio.

The second method of SS signal characteristic estimation uses a digital ad-hoc chip rate estimator (ACRE). The ACRE is used to estimate the chip rate of a half-sine pulse shaped SS direct-sequence signal. The ACRE is explained in relation to its similarities and contrasts to the chip rate detector. The components and performance of the ACRE are presented for standard-ACRE, ACRE with additional filtering, and ACRE with incrementing. The additional filtering results in a reduced chip rate search range but yields improved estimation performance and incrementing has the potential for parallel processing, resulting in dramatically decreased computational time, without loss of performance.

THIS PAGE INTENTIONALLY LEFT BLANK

TABLE OF CONTENTS

LIST OF FIGURES

LIST OF TABLES

THIS PAGE INTENTIONALLY LEFT BLANK

LIST OF ACRONYMS

AR	Autoregressive
ARMA	Autoregressive Moving-Average
AM	Amplitude Modulation
AWGN	Additive White Gaussian Noise
BPF	Band-pass Filter
BPSK	Binary-Phase Shift Keying
CDF	Cumulative Distribution Function
CRD	Chip rate Detector
CW	Continuous Wave
dB	Decibel
DFT	Discrete Fourier Transform
DS	Direct Sequence
FFT	Fast Fourier Transform
FH	Frequency Hopping
HRD	Hop Rate Detector
HPF	High-pass Filter
I	Inphase
IID	Independent Identically Distributed
ISI	Intersymbol Interference
J-B	Jarque-Bera
K-S	Kolmogorov-Smirnov
LRT	Likelihood Ratio Test
LPI	Low Probability of Intercept
LPD	Low Probability of Detection
LPF	Low-pass Filter
MA	Moving-Average
MAP	Maximum *a posteriori*
MFSK	*M*-ary Frequency-Shift Keying
MHAC	Multi-Hop-Observation Auto-Correlation
MISE	Mean Integrated Squared Error
MPSK	*M*-ary Phase-Shift Keying
MSE	Mean Squared Error
MSK	Minimum Shift Keying

N-P	Neyman-Pearson
NIR	Noise to Interference Ratio
pdf	Probability Density Function
PFDM	Prefilter-Delay-and-Multiply
pmf	Probability Mass Function
PN	Pseudo-Noise
PSD	Power Spectral Density
Q	Quadrature
QPSK	Quadrature Phase-Shift Keying
RV	Random Variable
SHAC	Single-Hop-Observation Auto-Correlation
SINR	Signal-to-Interference-Noise Ratio
SIR	Signal to Interference Ratio
SNR	Signal to Noise Ratio
SS	Spread Spectrum

ACKNOWLEDGMENTS

First and foremost, I thank God for giving me the opportunity, talent, and the support of so many people that have made this work possible and for carrying me through the most challenging chapter in my life.

I thank my parents for teaching me the virtues of hard work and tenacity that have been the foundation upon which my education has been built. I also thank the United States Navy for consistently providing me incredible opportunities to serve and better myself in ways that I could have never imagined when I enlisted 18 years ago.

The members of my dissertation committee are gladly acknowledged for their patience, wisdom, and encouraging support. My deepest thanks go to Professor Clark Robertson for his Job-like patience and consistent generous commitment of time, expertise, and energy to help me, even when my productivity was dismal at best. Not only has he been my chief advisor and advocate, but he is a tried and true friend. Professor Frank Kragh has been a tremendous encouragement through his counsel, friendship, and energetic support, and I deeply thank him. Thanks also go to Professor David C. Jenn for his constant willingness to help and his timely support throughout the process. I thank Professor Monique P. Fargues for her dedication and considerable work throughout the process and, specifically, in proof-reading this dissertation so that it is a work worth being proud of. I also thank Professor Carlos F. Borges for his mathematical insights and his down to earth philosophy, which helped me learn valuable life lessons.

Although Dr. Kyle Kowalski was not on my committee, he was of immeasurable help, second only to my committee chair. His insights, work, and funding made this research effort possible and are reflected throughout nearly every aspect of the dissertation, and I deeply thank him. There are many others who have influenced and helped me, throughout my Naval and academic careers, to achieve this goal, and I thank them all collectively and CDR Littleton and Professor Dvorak specifically.

Finally, I want to thank my wife, Kim, and our children, Katie, Amanda, and Johnathon. They have been a tremendous source of joy and fulfillment and have endured the separation and sacrifices required to complete this program. Along with the words of

encouragement that I received from my family and others, God used Isaiah 40:29-31 and Psalms 23 to keep me pressing on, and I give the Holy Trinity the ultimate thanks that I have been successful in this program.

EXECUTIVE SUMMARY

This research investigates detection and estimation methods for the two most common types of spread spectrum (SS) systems, frequency-hopped (FH) SS and direct sequence (DS) SS. For FH-SS, detection and estimation of the hop-frequencies is examined using an exponential averaging detector. For DS-SS, detection and estimation of the chip rate is examined using an ad-hoc chip rate estimator (ACRE).

The background for both detection and estimation methods in the areas of design criteria, signals, analytic tools and a literature review is presented. Then the exponential averaging detector along with the signals and metrics that are used to evaluate its performance are described; specifically, this work investigates the effect of additive-white-Gaussian-noise (AWGN) along with wideband and narrow band interference signals as compared to the FH-SS signal. The detection method provides an estimate of the AWGN plus inference spectrum using exponential averaging and then generates an estimate of the desired signal spectrum by combining the estimated AWGN plus interference spectrum with the composite (desired signal plus interference plus AWGN) spectrum.

Scaled subtraction and quotient-combining methods are described, and the analytic expression for the probability density function (pdf) of the random variable (RV) that models the detector's output with scaled-subtraction-combining and an AWGN plus BPSK input is developed. It was shown that an analytic expression for the pdf of the RV that models the detector's output with either combining method and an AWGN plus BPSK plus CW input is mathematically intractable as far as can be determined. Therefore, a heuristic approach to estimate the pdf of the signal spectral estimate RV when the detector input signal is interference plus AWGN is addressed.

The exponential averaging detector's simulation set-up, decision criteria development, and various simulation results are discussed in detail. The simulation set-up includes the description of the various parameters and signals used. The decision criteria section investigates two methods to heuristically evaluate a pdf model of the detector's output: histograms and goodness-of-fit tests. Upper and mid-estimates for the probability

of false alarm are developed to set the detector's threshold. Simulation results include performance guidelines, heuristic support of the Gaussian postulate, the detector data evaluated by the goodness-of-fit tests, threshold estimates, bounds on P_f, and an evaluation of the detector's performance.

The performance of the detector for various values of signal-to-noise ratio (SNR) and signal-to-interference ratio (SIR) is displayed as plots of simulation-based estimates of the P_d versus SIR for fixed SNR and analyzed. From the simulation estimate of the probability of false alarm, the upper-estimate for the probability of false alarm is selected.

The second method of SS signal characteristic estimation, ACRE, is developed and described next. Although theoretical analysis of the system is investigated, simulation results are primarily used to describe and set parameters. The approach used to develop ACRE is to compare and contrast it to the CRD approach. One contrast between ACRE and the CRD is that the CRD requires an estimate of the chip rate, whereas ACRE only requires a range of values for the chip rate. Thus, as the name implies, the primary purpose of the CRD is to detect the chip rate and not to estimate it. ACRE simultaneously searches a specified bandwidth and estimates the chip rate. This simultaneous search and estimation provides a significant performance advantage over the CRD, which requires that the detector scan through a specified bandwidth in order to detect the chip rate. However, simultaneous search and chip rate estimation results in increased computational complexity.

The performance of the CRD with half-sine pulse shaping is shown using Fourier series coefficients. ACRE is then described in a block diagram and the various blocks discussed, such as how the PSD estimator block closely parallels the CRD spectral component and the motivation and implementation of frequency bin baselining. The complexity of deriving an analytic expression for the pdf of the RV that models the ACRE output is discussed briefly, and from this a heuristic approach is implemented.

Next, the ACRE simulation set-up, decision criteria development and simulation results are discussed. The simulation set-up includes a description of the various parameters and signals used. In the decision criteria section, a threshold is generated using the estimated pdf and a predetermined P_f. The decision criteria as a function of

time bandwidth product (TBW) and the application of the central limit theorem are discussed and three ACRE-based simulation approaches are considered: standard-ACRE, ACRE with additional filtering, and ACRE with incrementing.

The performance of the three ACRE simulations are plotted with SNR versus a simulation based estimate of the probability of detection. Standard ACRE's performance improved 1 dB as the TBW is doubled. Filtering trades off chip rate search range for estimation performance. A quantitative illustration of the trade-off is that the reduction of the search range to a quarter of the original range generated an additional 5 to 6 dB in performance gain. Incrementing shows the potential for parallel processing without loss of performance as well as trading performance for computations. A quantitative illustration of incrementing shows that the relative computational cost, 20 times the standard cost, generated small 1 dB of performance gain. The practical application of the ACRE scheme in this time of ever increasing, inexpensive processing power is greatly expanded since it can be implemented with parallel processing, and additional processing can be exchanged for performance.

THIS PAGE INTENTIONALLY LEFT BLANK

I. INTRODUCTION

A. BACKGROUND

The estimation of signal parameters is a broad and growing field. There are numerous commercial and military applications of signal parameter estimation. Two commercial uses of signal parameter estimation are receiver synchronization and bandwidth management. Two military applications of signal parameter estimation are signal identification and signal deciphering. Military signal identification is used for both communication and radar system identification. Covert communications consist of various low probability of detection (LPD) and low probability of intercept (LPI) transmissions. LPD transmissions can be accomplished with highly directive antennas producing a narrow beam, power control, and/or waveform techniques [1]. Spread spectrum (SS) is an important class of both LPD and LPI waveform techniques and are the only LPD methods discussed in this paper.

Communications system design plays a significant factor in how easy signal parameter estimation is. As an example, if interference with other signals occupying the same bandwidth is not a significant issue, then increasing the transmitted power may be a desirable solution to improving system performance, thus making signal parameter estimation easier. In the case of LPD and LPI signals, significant challenges are encountered in signal parameter estimation. Although SS signals are not necessarily either LPD or LPI, they do pose distinct challenges to detection, interception, and signal parameter estimation.

1. Detectors and Design Criteria Examples

Polydoros and Weber [2] describe an LPI signal as a spread spectrum waveform whose spreading code is unknown to the interceptor. Consequently, the potential interceptor must use wideband detection techniques since a correlation detector cannot be used [3]. The correlation detector is a good example of a detector whose performance is greatly degraded unless a considerable amount of a-priori signal information is known. The correlation detector integrates the product of two waveforms and then makes a decision using a comparator with a decision criteria generated threshold [4]. If the two

waveforms are related, their cross-correlation is non-zero, and in general, the two waveforms only differ in their noise elements and in one of them being passed through a channel transfer function [4]. The advantage of the correlation detector is that the effect of the noise tends toward zero as the integration time increases.

The matched filter provides insight into the correlation demodulator since it produces the same signal at the decision output assuming an additive white Gaussian noise (AWGN) channel [5]. The matched filter maximizes the signal-to-noise ratio (SNR) in AWGN. The matched filter frequency response is the complex conjugate of the transmitted signal's frequency response multiplied by a phase shift [5]. From this it is clear that significant a-priori knowledge is required to implement the matched filter and achieve optimum performance with respect to SNR. Additionally, the correlation detector tends away from the optimum with respect to SNR as the two waveforms multiplied by each other tend away from each other.

Whereas the correlation detector's design is based on the presence of considerable a-priori knowledge, the *radiometer* (or *energy detector*) requires very little. The *radiometer* shown in Figure 1 is the optimum receiver for a signal that is modeled as a stationary Gaussian process in the presence of AWGN [3, 6, 7]. In light of the bandpass filter (BPF) in Figure 1, the bandwidth must also be known in order for the receiver to be optimum. It is also assumed that the signal is either present or absent during the entire integration time interval. From this discussion of the correlation detector and radiometer, it is clear that detectors widely vary with respect to the a-priori knowledge which they require.

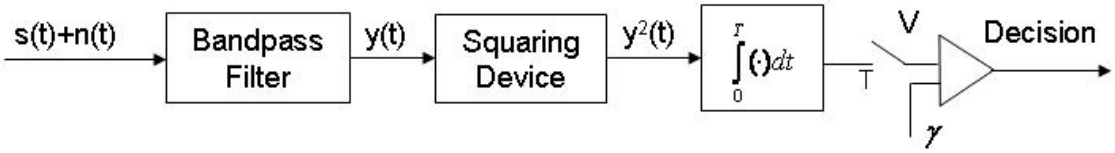

Figure 1 Radiometer.

The motivation behind the radiometer's design is that by squaring the signal a considerable portion of the signal's energy is converted to baseband. The radiometer is said to be optimum in the sense that it implements a likelihood ratio test (LRT) [7]. The LRT is used to set the decision criteria, or threshold. There are a number of LRTs. A few common decision rules are maximum *a posteriori* (MAP), Bayes', and Neyman-Pearson (N-P). The N-P decision rule requires the least amount of information, as is shown in the development of the four decision rules to be discussed.

For signal detection there are two hypotheses: the signal is present H_1 or the signal is not present H_0. Based on one or more observations *Y* of a signal modeled as a random variable *y,* a decision between the two hypotheses is determined. The decision maximizes the probability of a correct decision, and the decision rule can be stated as

$$\text{choose } H_0 \text{ if } P(H_0 \mid y) > P(H_1 \mid y) \text{ and}$$

$$\text{choose } H_1 \text{ if } P(H_1 \mid y) > P(H_0 \mid y),$$

where $P(H_i \mid y)$ is the conditional probability of H_i given *y*. The same decision rule in a more common form is

$$\frac{P(H_1 \mid y)}{P(H_0 \mid y)} \underset{H_0}{\overset{H_1}{\gtrless}} 1, \tag{1.1}$$

which means choose H_1 if the ratio is greater than one and choose H_0 if the ratio is less than one [8].

An alternate form of (1.1) is desirable since the probability density function (pdf) of *y* given H_i is often known vice $P(H_i \mid y)$. From Bayes' rule

$$P(H_i \mid y) = \frac{f_{Y|H_i}(y \mid H_i) P(H_i)}{f_Y(y)}, \tag{1.2}$$

where $f_Y(y)$ is the pdf of the random variable (RV) *y*, $f_{Y|H_i}(y \mid H_i)$ is the conditional pdf of *y* given that the event H_i has occurred, and $P(H_i)$ is the probability of H_i. Rewritten using (1.2), (1.1) is equivalent to

$$\frac{P(H_1) f_{Y|H_1}(y \mid H_1)}{P(H_0) f_{Y|H_0}(y \mid H_0)} \underset{H_0}{\overset{H_1}{\gtrless}} 1. \tag{1.3}$$

The MAP decision rule

$$L(y) = \frac{f_{Y|H_1}(y \mid H_1)}{f_{Y|H_0}(y \mid H_0)} \underset{H_0}{\overset{H_1}{\gtrless}} \frac{P(H_0)}{P(H_1)}, \tag{1.4}$$

is obtained by rearranging (1.3), where $L(y)$ is the *likelihood ratio* [8]. Bayes' decision rule

$$L(y) = \frac{f_{Y|H_1}(y \mid H_1)}{f_{Y|H_0}(y \mid H_0)} \underset{H_0}{\overset{H_1}{\gtrless}} \frac{P(H_0)(C_{10} - C_{00})}{P(H_1)(C_{01} - C_{11})}, \tag{1.5}$$

is similar to MAP except that it includes the decision cost for both decisions when they are correct and incorrect, where C_{ij} is the decision cost with i indicating the decision and j indicating the event [8].

In many applications $P(H_0)$ and $P(H_1)$ are unknown. Another way of managing the possibility of making an incorrect decision is by introducing the probability of false alarm P_f. The N-P criterion sets a bound on P_f and then maximizes the probability of detection P_d within the bounds of P_f [9]. Once P_f is set, a decision threshold γ is generated from $f_{Y|H_0}(y \mid H_0)$ using

$$P_f = \int_{\gamma}^{\infty} f_{Y|H_0}(y \mid H_0) dy, \tag{1.6}$$

where γ is the threshold [5]. The threshold γ is substituted for the right hand side of (1.4) or (1.5) to generate the basic form of the N-P decision rule [8]:

$$L(y) = \frac{f_{Y|H_1}(y \mid H_1)}{f_{Y|H_0}(y \mid H_0)} \underset{H_0}{\overset{H_1}{\gtrless}} \gamma. \tag{1.7}$$

Figure 2 shows a graphical representation of the N-P decision rule.

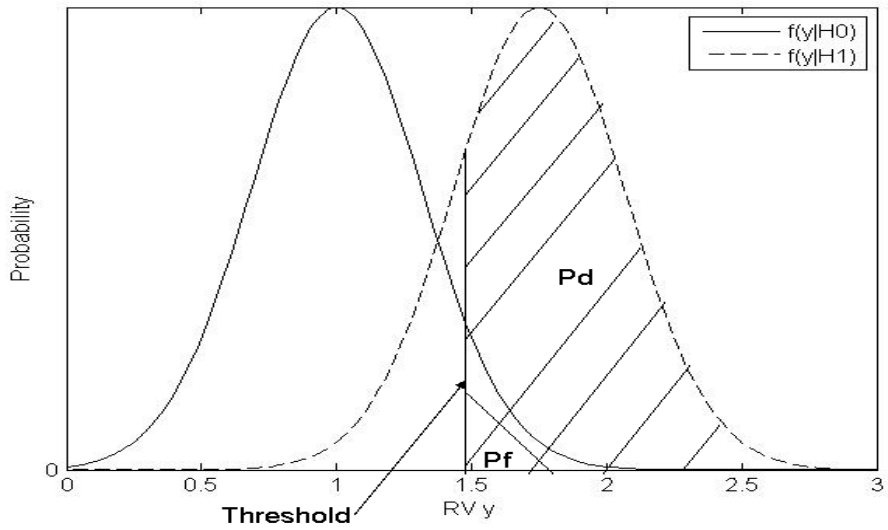

Figure 2 Conditional pdfs with a threshold which sets the detector P_f and P_d.

The process used to solve for the pdf of a RV which is a function of multiple RVs is reviewed to provide background for methods used to obtain pdfs from this work as applied in (1.6) to determine the thresholds. This process is based on a change of variables in two-dimensional integrals [10]. The first step is to choose "companion" functions that facilitate the change of variables in terms of the initial RVs u and q

$$\begin{aligned} z &= \varphi(u,q) \\ w &= \xi(u,q), \end{aligned} \tag{1.8}$$

and then solve for their reciprocal "companion" equations in terms of the substitution RV [10]

$$\begin{aligned} u &= \alpha(z,w) \\ q &= \beta(z,w). \end{aligned} \tag{1.9}$$

Next the Jacobian transformation is solved for by taking the determinant of

$$J = \begin{vmatrix} \dfrac{\partial \alpha}{\partial z} & \dfrac{\partial \alpha}{\partial w} \\ \dfrac{\partial \beta}{\partial z} & \dfrac{\partial \beta}{\partial w} \end{vmatrix}. \tag{1.10}$$

The third step is to map the range of the initial RV onto the range of the substitution RV. Let the substitution range be R. Then the joint density of the substitution RV $p_{z,w}(z,w)$ is determined using the formula

$$p_{z,w}(z,w) = p_{r,s}(\alpha(z,w),\beta(z,w))\left|J\right|,\ (z,w)\in R, \tag{1.11}$$

and zero otherwise. Finally the marginal density $p_z(z)$ is solved by integrating the joint density $p_{z,w}(z,w)$ over the range of w as shown below

$$p_z(z) = \int_{R_w} p_{r,s}(\alpha(z,w),\beta(z,w))\left|J\right|dw, \tag{1.12}$$

where R_w is range of w.

Signal parameter estimation is the focus of some detectors. When the signal in question is a direct sequence spread spectrum signal, a key signal parameter of interest is the chip rate. The chip rate detector (CRD) is a good example of a signal parameter estimation detector. One implementation of the CRD is shown in Figure 3 [11]. From the diagram it is clear that certain knowledge of the signal must be known or estimated prior to the CRD producing the desired results. The signal characteristics that must be known a-priori are the carrier frequency, phase, and the chip rate. The chip rate detector uses the signal phase in the offset frequency generator within the spectral component.

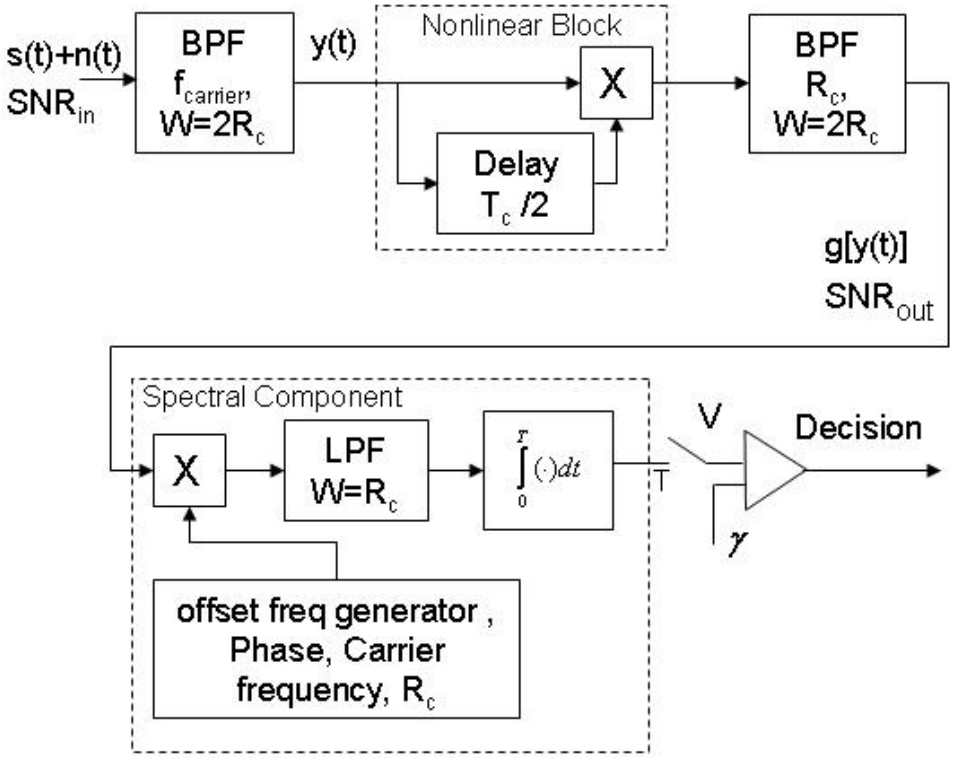

Figure 3 Block diagram of a CRD from [11].

A simple explanation of the CRD scheme follows. It can be shown that the delay-and-multiply block generates a signal which can be represented as the superposition of a non-deterministic and a deterministic signal with a rate-line at the chip rate R_c. The output of the nonlinear block is bandpass filtered to reduce noise. Next, the output of the bandpass filter is downconverted to baseband using the offset frequency generator. The offset frequency generator block requires phase, carrier frequency, and chip rate estimates for $s(t)$. The lowpass filter in the spectral component is optional since the integrator acts as a narrowband filter which is used to increase the SNR. Finally, a decision is made using a comparator. The generation of the deterministic signal is illustrated in Figure 4 [3]. From [3] the product of the non-return-to-zero baseband direct sequence (DS) SS signal and its delay are the sum of a deterministic signal and a random signal given that the delay D satisfies $|D| \le T_c$, where T_c is the chip period. In this

configuration the deterministic signal is a rectangular pulse train with pulse width $T_c - D$ and period T_c. For $|D| > T_c$ the product of the signal and its delayed version does not contain a deterministic component, and the average is zero assuming that the information signal is polar and consists of equally likely ones and zeros.

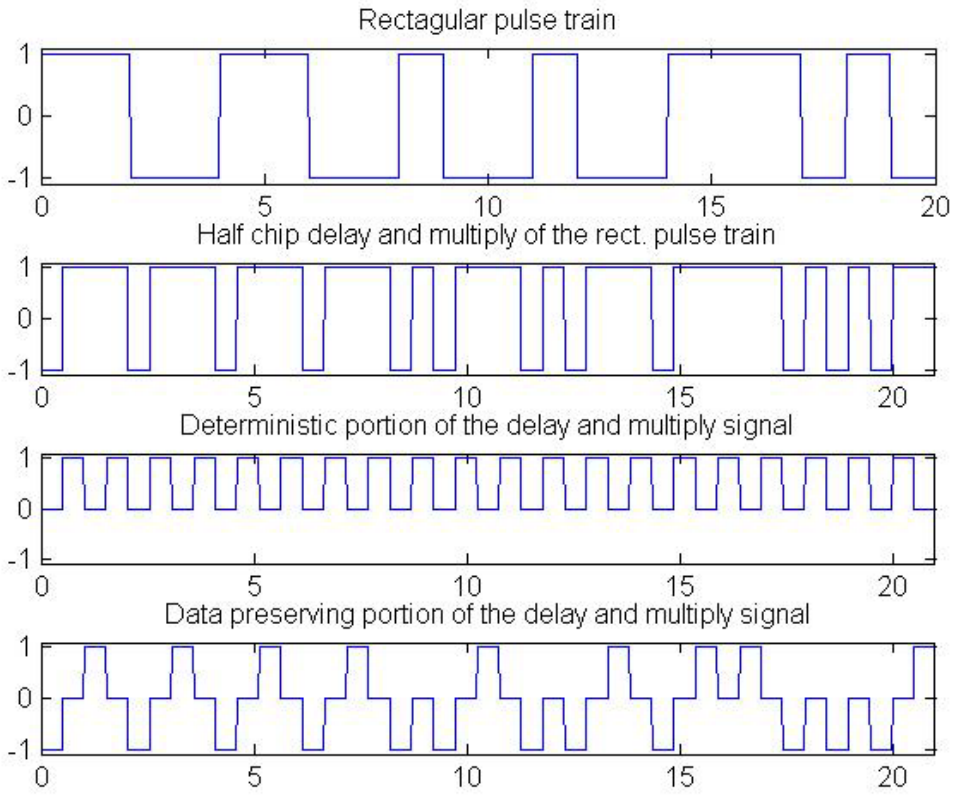

Figure 4 Illustration of how a delay and multiply of a rectangular pulse train with itself can be separated into a deterministic portion and a data preserving portion, assuming the delay is less than the period of the pulse.

The a-priori signal knowledge needed for the CRD's operation can be estimated using the following methods. If the carrier frequency f_c is not known, then it can be estimated using a squaring circuit if the underlying data is binary-phase shift keying (BPSK) modulated. Note that a squaring circuit is effective since a significant amount of

power resides near $2f_c$ for DS-SS signals once the signal is squared [2]. This characteristic also makes squaring the signal an effective way to determine f_c even though very little power is centered near f_c for DS-SS signals [1].

As for the phase, it can be estimated by taking the inverse tangent of the ratio of the downconverted in-phase and quadrature components when it is not known. Alternatively, an estimate of the phase can be obtained using a narrowband filter centered on the chip rate followed by an envelope detector [11].

If the chip rate is unknown a-priori, then the chip rate must be scanned for. The scanning process is based on the CRD acceptable range of performance, given that the delay does not maximize the chip rate-line. The power in the R_c rate-line is computed using the exponential Fourier series coefficient that corresponds to the R_c frequency. The exponential Fourier series coefficients are obtained using

$$c_n = \frac{2}{T_c}\int_0^{T_c} g(t)\exp(-j2\pi f_n t)\,dt, \tag{1.13}$$

where $g(t)$ is a bounded periodic function of period T_c [12]. From (1.13), the Fourier series coefficient that corresponds to the R_c spectral line is

$$c_{R_c} = \frac{2}{T_c}\int_0^{T_c} \text{rect}\left(\frac{t-0.5(T_c-D)}{T_c-D}\right)\exp(-j2\pi R_c t)\,dt, \tag{1.14}$$

where

$$\text{rect}(t/\tau) = u(t+\tau/2) - u(t-\tau/2), \tag{1.15}$$

and *u(t)* is the step function. Equation (1.14) can be evaluated to yield

$$c_{R_c} = \frac{2}{T_c}\int_D^{T_c} \exp(-j2\pi R_c t)\,dt = \frac{1-\exp(-j2\pi R_c D)}{-j\pi}, \tag{1.16}$$

which can be expressed

$$c_{R_c} = \frac{-2}{\pi}\exp(-j\pi R_c D)\sin(\pi R_c D). \tag{1.17}$$

From (1.17), we get

$$\left|c_{R_c}\right|^2 = \frac{4}{\pi^2}\sin^2\left(\pi R_c D\right). \tag{1.18}$$

The maximum R_c rate-line corresponds to half the chip rate, as seen in Figure 5. A common scan range for the CRD's delay is $T_c/2 \le D \le 3T_c/4$. This delay scan range ensures that the power in the R_c rate-line does not go more than 3 dB below the maximum, as seen in Figure 5.

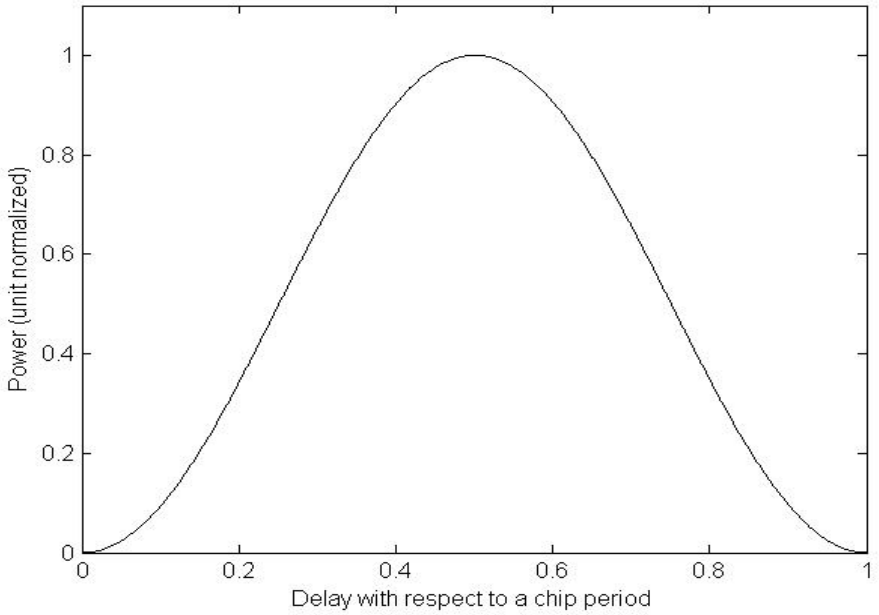

Figure 5 Normalized power in the CRD R_c rate-line as a function of delay with respect to the chip period for a rectangular pulse.

The hop rate of frequency-hopped signals is another signal parameter of interest for detection and estimation. The detectors vary from the optimum performance of the maximum-likelihood based detector with nearly complete a-priori signal knowledge to a sub-optimum multi-hop radiometer with little a-priori signal knowledge [13, 14]. Although the details of these detectors are not described here, it is sufficient to note that each detector's design is based on differing trade-offs of performance for a-priori knowledge.

Some guidelines for performance versus a-priori knowledge trade offs exist. The loss of chip synchronicity in an optimum coherent detector cost between 0.6 dB and 1.4 dB [2]. Another way to consider this statement is that an asynchronous detector loses 0.6 dB to 1.4 dB of performance as compared to its synchronous counterpart. Detectors that combine two independent observations gain 1.5 dB to 3 dB of performance for non-coherent and coherent detectors, respectively [3]. The performance of signal detectors varies and they are often displayed in plots of SNR versus probability of detection P_d for a given probability of false alarm P_f.

A common component in many communications systems is a Hilbert transform circuit. The Hilbert transform can be used to demodulate amplitude modulation (AM) signals, and in some modems it is used to detect baud rate. The Hilbert transform of a real-valued signal $s(t)$ is

$$\hat{s}(t) = s(t) * \frac{1}{\pi t}, \tag{1.19}$$

where * is the convolution operator and is defined as [5]

$$y(t) \equiv x(\tau) * h(t-\tau) = \int_{-\infty}^{\infty} x(\tau) h(t-\tau)\, d\tau. \tag{1.20}$$

The frequency response representation of the Hilbert transform is [5]

$$H(f) = -j\,\mathrm{sgn}(f), \tag{1.21}$$

where $\mathrm{sgn}(\cdot)$ is the *signum* function, defined as

$$\mathrm{sgn}(f) \equiv \begin{cases} 1, & f > 0 \\ 0, & f = 0. \\ -1, & f < 0 \end{cases} \tag{1.22}$$

From (1.21) it is clear that if a signal and the product of its Hilbert transform and j are summed in the frequency-domain, then the composite signal's frequency response for negative frequencies is zero. The addition of signals and scalar multiplication in either the time or frequency-domain is equivalent since the inverse Fourier transform is a linear operation. Thus, the summation of the signal and the product of its Hilbert transform and

j is equivalently implemented in the time-domain as shown in Figure 6. An illustrative example of a potential frequency response associated with passband signals in Figure 6 is shown in Figure 7.

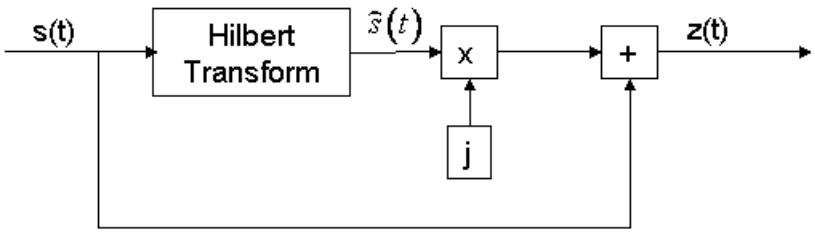

Figure 6 Analytic signal generator for real-valued input *s(t)*.

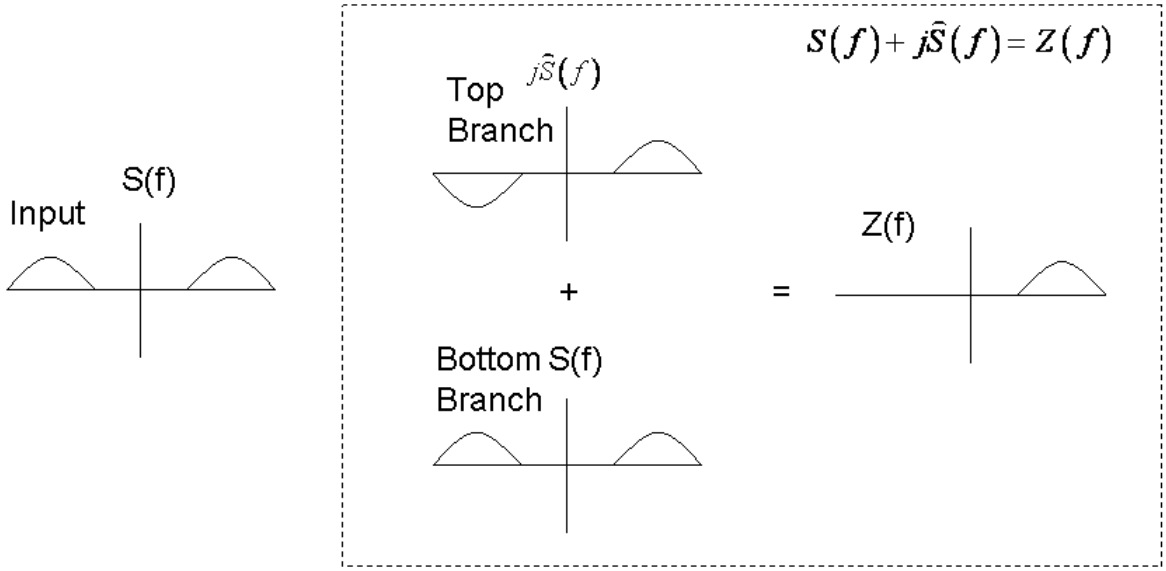

Figure 7 Illustration of signals in the circuit of Figure 6.

The output signal *z(t)* shown in Figure 6 is an analytic signal since its spectrum is zero for all negative frequencies [5]. An analytic signal is also called the pre-envelope of the signal. Since real signals have an even symmetry magnitude frequency response, the frequency response of *z(t)* shown in Figure 7 illustrates that *z(t)* is a complex signal. The complex signal *z(t)* in polar coordinates can be expressed by

$$z(t) = A(t)\exp\left[\, j\phi(t)\right], \tag{1.23}$$

where $A(t)$ is the signal's amplitude, or envelope, and $\phi(t)$ is the signal's phase. The amplitude of a complex signal is the square root of the product of the signal and its complex conjugate. Thus, the product of $z(t)$ and its complex conjugate produces the squared envelope of $z(t)$.

The AM application illustrates how the Hilbert transform can be used to convert a bandpass signal to a baseband signal. An AM signal can be represented by

$$x(t) = A(t)\cos(2\pi f_c t), \tag{1.24}$$

where *A(t)* is the baseband information signal, and f_c is carrier frequency which is much greater than the frequency content in *A(t)*.

2. Signals

This section provides a brief description of the signal and noise types used in following sections. A detailed survey of the topics briefly discussed in this section can be found in [3, 5, 15]. *M*-ary phase-shift keying (*M*PSK) is widely used and its time-domain representation is given by

$$s_{MPSK}(t) = \sqrt{2}A_c \cos\left[2\pi f_{cr} t + 2\pi i/M\right], i = 0,1,..,M-1, \tag{1.25}$$

where A_c^2 is the average received signal power, f_{cr} is the carrier frequency, and *M* is the number of discrete phases used to represent symbols [5]. A constellation representing the eight discrete phases in 8PSK is shown in Figure 8. As the name and (1.25) indicate, the signal information is in the phase.

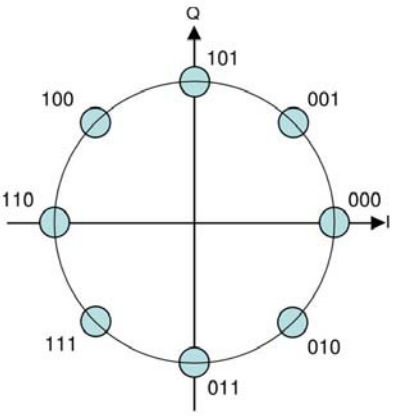

Figure 8 A constellation representation of 8PSK.

When $M = 2$ the *M*PSK signal is binary and is called BPSK. A BPSK signal can be written as

$$s_{BPSK}(t) = \sqrt{2}A_c d(t)\cos(2\pi f_{cr} t), \tag{1.26}$$

where *d(t)* is the information signal consisting of a polar pulse train of positive ones and negative ones. The RV that is used to model the information signal is not described by a pdf but rather a probability mass function (pmf) since the information signal takes on a finite number of values, specifically positive one and negative one. The pmf of the information signal is shown in Figure 9 [16].

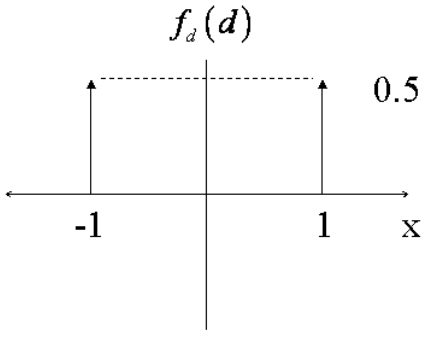

Figure 9 The pmf of the information signal in a BPSK signal.

M-ary frequency-shift keying (*M*FSK) is another widely used modulation scheme, and its time-domain representation is given by:

$$s_{MFSK}(t) = \sqrt{2}A_c \cos\left[2\pi\left(f_{cr} + i/T\right)t\right],\ i = 0,1,..,M-1, \tag{1.27}$$

where T is the symbol period. The $1/T$ frequency increments are the minimum spacing at which dissimilar symbols will be uncorrelated over a symbol time for non-coherent detection. The signal representing the different symbols are orthogonal when the frequency increment is an integer multiple of $1/T$, as shown in (1.27) [15].

Another common modulation scheme is minimum-shift keying (MSK). The MSK scheme can be viewed a special case of either offset quadrature PSK (OQPSK) or a special case of continuous phase modulation (CPM) [15]. A time-domain representation of MSK is given by:

$$\begin{aligned} s_{MSK}(t) = \sqrt{2}A_c\big[&d_I(t)\cos\left(\pi t/2T\right)\cos\left(2\pi f_{cr}t\right) + \\ &d_Q(t)\sin\left(\pi t/2T\right)\sin\left(2\pi f_{cr}t\right)\big], \end{aligned} \tag{1.28}$$

where $d_I(t)$ is the set of even bits and $d_Q(t)$ is the set of odd bits [15]. The sinusoidal terms, $\cos\left(\pi t/2T\right)$ and $\sin\left(\pi t/2T\right)$ with the argument $\pi t/2T$ can be viewed as representing some type of pulse shaping.

Pulse shaping is commonly used for bandwidth control and can also be used to reduce the likelihood of detection [3]. For example, in [17] it is shown that pulse shaping can be used in some network environments to reduce transmit power. In [18] an IEEE 802.15.4 compliant radio transceiver uses half-sine and raised cosine pulse shaping. Nyquist shaped pulses are specifically designed to provide bandwidth control and reduce intersymbol interference (ISI) [5]. Some common shaped pulses used are half sine, raised cosine, and Gaussian. A half sine pulse is a sine wave for half a period, such as that mentioned in the MSK signal defined above. The raised cosine pulse is given by

$$p_{rc}(t) = \frac{\sin\left(\pi t/T\right)}{\pi t/T}\frac{\cos\left(\pi\beta t/T\right)}{1-4\beta^2t^2/T^2}, \tag{1.29}$$

where β is the roll-off factor and has a range from zero to one [3]. When $\beta = 0$ the spectrum of the raised cosine is a rectangle pulse between frequencies $\pm 1/(2T)$. Note

that generating (1.29) when $\beta = 0$ requires that the raised cosine pulse has an infinite duration, which is not practical. Truncating the two extreme ends of the raised cosine pulse, results in a realizable pulse approximating the raised cosine. Similarly, the Gaussian pulse must also be truncated and is generated by

$$p_G(t) = \sqrt{a\pi}W \exp\left(-a\pi^2 t^2 W^2\right), \tag{1.30}$$

where W is the bandwidth of the pulse spectrum and $a = \sqrt{0.5\ln 2}$ in [19].

As mentioned earlier, SS techniques also reduce the likelihood of detection. As the name indicates, the signal spectrum is spread making the signal bandwidth much greater than the bandwidth that is required without using spread spectrum [9]. In addition to reducing the likelihood of detection, SS techniques also improve performance in narrow and broadband jamming environments. This reduced susceptibility to jamming allows multiple access of numerous signals on the same bandwidth. However, SS techniques do not improve performance in the presence of AWGN only.

One SS technique previously mentioned is DS-SS. One form of DS-SS is the product of a BPSK modulated signal and a chipping signal, where the two signals are synchronized so that the start of a symbol interval corresponds to the start of a chip interval, and the chip period is an integer multiple of the symbol period. For a DS-SS signals using BPSK, the time-domain signal can be expressed as

$$s_{DS}(t) = c(t)s_{BPSK}(t), \tag{1.31}$$

where $c(t)$ is the chipping signal and $s_{BPSK}(t)$ is (1.25), when $M = 2$. The chipping signal is commonly obtained from a pseudo-noise (PN) sequence, which is easy to generate using a shift register and exclusive-OR gates and models a true random binary sequence fairly well [5]. Another SS technique is frequency-hopping (FH), where the carrier frequency is periodically switched (hopped) following a predetermined pattern. A PN sequence is a common way of generating the predetermined pattern. *M*FSK is a common modulation scheme used with FH-SS techniques.

The most common type of noise considered is AWGN. In general, AWGN is of the form

$$n(t) = \xi(t) + j\psi(t), \tag{1.32}$$

where $\xi(t)$ and $\psi(t)$ are modeled as independent, real-valued, Gaussian distributed processes with zero mean and identical constant power spectral densities. The metric used to describe the amount of AWGN in a signal summed with AWGN is the SNR, defined as

$$SNR \equiv \lim_{T\to\infty}\left[\frac{\int_{-T}^{T} s^2(t)dt}{\int_{-T}^{T} n^2(t)dt}\right], \tag{1.33}$$

when the AWGN is real [20]. In the digital domain, when there are finite samples, the SNR is defined as

$$SNR_{measured} = \frac{\sum_{l=1}^{N} s^2(l)}{\sum_{l=1}^{N} n^2(l)}, \tag{1.34}$$

where N is the number of samples. However, any of the previously described signals can be considered noise since noise refers to any unwanted signal [15].

When unwanted modulated signals are summed with the desired signal, the metric used is the signal-to-interference ratio (SIR). The SIR is computed in the same way as the SNR except that the interference signal replaces the noise in (1.33) and (1.34). When unwanted, modulated signals and noise are summed with the desired signal another metric used is the signal-to-interference-noise ratio (SINR). The SINR is computed in the same way as the SNR except that the interference plus the noise replaces the noise in (1.33) and (1.34). Although the SINR provides a single metric by which to gauge performance, using both SNR and SIR provides more information and a clearer representation of the results. For this reason SINR is not used in this dissertation. The use of the noise-to-interference-ratio (NIR) with SINR provides the same amount of information as SNR with SIR.

B. LITERATURE REVIEW

There is a considerable amount of published research in the area of detection and estimation of signals and signal parameters. The detection environment that is to be considered determines what methods are used in designing the detector. The detection environment is determined by what signal(s) are to be detected, the type of noise to be suppressed, the channel type to be compensated for, and the detector's knowledge of the signal(s), noise, and channel. The detector's knowledge may be very specific knowledge such as the signal's center frequency or may be less specific such as the range of frequencies where the signal's center frequency might be found.

Another design factor is determining whether the detector will process the data in the time or frequency-domain. The time-domain is further differentiated into continuous time and sampled, or discreet, time. In this dissertation the time-domain will specifically refer to the continuous time-domain unless otherwise specified. The correlation detector is an example of a time-domain detector. According to the Wiener Kinchine theorem, the time and frequency-domain representations are equivalent in principle, but due to practical implementation issues, they are not in practice [21].

The general design approach also must be selected. An example of this idea comes from [22] where two design approaches are discussed. The first approach discussed chooses the detector structure and then optimizes its parameters as in the CRD where a half chip delay is optimum for rectangular, baseband pulses. The second approach determines the order of the detector (i.e., using a quadratic non-linearity) and then solves for the kernel that maximizes the spectral line SNR for a given signal. The selection of the non-linearity transformation applied should be the lowest order non-linearity that emphasizes the spectral line, as increasing the non-linearity order results in decreasing output SNR levels when the SNR (dB) is negative. The optimum design with respect to maximizing the SNR, for a BPSK signal using the second design approach produces the detector shown in Figure 10. Although this approach is desirable since it maximizes the spectral line SNR, the a-priori knowledge required to implement the matched filter may in some cases requires a sub-optimum detector be used instead.

Figure 10 Optimum PSK detector from [22].

These choices, along with others that are not mentioned, predicate that there are numerous detection and estimation approaches. This section is intended as a brief sampling of those areas in detection and estimation that are applicable to the research presented in this dissertation.

An excellent sample article is [11], which focuses on the laboratory performance of SS detectors. This article outlines a general form of some common SS detectors, and gives the specific characteristics for a radiometer, squaring carrier detector, and CRD. The performance of these detectors was compared to the theoretical performance postulated in [23] and [24] as well as a number of other papers.

An example illustrating how specific knowledge of the noise only and noise plus signal statistics are used in detectors is discussed in [23]. The detection of signals with increased complexity such as pulse shaping is discussed in [24]. One of the interesting findings that [24] presents is that the rate-line SNR produced in a CRD with a Nyquist pulse from (1.29) where $\beta = 4$ is 20 dB down from a rectangular pulse signal, and [24] also illustrates the significant impact that pulse shaping has on some detection methods.

A discussion of the delay-and-multiply method structure and optimization via the pre-filter with respect to a defined figure of merit is presented in [25]. The figure of merit is defined as the ratio of the power at the output of the prefilter-delay-and-multiply (PFDM) given signal input and the power spectral density (PSD) of the output of the PFDM given signal plus noise input. The low SNR case is considered so that the denominator of the figure of merit is approximated by the PSD of the output of the PFDM given noise only. Two other items worth mentioning are that the expression used for the figure of merit is an upper bound derived from the Cauchy-Schwartz inequality, and the optimum prefilter is constrained to be a linear filter.

Increasing the order of the non-linearity transformation beyond two is another approach used in detection. This higher order non-linearity approach is used in carrier detection in [26], [27] and [28]. These articles focus on detecting the carrier frequency of PSK signals with binary, quadrature (balanced), and quadrature (unbalanced) configurations. Note that 'unbalanced' means that the I and Q channels have unequal power. These results are important since detectors such as the CRD require the carrier frequency as an input.

The references discussed so far are applicable to DS-SS signals and not FH-SS signals. In [21] a number of detection methods are discussed and compared for unknown sinusoids in noise, which is applicable to FH-SS signals. The types of detection approaches that are compared are a radiometer, fast Fourier transform (FFT) based detection, and correlation based detection with a number of different autoregression models. The results illustrate the trade-offs between performance and complexity.

FH signal detection using autocorrelation techniques as in [21] continue to be discussed and developed as in [29]. The autocorrelation detection technique follows the block diagram shown in Figure 11. Each lag element output from the real-time autocorrelation block is the integration of the product of the input signal with a delayed version of the signal. This step of the processes is very similar to the method used in the CRD. The integration time in [29] is a single hop time interval, thus it is called a single-hop-observation auto-correlation (SHAC) technique. The power sampling is the square of the signal sampled. The final step of weighted accumulation normalizes and sums each sample which is related to a specific lag by a function of the lag and the input signal duration. The last step also uses a receiver-selected parameter which accounts for the term weighted in the last block of Figure 11.

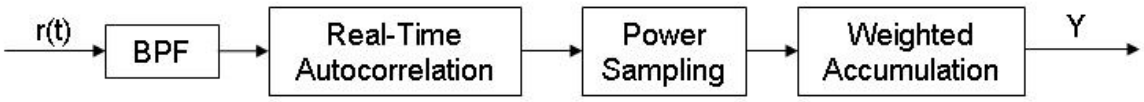

Figure 11 Autocorrelation processing from [29] and [30].

In addition to SHAC there is also the multi-hop-observation auto-correlation (MHAC) technique, where the autocorrelation integration time is defined over multiple hop time intervals [30]. By power sampling in the MHAC domain, the hop-rate information is preserved while frequency and phase dependencies are suppressed. This idea to the use of the MHAC technique to estimate the hop-rate as in [30], [31], and [32]. The hop-rate estimate discussed in [30], [31], and [32] is a maximum-likelihood estimation. A method describing how to use the results from SHAC and MHAC to estimate hop timing is presented in [31]. A recursive variety of MHAC is discussed in [32].

Frequency-domain correlation detection techniques are also used, and the development of these correlation detection techniques are discussed in [33], [34], [35], and [36]. The development and advantages of a spectral correlation function are discussed in [33] and [34] for both analog and digital modulations, respectively. These results show that the spectral-correlation density function is a generalization of the PSD and contains additional information.

A block diagram of the spectral-correlation analyzer is shown in Figure 12 [35], where the rightmost block on the lower branch represents the complex conjugate operation. Specific α values are selected based on the potential frequency range of the cyclostationary properties imbedded in the signal of interest. Note that the spectral-correlation density function $S_x^{\alpha}(f)$ is approximate since the input $x(t)$ is finite in duration. A number of spectral-correlation density function plots are presented in [33] and [34] for phase-modulated signals, frequency-modulated signals, amplitude-shift keying (ASK), QPSK, MSK, and other signal types.

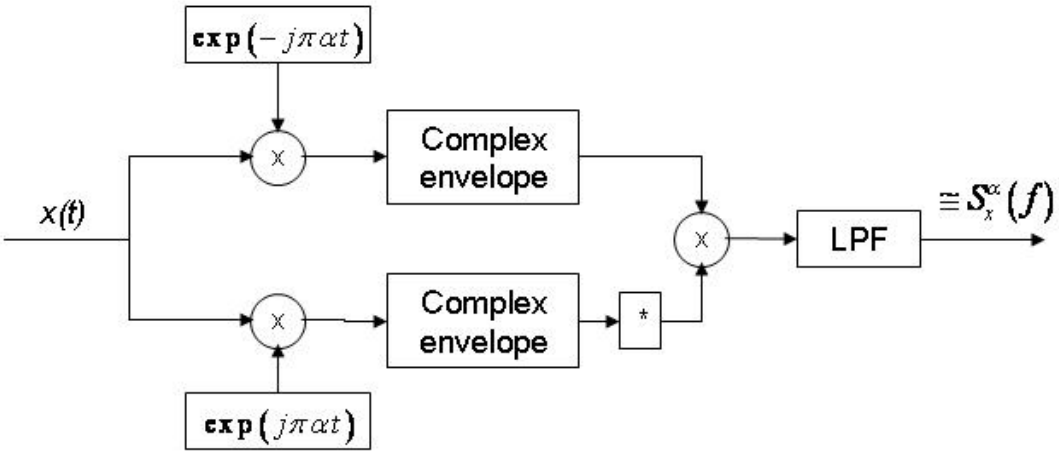

Figure 12 Spectral-correlation analyzer block diagram from [35].

The spectral-correlation density function and its applicability to estimation and detection are discussed in [35], where the bi-frequency plane is developed as an analysis tool. The bi-frequency plane plots frequency verses α. The type of pre-filtering used on the signal determines the support region within the bi-frequency plane. The pre-filters discussed in [35] are low-pass filters (LPF), BPF, and high-pass filters (HPF). Frequency shift filtering is also discussed in [35].

The significant computational costs associated with frequency-domain correlation detection techniques prompted research in the development of computationally efficient algorithms to perform cyclic spectral analysis [36]. The fast Fourier transform (FFT) accumulation method and the strip spectral correlation algorithm subdivide the support region in the bi-frequency plane to increase computational efficiency [36]. For the LPF pre-filter case, the FFT accumulation method subdivides the region into a number of diamond shapes, while the strip spectral correlation algorithm subdivides the region into strips. Each strip covers a number of the FFT accumulation method's sub-regions. Both methods cover the entire support region. Results in [36] illustrate how computational costs may be reduced, by subdividing the frequency range of interest.

Other approaches focus on detecting signals by using autoregressive (AR), moving-average (MA), and autoregressive moving-average (ARMA) techniques, as illustrated in [37]. This specific ARMA-based approach focuses on estimating the signal PSD in the presence of white Gaussian noise and smoothes out chip rate-lines to estimate the PSD. By smoothing the chip rate-lines, the rate-lines become indiscernible from any other aspect of the PSD.

Avoiding detection and estimation is another area of research. An interesting approach to avoid chip rate detection of DS-SS signals is by changing the chip rate as in [38]. This article illustrates how increased transmitter/receiver complexity may be used to increase the difficulty in signal detection. In [38] the chip rate hopping is purported to make the signal undetectable with input SNR less than -11 dB, given an optimum detection bandwidth is available for processing.

A more common form of reducing a signal's detectability is to use pulse shaping. An article which addresses this research area is [39]. This paper proposes that ideally any detector can be defeated if the detector knowledge is applied to the signal. To avoid detection the signal must be sufficiently band-limited and the appropriate amplitude weightings implemented. The types of symbol amplitude distributions considered in the paper are binary, Gaussian, and quantized Gaussian.

Finally, it is worth mentioning the names of a few authors whose work stands out in this area of research: Douglas A. Hill [11, 26, 27, 28], Andreas Polydoros [2, 21, 29] and William A. Gardner [22, 33, 34, 35].

THIS PAGE INTENTIONALLY LEFT BLANK

II. FREQUENCY-HOP ESTIMATION USING EXPONENTIAL AVERAGING

SS signals are used to maintain performance in a jamming environment [5]. A jamming environment is defined as that found when interference signals or jamming signals are present. The presence of interference signals in addition to AWGN increases the difficulty of detecting a FH signal. FH detection methods are dependant on the amount of a-priori knowledge of the channel, the interference signals, and the FH signal. In the case of perfect knowledge of the previous three factors, an optimum detector can be constructed. However, alternate approaches are required since this is rarely the case.

This chapter expanded on the work in [40] by including AWGN in addition to the interference signals. Specifically, this chapter investigates the estimation of frequency hops from a SS-FH signal in the presence of a wideband interference signal, narrowband interference signals, and AWGN. Results derived in this section assume that the noise is AWGN, the interfering signals are high power wideband (relative to a frequency hop bin bandwidth) signals and narrow band continuous wave CW tones, the FH signal is bounded within a given bandwidth, and the FH sequence is fixed for an entire search cycle.

The exponential averaging FH detector is shown in Figure 13. The input into the detector is the sum of the FH signal, interference signal, and AWGN. Before the detector's output can be used, all of the buffers shown by the set of delay blocks must be filled. The operator after the FFT is the absolute value squared. The connections after the absolute value squared block that go down are used to estimate the noise plus interference spectral estimate $M(k)$ using the weight factor ρ and the detector output $\tilde{S}(k)$ which is the FH signal spectral estimate. The two combining methods considered in this work are scaled subtraction and quotient-combining.

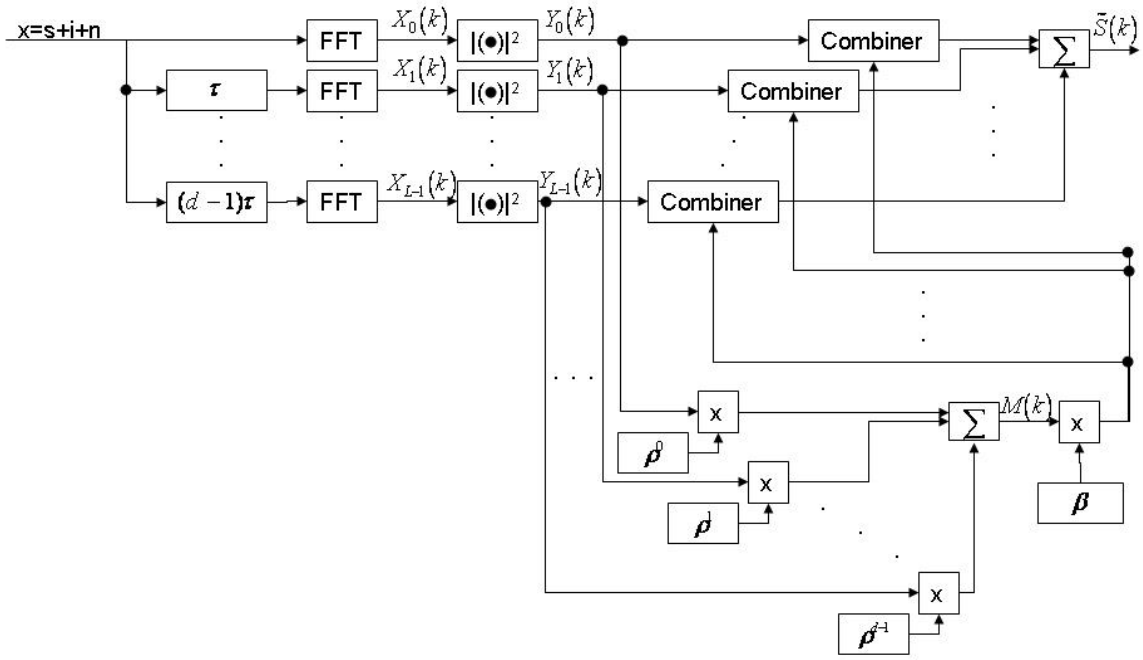

Figure 13 Exponential Averaging Frequency Hop Detector diagram.

A. EXPONENTIAL AVERAGING FH DETECTOR

Exponential averaging is used to generate a spectral estimate of the AWGN plus the interference. The digitized signal is separated into small data segments, which are transformed into the frequency-domain using the discrete Fourier transform (DFT). The DFT of a data block $\left[x(n)\right]|_{n=0}^{N-1}$ is given by:

$$X(k)=\sum_{n=0}^{N-1}x(n)\exp\left[-j\left(2\pi/N\right)nk\right],\quad k=0,1,...,N-1, \tag{2.1}$$

where N is the number of samples [41]. In (2.1) $X(k)$ is in general complex. Although the magnitude squared operation is used in the Hop detector diagram shown in Figure 13, an equally valid choice is the magnitude since the detectability of the FHs is determined by their value relative to the AWGN noise plus interference levels. The scaled spectral estimate of the AWGN plus interference is expressed analytically as

$$M(k)=\sum_{l=0}^{L-1}\rho^{l}Y_{l}(k), \tag{2.2}$$

where $M(k)$ is the noise plus interference spectral estimate, ρ is a weight factor which has values ranging from zero to one, L is the number of segments that the data is separated into, and $Y_l(k)$ is the magnitude squared of the DFT of the l^{th} segment. The primary method used for selecting the parameters ρ, N, and L was by trial and error, based on simulation results. However, a brief discussion of exponential averaging and the interrelation of N and L provide some intuitive sense from which to subjectively address the selection of N and L.

The spectral average of a series of sample sets from the same random process tends to produce a smooth shape as the number of sample sets increases. This result is fairly intuitive in that the underlying spectrum of the random process tends to become more self evident as more data is averaged. Thus, it is not intended as a noise reduction method in and of itself, since the noise is not reduced but rather smoothed out.

Continuing with the description of the exponential averaging detector, the spectral estimate of the FH signal is obtained by combining the noise plus interference spectral estimate with the composite (desired signal, interference, and noise) spectrum. The two combining methods developed in this research are referred to as "scaled-subtraction-combining" and "quotient-combining," and use element-by-element operations with respect to the frequency bins.

Scaled-subtraction-combining is motivated from the basic idea that the time-domain sum of the signal, AWGN, and interference is the input into the exponential averaging detector, so a natural separating operator to consider is subtraction. Since the Fourier transform is a linear operator which is closed under vector addition, using subtraction in a frequency-domain representation of the signal is consistent.

The FH signal spectral estimation process using scaled-subtraction-combining is expressed analytically as

$$\tilde{S}_s(k) = \sum_{l=0}^{L-1} \left[Y_l(k) - \beta M(k) \right], \tag{2.3}$$

where β is a scaling factor and the operation is implemented element-by-element with respect to *k*. The scaling factor β is used to normalize $M(k)$ with respect to the average values of $Y_l(k)$ and is given by

$$\beta = \left(\sum_{l=0}^{L-1} \rho^l \right)^{-1} = \frac{1-\rho}{1-\rho^L} \approx 1-\rho \tag{2.4}$$

which represents the value which approximately normalizes $M(k)$ and is exact when $Y_l(k)$ is fixed. The term $Y_l(k)$ can be moved out of the summation in (2.2) if $Y_l(k)$ does not vary in time since $Y_l(k) = Y_m(k)$ for all value of *l* and *m*, resulting in $\beta M(k) = Y_l(k)$. The reciprocal of β is the geometric series, so the approximation for β is exact as *L* approaches infinity.

The scaling factor is a natural consequence of exponential averaging since $M(k)$ is compared with $Y_l(k)$ yet $M(k)$ gets larger as $\rho \to 1$ and the number of branches increases. By using the scaling factor, the AWGN plus interference spectral estimate and the input spectrum are similar in magnitude, which provides the greatest emphasis on the signal spectrum when subtraction combining is used.

The FH signal spectral estimation process using quotient-combining is expressed analytically as

$$\tilde{S}_q(k) = \sum_{l=0}^{L-1} Y_l(k) / M(k), \tag{2.5}$$

where the quotient is taken element-by-element with respect to *k*. The scaling factor β can also be included in the quotient-combining scheme as a normalizing factor although it is not needed since only the relative difference in bins is important versus the absolute difference. Thus, by using quotient-combining, the frequency response of the AWGN plus interference is approximately normalized over the entire frequency range of interest. The quotient-combining scheme frequency bin output is unitless. This ratio based normalization allows bins in different frequency regions that have different magnitude local averages to be easily compared with each other.

Note that a time varying signal is disproportionately represented in $M(k)$. The lack or excess representation of a time varying signal in $M(k)$ is related to the weight factor and the branch(s) that include(s) the time varying signal. FH signals are just such signals. From this observation the individual frequency hops of a FH-SS signal are distinguished from the AWGN and interference signals in (2.5) since the spectrum of a FH-SS signal varies in time and the individual hops are usually not proportionally represented in $M(k)$.

The amount that the FH signal is disproportionately represented in $M(k)$ is related to the hop rate and the period over which the average is taken. This characteristic illustrates why an estimated range of the FH signals period must be known a-priori, since a number of the frequency hops will be completely unrepresented in the spectral estimate if the averaging period is significantly less than the FH sequence cycle

The discussion above is most easily seen when linear averaging versus exponential averaging is applied. However, exponential averaging weights more recent elements more heavily. Thus, exponential averaging provides a convenient method to retain the benefits of averaging and potentially suppressing signals with a time varying spectrum. The parameter ρ determines how heavily recent elements are weighted in the exponential average. A few factors that help determine ρ are the data size available for processing, the FH hop cycle duration, and the duration of a full cycle for the interference signal. Thus, by the time a hop is represented in a segment its previous representation is negligible in $M(k)$. Similarly, the factors used to determine ρ are also used to determine what values should be chosen for *N* and *L*.

The values of *N* and *L* are inversely proportional, assuming that the data segments do not overlap nor are they zero padded. This assumption implies that the segment size and *N* are equal. The value of *N* also has an upper bound of the data length and a more practical upper restriction due to errors that result from exceeding machine memory. The value of *N* has a lower bound due to the required frequency resolution. As an example,

for most applications a 64 point DFT to evaluate a 10 MHz bandwidth is insufficient. Finally, the value of *N* should be chosen to be an integer power of two, which allows the DFT to be evaluated using a FFT without requiring zero padding.

In general it is better to choose smaller values of *N* within the range previously discussed. The reason that a smaller segment size is desired is that it reduces the chance that a segment contains multiple hops and, thus, increases the suppression of the FH signal by the exponential averaging. Once the value of *N* is determined, then the value of *L* is the integer number of times that *N* goes into the data length. Data that does not make up a complete sample set can either be disregarded or zero padded and used.

B. SIGNALS AND METRICS

The FH signal used to evaluate the exponential averaging FH detector discussed in this research is a FH-MSK waveform with seven frequency hops. The carrier frequency is 10 MHz. The FFT of the FH signal is shown in Figure 14.

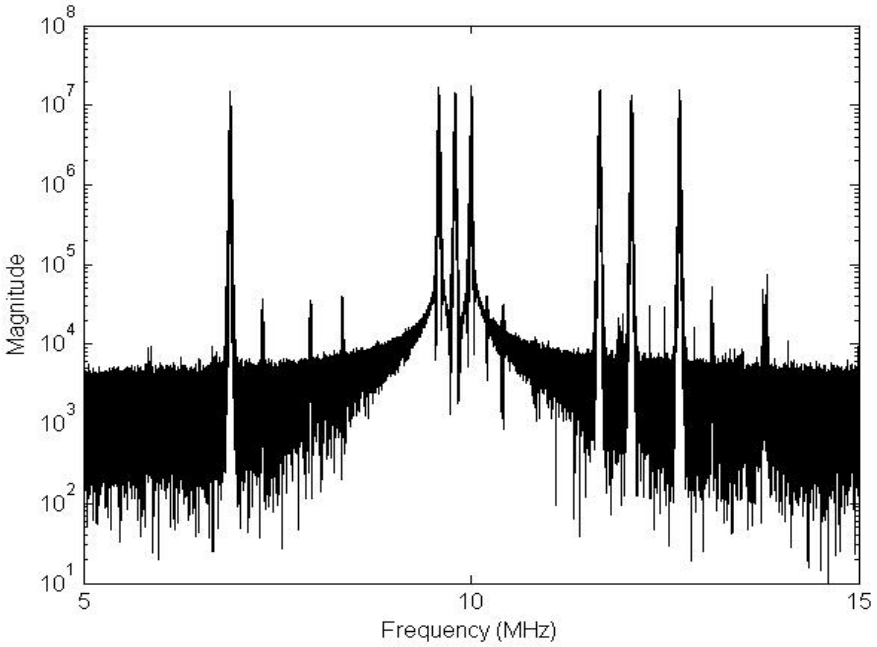

Figure 14 Fourier transform of FH/MSK signal, $f_s = 50$ MHz.

The interference signal is the sum of a BPSK signal with a carrier frequency of 10 MHz and a continuous wave (CW) signal. The FFT of the BPSK interference signal is shown in Figure 15. The FFT of the CW interference signal is show in Figure 16. There are 21 CW signals in the bandwidth of interest. The FFT of the composite interference signal is shown in Figure 17. The FFT of the FH-MSK signal plus the interference signal is shown in Figure 18. The signals are sampled at 50 MHz.

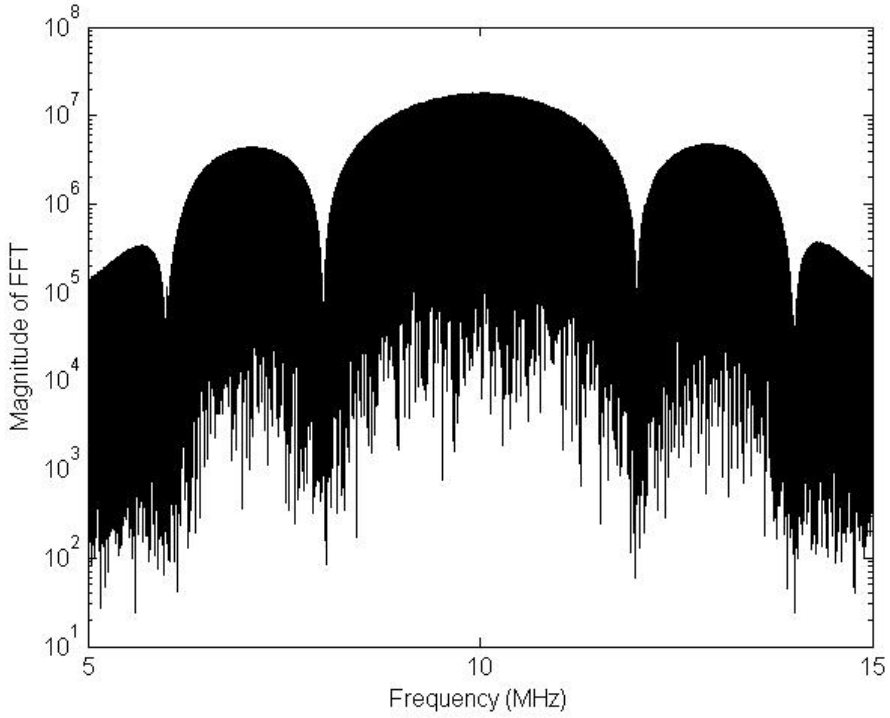

Figure 15 Fourier transform of the BPSK interference signal, $f_s = 50$ MHz.

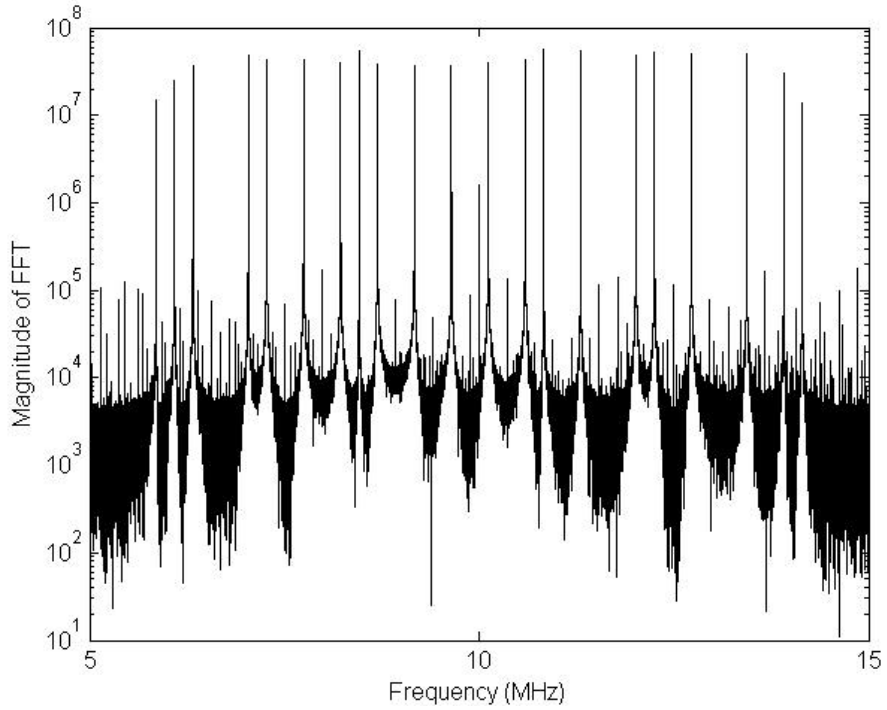

Figure 16 Fourier transform of the CW interference signal, $f_s = 50$ MHz.

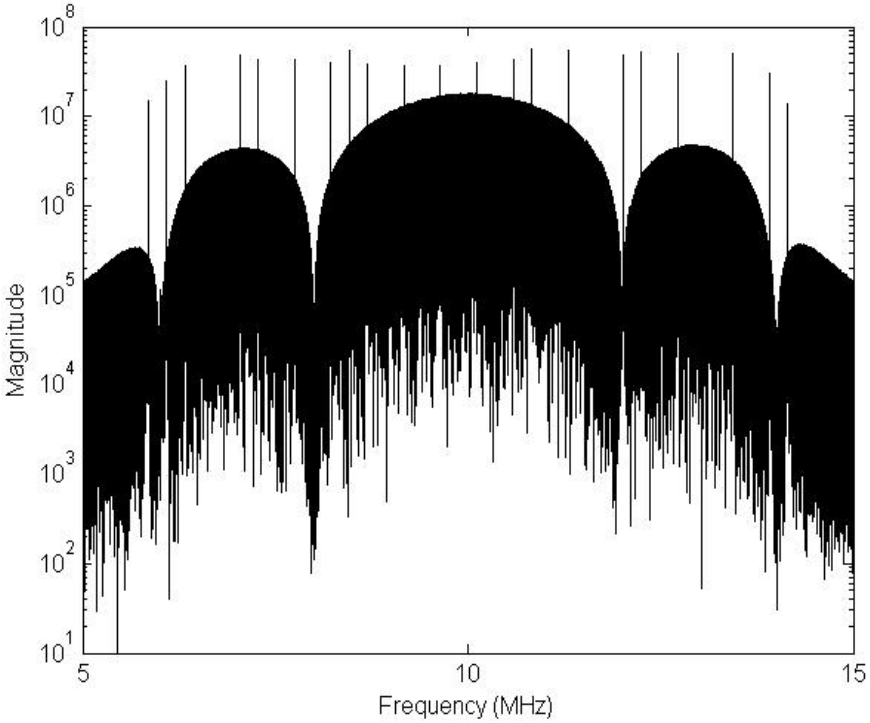

Figure 17 Fourier transform of the composite interference signal (BPSK plus CW), $f_s = 50$ MHz.

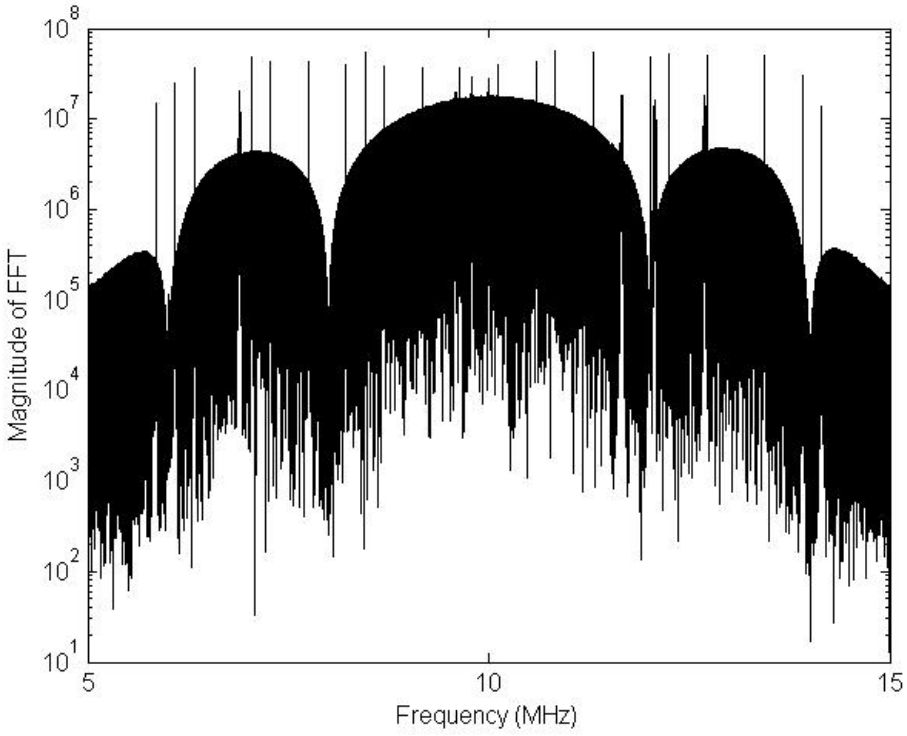

Figure 18 Fourier transform of the sum of the FH-MSK and interference signals, $f_s = 50$ MHz.

The BPSK signal is selected because of its relatively flat spectrum near the center of the main lobe relative to the bandwidth of a FH bin. The CW signal was selected for its narrowband characteristic which is similar to a tone jamming signal. Tone jamming can be the most effective noise jammer to FH systems [3]. Since the two interference signals are dissimilar, the combination of the two signals summed with AWGN is a reasonably hostile environment in which to evaluate the detector. Visually, it is clear that it can be difficult to find the FH-MSK signal, especially for low SIR.

The performance metrics are SIR, SNR, and P_d. The signal power in the SIR and SNR metrics is the power in the FH-MSK signal. The interference power in the SIR metric is the power of the BPSK and CW signals summed in the time-domain. The noise power in the definition of the SNR quantity is the power of the AWGN. SIR and SNR

quantities are varied by scaling normalized time-domain signals. The metric P_d is estimated by simulation, dividing the number of detections by the number of simulations runs for a fixed P_f.

C. ANALYTIC DECISION CRITERIA

It is desirable that the selected performance measures enhance the detector's performance to the greatest extent possible. The detector is not the optimum detector since there is limited a-priori knowledge. However, the decision criteria that the detector uses to evaluate the data can be optimized with respect to the detector. What is meant by optimum decision criteria in this context are that P_f does not exceed a preset value and that P_d is maximized. The threshold is obtained by using (1.6) where $\tilde{S}_s$ in Figure 13 is the RV that models the signal at the input into the comparator when only noise (undesirable signals) are present.

Determining the pdf of $\tilde{S}$ in the interference plus AWGN detector input case $f_{\tilde{S}|x=i+n}(\tilde{S} \mid x = i + n)$, so that it can be used in (1.6) to obtain the threshold is not a simple table look-up nor is it available elsewhere. In Subsection II.C.1 the analytic expression for $f_{\tilde{S}_s|x=i_{BPSK}+n}(\tilde{S}_s \mid x = i_{BPSK} + n)$ is developed, where $f_{\tilde{S}_s|x=i_{BPSK}+n}(\tilde{S}_s \mid x = i_{BPSK} + n)$ is a special case of $f_{\tilde{S}|x=i+n}(\tilde{S} \mid x = i + n)$ with the interference equal to the BPSK interference signal and scaled-subtraction combining is used. The special case pdf is obtained by solving for the pdf of $\tilde{S}$ when the detector's input is only AWGN, $f_{\tilde{S}|x=n}(\tilde{S} \mid x = n)$ and then from this intermediate step, intuition is employed to obtain $f_{\tilde{S}_s|x=i_{BPSK}+n}(\tilde{S}_s \mid x = i_{BPSK} + n)$.

Subsection II.C.2 develops the analytic expression for the general case where the interference includes the CW signals for both combining methods to the point that an unknown joint pdf is necessary to proceed with an analytic solution. Although the work

in Subsections II.C.1 and II.C.2 is not used in this dissertation it is presented for potential use in the future with respect to the special case and as justification to solve for $f_{\tilde{S}|x=i+n}(\tilde{S} \mid x = i + n)$ using heuristic methods considered in Chapter III.

1. Special Case Detector Output pdf Analysis

First, the AWGN only detector input case is considered and next results are expanded to include the BPSK interference signal for the scaled-subtraction combining method. The delays shown in Figure 13 preceding the FFT inputs ensure that the segments of data that are inputs to the FFT do not overlap in time. The RV that models the input into a specific FFT block is independent of the RVs that model all the inputs into the other FFT blocks. To find the pdfs of the RVs that model the output of the FFTs, the FFT input pdf is transformed as the sum of scaled, independent, Gaussian RVs with the result

$$X_l(k) = \sum_{m=1}^{N} x_l[m] \exp\left(-j2\pi km/N\right), \tag{2.6}$$

where $X_l(k)$ is a RV representing the k^{th} frequency bin output of the l^{th} branch in the exponential averaging detector, N is both the number of FFT frequency bins and the number of samples in a segment, and $x[m]$ is the m^{th} input element into the FFT.

Next Euler's formula is applied to the exponential term in (2.6), resulting in

$$X_l(k) = \sum_{m=1}^{N} x_l[m]\left[\cos\left(2\pi km/N\right) - j\sin\left(2\pi km/N\right)\right]. \tag{2.7}$$

It is observed that, for a specific frequency bin, the trigonometric functions reduce to scalars having values between a negative one and a positive one. Recall that when the RV $y = ax + b$, where x is a RV, and a and b are scalars the pdf of y is given by [42]

$$f_y(y) = \frac{1}{|a|} f_x\left(\frac{y-b}{a}\right). \tag{2.8}$$

Equation (2.8) indicates that, in general, the distribution does not change except for a scaling factor when $b = 0$. The summation of the resulting scaled, independent, identically distributed (IID) RVs, in the case of AWGN, generates a RV that is Gaussian

with a mean scaled by $\sum_{m=1}^{N} a_m$ and a variance scaled by $\sum_{m=1}^{N} a_m^2$ [43]. The scaling factor of the mean is zero since it is the non-normalized average of a cosine or sine over an integer multiple of 2π. The variance scaling factor is also a constant and is one-half. Thus, given the detector input is AWGN, the FFT output pdf is a complex Gaussian with zero mean and the input variance scaled by $0.5N$, where *N* is the number of frequency bins in the FFT.

For the case when *x* is the sum of a BPSK signal and AWGN, the analysis is different, as the characteristic function approach is taken to determine the pdf of the sum of the two RVs. The characteristic function of the random variable *y* is defined as [44]

$$\Phi_y(\omega) \equiv E\left\{\exp\left(j\omega y\right)\right\}. \tag{2.9}$$

The relationship between the characteristic function and the pdf are given by [44]:

$$f_y(y) = \frac{1}{2\pi}\int_{-\infty}^{\infty} \Phi_y(j\omega)\exp(-j\omega y)\,d\omega = FT^{-1}\left[\Phi_y(j\omega)\right]|_y \tag{2.10}$$

and

$$\Phi_y(\omega) = \int_{-\infty}^{\infty} f_y(y)\exp\left(j\omega y\right)dy = FT\left[f_y(y)\right]. \tag{2.11}$$

Note, the association of the constant $\frac{1}{2\pi}$ and the sign of the exponential in the Fourier and inverse Fourier transform pair varies [12, 44]: The characteristic function of the Gaussian RV *y* is given by

$$\Phi_y(\omega) = \exp\left(j\mu\omega - \sigma^2\omega^2/2\right), \tag{2.12}$$

where μ is the mean of *y* and σ^2 is the variance of *y* [45]. From (2.9) the pdf of *y* is not required if $y = g(x)$ and the pdf of the RV *x* is known since the expected value of a function of a RV is given by

$$E\{y\} = \int_{-\infty}^{\infty} g(x)\, f_x(x)dx, \tag{2.13}$$

where $f_x(x)$ is the pdf of *x* [46].

The characteristic function of the sum r of two independent RVs u and n is the product of the summed RVs' characteristic functions: i.e., [47]

$$\Phi_r(j\omega) = \Phi_u(j\omega)\Phi_n(j\omega). \tag{2.14}$$

The characteristic function of a zero mean Gaussian RV is [47]

$$\Phi_n(\omega) = \exp\left(-\sigma^2\omega^2/2\right). \tag{2.15}$$

BPSK signal's properties are discussed before the characteristic function is developed. Recall that a BPSK signal can be represented as

$$u = A\cos\left(\omega_c t + \theta\right), \tag{2.16}$$

where ω_c is the carrier angular frequency and θ is a RV that contains the BPSK signal's data. The RV θ has values $\theta = 0, \pi$ and pmf

$$f_\theta(\theta) = \frac{1}{2}\left[\delta\left(\theta\right) + \delta\left(\theta - \pi\right)\right]. \tag{2.17}$$

The characteristic function of u is obtained by first generating a function of the RV θ using the entering argument of the expectation in (2.9) and substituting $u(\theta)$ from (2.16) for y, and is given by

$$g\left(\theta\right) = \exp\left(j\omega u\left(\theta\right)\right). \tag{2.18}$$

The characteristic function of u is obtained by substituting (2.18) into (2.9) to yield

$$\Phi_u(\omega) = E\left\{g\left(\theta\right)\right\}, \tag{2.19}$$

and then applying (2.13) to the right side of (2.19) which gives the characteristic function of u as

$$\Phi_u(\omega) = \int_{-\infty}^{\infty} g\left(\theta\right) f_\theta\left(\theta\right) d\theta. \tag{2.20}$$

Substituting (2.16) into (2.18), and substituting the result and (2.17) into (2.20) yields

$$\Phi_u(\omega) = \int_{-\infty}^{\infty} \frac{1}{2}\left[\delta\left(\theta\right) + \delta\left(\theta - \pi\right)\right]\exp\left[j\omega A\cos\left(\omega_c t + \theta\right)\right] d\theta. \tag{2.21}$$

At that point, the variable t in (2.21) is set to zero without loss of generality since the statistical properties are time invariant. Next, the characteristic function in (2.21) simplifies to

$$\Phi_u(\omega) = \frac{1}{2}\left[\exp(j\omega A) + \exp(-j\omega A)\right]. \tag{2.22}$$

Substituting (2.15) and (2.22) into (2.14), leads to the characteristic function of the sum of the BPSK interference signal and the AWGN expressed as

$$\Phi_r(j\omega) = \cos(\omega A)\exp\left(-\sigma^2\omega^2/2\right). \tag{2.23}$$

Substituting (2.23) into (2.10), leads to

$$f_r(r) = \frac{1}{2\pi}\int_{-\infty}^{\infty}\frac{1}{2}\left[\exp(j\omega A) + \exp(-j\omega A)\right]\exp\left(-\sigma^2\omega^2/2\right)\exp(-j\omega r)\,d\omega. \tag{2.24}$$

The pdf of *r* is further simplified by rearranging (2.24) as

$$f_r(r) = \frac{1}{4\pi}\left\{\int_{-\infty}^{\infty}\left[\exp(j\omega A)\exp\left(-\sigma^2\omega^2/2\right)\right]\exp(-j\omega r)\,d\omega + \int_{-\infty}^{\infty}\left[\exp(-j\omega A)\exp\left(-\sigma^2\omega^2/2\right)\right]\exp(-j\omega r)\,d\omega\right\}. \tag{2.25}$$

Noting that the elements in the square brackets are of the form of the Gaussian characteristic function in (2.12), and are given as $\Phi_{r1}(\omega) = \exp\left(j\omega A - \sigma^2\omega^2/2\right)$ and $\Phi_{r2}(\omega) = \exp\left(-j\omega A - \sigma^2\omega^2/2\right)$, allows (2.24) to be simplified as

$$f_r(r) = \frac{1}{2\pi}\int_{-\infty}^{\infty}\Phi_{r1}(\omega)\exp(-j\omega r)\,d\omega + \frac{1}{2\pi}\int_{-\infty}^{\infty}\Phi_{r2}(\omega)\exp(-j\omega r)\,d\omega. \tag{2.26}$$

Since (2.26) is in the form of (2.10), and Φ_{r1} and Φ_{r2} are Gaussian characteristic functions, $f_r(r)$ may be rewritten as

$$f_r(r) = \frac{1}{2}\left[\frac{1}{\sqrt{2\pi\sigma^2}}\exp\left(-\frac{(r+A)^2}{2\sigma^2}\right) + \frac{1}{\sqrt{2\pi\sigma^2}}\exp\left(-\frac{(r-A)^2}{2\sigma^2}\right)\right], \tag{2.27}$$

which is the sum of two Gaussian distributions scaled by one half with means $\pm A$ and variance σ^2.

When *r* is the input into the delays shown in Figure 13, the output of the delays can be viewed as nearly independent if the segment length is much greater than the BPSK bit rate. Note that there are many bits in each segment of data or in a given branch so that there are few bits common to any two segments compared to the total number of bits

when the segment length is much greater than the BPSK bit rate. From this discussion, the RV at the input of a specific FFT block is considered independent of the RVs at the inputs of all the other FFT blocks. Since the FFT is a linear operator and $f_r(r)$ can be viewed as the sum of two Gaussian distributions, the analysis for the AWGN-only input can be used to determine the pdf of the output of the FFT given *r* is the detector input. Thus, given that *r* is the detector input, the pdf of the FFT output is a complex Gaussian with zero mean with the input variance scaled. The variance scaling factor is twice the variance of one of the Gaussians times $0.5N$ where *N* is the number of frequency bins in the FFT.

The block next to the FFT operation shown in Figure 13 can be chosen as either the absolute value or the absolute value squared. The selection of either operation is arbitrary since the relative difference of the FH signal versus the AWGN plus interference is desired. The absolute value squared is selected in this work, which leads to:

$$Y_l(k) = X^2_{(l,i)}(k) + X^2_{(l,q)}(k), \tag{2.28}$$

where $X_{(l,i)}(k)$ and $X_{(l,q)}(k)$ are the in-phase and quadrature components of the complex Gaussian RV $X_l(k)$, respectively.

Recall that $Y_l(k)$ is a central chi-squared pdf when $Y_l(k)$ is defined as

$$Y_l(k) = \sum_{m=1}^{d} X^2_{(l,m)}(k), \tag{2.29}$$

where $X_{(l,m)}(k), m = 1,2,...,d$ are independent identically distributed (IID) Gaussian RVs with zero mean and variance σ^2 [5]. The generic chi-squared pdf of *Y* is given by: [5]

$$f_Y(Y) = \frac{1}{\sigma^d 2^{d/2}\Gamma(d/2)} Y^{d/2-1} \exp\left(-Y/2\sigma^2\right), Y \geq 0. \tag{2.30}$$

Since (2.30) reduces to the exponential distribution in the case of interest; i.e., when $d = 2$ where *d* corresponds to the inphase and quadrature signal components, the pdf of $Y_l(k)$ is an exponential distribution [42]

$$f_{Y_l}(Y_l) = \lambda_l \exp(-\lambda_l Y_l), Y_l \geq 0, \lambda_l = \frac{1}{2\sigma^2}. \quad (2.31)$$

The diagram in Figure 13 forks into two paths. The lower path, which leads to the noise interference spectral estimate, is considered first. Each $Y_l(k)$ term is scaled by ρ^l where ρ is the weight factor in (2.2). We obtain the value of λ_l in (2.31) as $\frac{1}{2(\rho^l)^2\sigma^2}$ by using the transformation in (2.8) to account for scaling of $Y_l(k)$ by ρ^l. The L branches are then summed to generate the noise interference spectral estimate $M(k)$. The pdf of $M(k)$ is obtained as the convolution of the L pdfs of the RVs $\rho^l Y_l(k)$ where $l = 0,1,...,L-1$.

Since convolution in one domain is equivalent to multiplication in the transform domain, the L^{th} order convolution is found using transforms. The pdfs of $\alpha^l Y_l(k)$ are transformed using the Laplace transform

$$H(s) = \int_0^\infty h(t)\exp(-st)\,dt, \quad (2.32)$$

since the RVs $\rho^l Y_l(k)$ are greater or equal to zero [42]. The Laplace transform of the pdf of $\rho^l Y_l(k)$, from (2.31) and (2.32) is given by

$$F_{Y_l(k)}[Y_l(k)] = \frac{\lambda_l}{s+\lambda_l}, \quad (2.33)$$

where $\lambda_l = \frac{1}{2(\rho^l)^2\sigma^2}$. Taking the inverse Laplace transform of the product of L pdfs of the form in (2.33), leads to the pdf of $M(k)$ as

$$f_{M(k)}[M(k)] = \mathcal{L}^{-1}\left\{\prod_{l=0}^{L-1}\frac{\lambda_l}{s+\lambda_l}\right\}, \quad (2.34)$$

where $\mathcal{L}^{-1}\{\cdot\}$ is the inverse Laplace transform. Equation (2.34) can be simplified to

$$f_{M(k)}[M(k)] = \left(\prod_{l=0}^{L-1}\lambda_l\right)\mathcal{L}^{-1}\left\{\prod_{l=0}^{L-1}\frac{1}{s+\lambda_l}\right\}. \quad (2.35)$$

Next, a partial fraction expansion is used to obtain the inverse Laplace transform. By expanding the product in (2.35) into the sum of easily inverted ratios, the inverse is obtained as

$$\prod_{l=0}^{L-1}\frac{1}{s+\lambda_l}=\sum_{l=0}^{L-1}\frac{A_l}{s+\lambda_l}, \tag{2.36}$$

where A_l are scalars [48]. The value of A_0 is obtained by multiplying both sides of (2.36) by $(s+\lambda_0)$ and setting $s=-\lambda_0$. As a result, every element in the summation except for the 0^{th} element goes to zero. The left hand side of (2.36) is similar except that the $(s+\lambda_0)$ element is factored out. By repeating this process L times, all A_l scalars are obtained, resulting in

$$A_l=\prod_{\substack{i=0\\ i\neq l}}^{L-1}\left(\frac{1}{\lambda_i-\lambda_l}\right). \tag{2.37}$$

Thus, from (2.36) and (2.37), the pdf in (2.35) can be written as

$$f_{M(k)}\left[M(k)\right]=\left(\prod_{l=0}^{L-1}\lambda_l\right)\mathcal{L}^{-1}\left\{\sum_{l=0}^{L-1}\frac{A_l}{s+\lambda_l}\right\}. \tag{2.38}$$

Using (2.31) and (2.33) in (2.38), we get the pdf of $M(k)$

$$f_{M(k)}\left[M(k)\right]=\left(\prod_{l=0}^{L-1}\lambda_l\right)\sum_{l=0}^{L-1}A_l\exp\left(-\lambda_l M(k)\right), M(k)\geq 0. \tag{2.39}$$

The next step is specific to the combining method being considered. First we consider the scaled-subtraction-combining method, and later the quotient-combining method in the next subsection. Substituting (2.2) into (2.3), we get

$$\tilde{S}_s(k)=\sum_{l=0}^{L-1}\left[Y_l(k)-\beta\sum_{i=0}^{L-1}\rho^{L-i}Y_i(k)\right], \tag{2.40}$$

which can be algebraically manipulated to get

$$\tilde{S}_s(k)=\sum_{l=0}^{L-1}\left(1-L\beta\rho^{L-l}\right)Y_l(k). \tag{2.41}$$

The pdf which models the RV $\tilde{S}_s(k)$ is obtained by applying the similarity between (2.2) and (2.41) to determine that $f_{\tilde{S}_s(k)}\left[\tilde{S}_s(k)\right]$ is of the same form as $f_{M(k)}\left[M(k)\right]$ in (2.39), and then accounting for the only difference between the right hand sides of (2.2) and (2.41) which is the scalar in the summation. Thus, the pdf of $\tilde{S}_s(k)$ is given as

$$f_{\tilde{S}_s(k)}\left[\tilde{S}_s(k)\right]=\left(\prod_{l=0}^{L-1}\lambda_l\right)\sum_{l=0}^{L-1}A_l\exp\left[-\lambda_l\tilde{S}_s(k)\right],\tilde{S}_s(k)\geq 0, \tag{2.42}$$

where $\lambda_l=\dfrac{1}{2\left(1-L\beta\rho^{L-l}\right)^2\sigma^2}$

2. General Case Detector Output pdf Analysis

This subsection first addresses the detector output pdf using quotient-combining with an AWGN plus BPSK signal input, next it adds the CW signal to the AWGN plus BPSK signal input, resulting in a mathematically intractable solution. These results motivate the use of heuristic methods to estimate $f_{\tilde{S}|x=i+n}(\tilde{S}\mid x=i+n)$, since the expression for $f_{\tilde{S}|x=i+n}(\tilde{S}\mid x=i+n)$ includes unknown joint pdf's, when the detector's input is the BPSK plus CW interference signal and AWGN for both combining methods. This subsection is presented as justification to obtain $f_{\tilde{S}|x=i+n}(\tilde{S}\mid x=i+n)$ using heuristic methods.

The pdf of the signals representing the detector's output in the quotient-combining case is now considered. The pdf of the ratio of two RVs is given by:

$$f_z(z)=\int_0^{\infty}yf_{xy}(yz,y)\,dy+\int_{-\infty}^{0}(-y)\,f_{xy}(yz,y)\,dy, \tag{2.43}$$

where *x* and *y* are RVs, $z=x/y$, and $f_{xy}(x,y)$ is the joint pdf of *x* and *y* [42]. Equation (2.43) simplifies to

$$f_z(z)=\int_0^{\infty}yf_{xy}(yz,y)\,dy, \tag{2.44}$$

when the RVs *x* and *y* are non-negative [42].Since the joint pdf of $M(k)$ and $Y_l(k)$ is not known, a less direct approach is taken. Letting

$$\tilde{M}_l(k) = M(k) - \rho^l Y_l(k) \tag{2.45}$$

we get from (2.45) and (2.5)

$$\tilde{S}_q(k) = \sum_{l=0}^{L-1} \frac{Y_l(k)}{\tilde{M}_l(k) + \rho^l Y_l(k)} = \sum_{l=0}^{L-1} \left[q_l(k) \right]^{-1}. \tag{2.46}$$

Inverting and algebraically manipulating the summand in (2.46), we get

$$q_l(k) = \frac{\tilde{M}_l(k)}{Y_l(k)} + \rho^l. \tag{2.47}$$

The RV $q_l(k)$ is the ratio of two independent, non-negative RVs plus a constant. The motivation for this manipulation is that since the RVs are independent a pdf of their ratio can be obtained. Taking into account the shifting represented by the constant, we obtain the inverse of the resulting RV and its pdf, which is the summand in (2.46).

The difference between the pdf of $\tilde{M}_l(k)$ and the pdf of $M(k)$ is that $\tilde{M}_l(k)'s$ pdf does not include the l^{th} term in either the summation or the product. Thus, the pdf of $\tilde{M}_l(k)$ is given by

$$f_{\tilde{M}_l(k)}\left[\tilde{M}_l(k) \right] = \left(\prod_{\substack{i=0 \\ i \neq l}}^{L-1} \lambda_i \right) \sum_{\substack{i=0 \\ i \neq l}}^{L-1} A_i \exp\left[-\lambda_i \tilde{M}_l(k) \right], \tilde{M}_l(k) \geq 0. \tag{2.48}$$

The joint pdf of the RVs $\tilde{M}_l(k)$ and $Y_l(k)$ is the product of their respective pdfs since they are independent. From (2.31) and (2.48) the joint pdf of $\tilde{M}_l(k)$ and $Y_l(k)$ is given by

$$f_{\tilde{M}_l(k)Y_l(k)}\left[\tilde{M}_l(k), Y_l(k) \right] = \lambda_l \exp\left[-\lambda_l Y_l(k) \right] \left(\prod_{\substack{i=0 \\ i \neq l}}^{L-1} \lambda_i \right) \sum_{\substack{i=0 \\ i \neq l}}^{L-1} A_i \exp\left[-\lambda_i \tilde{M}_l(k) \right], \tag{2.49}$$

where $Y_l(k) \geq 0$, $\tilde{M}_l(k) \geq 0$, and $\lambda_i = \dfrac{1}{2\left(\rho^i\right)^2 \sigma^2}$. The pdf of $q_l(k)$, using (2.8), (2.44), and (2.49), is

$$f_{q_l}\left(q_l(k)\right)=\int_0^{\infty}\left\{\tilde{M}_l(k)\lambda_l\exp\left[-\lambda_l q_l(k)\tilde{M}_l(k)\right]\times \left(\prod_{\substack{i=0\\ i\neq l}}^{L-1}\lambda_i\right)\sum_{\substack{i=0\\ i\neq l}}^{L-1}A_i\exp\left[-\lambda_i\tilde{M}_l(k)\right]\right\}d\tilde{M}_l(k). \tag{2.50}$$

The next step in obtaining the pdf of $\tilde{S}_q(k)$ is determined by recalling the relationship between $\tilde{S}_q(k)$ and $q_l(k)$ from (2.46) and (2.47), respectively. Since $q_l(k)$ is the inverse of the summand of (2.46), the pdf of $q_l(k)$ inverse is determined. The pdf of the inverse of a RV is

$$f_y(y)=\frac{1}{y^2}f_x\left(\frac{1}{y}\right) \tag{2.51}$$

where the function of the RV x is $y=1/x$ and $f_x(x)$ is the pdf of x [42]. From (2.50) and (2.51), the pdf of the inverse of $q_l(k)$ is

$$f_{q_l^{-1}}\left(q_l^{-1}(k)\right)=\left[q_l^{-1}(k)\right]^2\int_0^{\infty}\left\{\tilde{M}_l(k)\lambda_l\exp\left[-\lambda_l q_l^{-1}(k)\tilde{M}_l(k)\right]\times \left(\prod_{\substack{i=0\\ i\neq l}}^{L-1}\lambda_i\right)\sum_{\substack{i=0\\ i\neq l}}^{L-1}A_i\exp\left[-\lambda_i\tilde{M}_l(k)\right]\right\}d\tilde{M}_l(k). \tag{2.52}$$

The final step in solving for the pdf of $\tilde{S}_q(k)$ is to sum L $q_l^{-1}(k)$ RVs. Recall that the pdf of the sum of two RVs is [42]

$$f_z(z)=\int_{-\infty}^{\infty}f_{xy}(z-y,y)\,dy \tag{2.53}$$

where the summed RVs are x and y, and $z=x+y$. This leaves the issue of what the joint pdf of $f_{q_1^{-1}(k)q_2^{-1}(k)\ldots q_L^{-1}(k)}\left[q_1^{-1}(k),q_2^{-1}(k),\ldots,q_L^{-1}(k)\right]$ is. Since the RVs $q_l^{-1}(k)$, where $l=1,2,\ldots L$ are dependent RVs, the solution of

$f_{q_1^{-1}(k)q_2^{-1}(k)....q_L^{-1}(k)}\left[q_1^{-1}(k), q_2^{-1}(k), ..., q_L^{-1}(k)\right]$ is not trivial at this point. Before an analytic expression for $f_{\tilde{S}_q(k)}\left[\tilde{S}_q(k)\right]$ is pursued any further, the effect of CW interference is included.

The direct approach of adding the AWGN and the CW signal to the interference and then following the method used above to determine the desired pdf was considered. The pdf of the sum of AWGN and a CW signal is

$$f_p(p) = \frac{1}{2\pi^2}\int_0^{\pi} \exp\left[\frac{-(B\cos\theta - p)^2}{2\sigma^2}\right]\int_{-\infty}^{\infty} \exp\left(\frac{-\sigma^2 u^2}{2}\right) du\, d\theta, \qquad (2.54)$$

where *p* is a RV that represents the sum of AWGN and the CW signal, *B* is the maximum amplitude of the CW signal, θ is the phase of the CW signal which is modeled as a uniform random variable, and σ^2 is the variance of the AWGN [47]. Due to the complexity of (2.54), an analytic expression for the pdf of $Y_l(k)$ as in (2.31) was not determined. Since the FFT is a linear operation, summing the individually processed CW signal with the AWGN plus BPSK interference signal after the FFT is an equivalent alternative approach.

The delays shown in Figure 13 preceding the FFT inputs will, in general, cause the CW segments to appear as having different phases, as shown in Figure 19. The initial phase shown in branch one of Figure 19 is also unknown. At this juncture the research could focus on solving for $\theta_{l,c}$ for the $l = 0,1,...,L-1$ branches and the $c = 1,2,...,C$ frequencies of the CW tones, where *C* is 21 for this research. Alternatively, another approach is to model $\theta_{l,c}$, $l = 0,1,...,L-1$, $c = 1,2,...,C$, as uniform RVs.

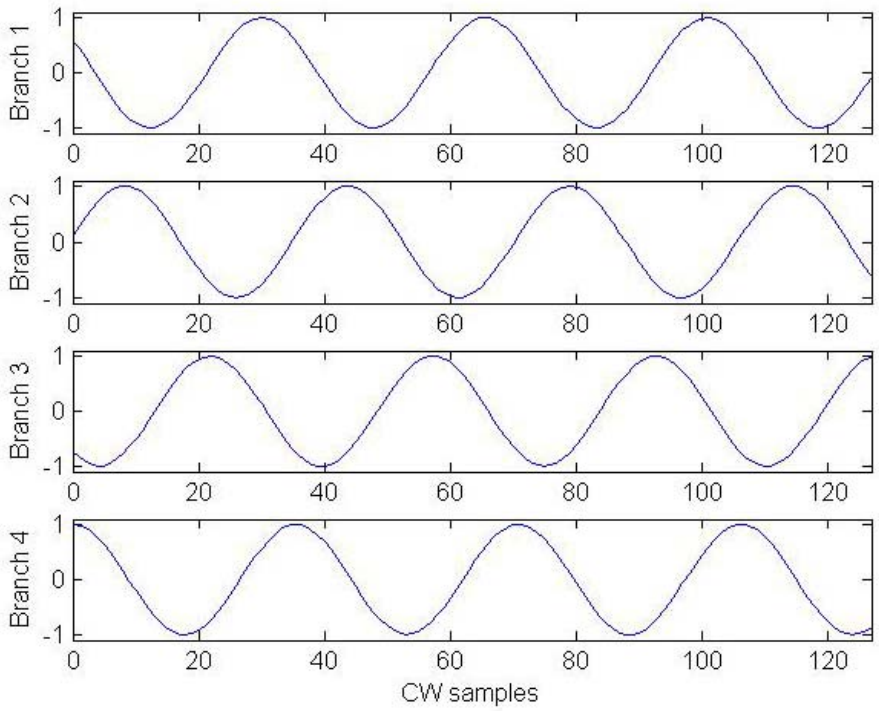

Figure 19 An example of the CW input in the first four branches, just prior to the FFT block.

A method to estimate $\theta_{l,c}$, $l = 0,1,...,L-1$ and $c = 1,2,...,C$ is presented in this paragraph and subsequently rejected due to its complexity. Energy detectors are used to estimate the *C* frequencies of the CW signal [11]. A phase-locked loop is used to estimate $\theta_{0,c}$ for each $c = 1,2,...,C$, and the values $\theta_{l,c}$, $l = 1,2...,L-1$ and $c = 1,2,...,C$ are obtained using the CW frequencies, the sampling frequency, and the segment length [20]. In this approach the FFT of the CW interference is no longer probabilistic but deterministic and can be combined with (2.27) using (2.8). The pdfs of $Y_l(k_c)$ $c = 1,2,...,C$ are then modeled as non-central, chi-squared distributions where k_c are the frequency bins that correspond to the *C* frequencies of the CW tones. Because of the complexity of this approach in estimating the CW frequencies and the phases, it was not pursued.

The approach taken is to model $\theta_{l,c}$, $l = 0,1,...,L-1$ and $c = 1,2,...,C$, as uniform RVs. The phases are identically distributed and each pdf is

$$f_{\theta_{l,c}}\left(\theta_{l,c}\right)=\frac{1}{2\pi}\text{rect}\left(\frac{\theta_{l,c}}{2\pi}\right), \tag{2.55}$$

where 'rect' is defined in (1.15). The CW interference is made up of *C* tones expressed as

$$v_{l,c}\left(t\right)=B\cos\left(2\pi f_{cw_c}t+\theta_{l,c}\right), \tag{2.56}$$

where f_{cw_c}, $c=1,2,...,C$ are the frequencies of each CW tone [5]. Using trigonometric identities, (2.56) can be rewritten as

$$v_{l,c}\left(t\right)=B\cos\left(\theta_{l,c}\right)\cos\left(2\pi f_{cw_c}t\right)-B\sin\left(\theta_{l,c}\right)\sin\left(2\pi f_{cw_c}t\right). \tag{2.57}$$

The Fourier transform of $v_{l,c}\left(t\right)$ is

$$V_{l,c}\left(f\right)=\int_{-\infty}^{\infty}\left\{B\left[\cos\left(\theta_{l,c}\right)\cos\left(2\pi f_{cw_c}t\right)-\sin\left(\theta_{l,c}\right)\sin\left(2\pi f_{cw_c}t\right)\right]\times \left[\cos\left(2\pi ft\right)-j\sin\left(2\pi ft\right)\right]\right\}dt \tag{2.58}$$

From the orthogonality of even and odd functions over the interval from negative infinity to positive infinity, the product of the *cosine* and *sine* functions go to zero, reducing (2.58) to [49]

$$\begin{aligned}V_{l,c}\left(f\right)=A\cos\left(\theta_{l,c}\right)\int_{-\infty}^{\infty}\cos\left(2\pi f_{cw_c}t\right)\cos\left(2\pi ft\right)dt+\\ jA\sin\left(\theta_{l,c}\right)\int_{-\infty}^{\infty}\sin\left(2\pi f_{cw_c}t\right)\sin\left(2\pi ft\right)dt.\end{aligned} \tag{2.59}$$

From [50] (2.59) simplifies to

$$\begin{aligned}V_{l,c}\left(f\right)=a_{l,c}\left[\delta\left(f-f_{cw_c}\right)+\delta\left(f+f_{cw_c}\right)\right]+\\ jb_{l,c}\left[\delta\left(f-f_{cw_c}\right)-\delta\left(f+f_{cw_c}\right)\right].\end{aligned} \tag{2.60}$$

where $a_{l,c}=\frac{B}{2}\cos\left(\theta_{l,c}\right)$ and $b_{l,c}=\frac{B}{2}\sin\left(\theta_{l,c}\right)$, as shown in Figure 20. Thus, the Fourier transform of the CW signal has non-zero values at plus and minus the CW frequencies. The discrete version of (2.60) is similar if the Nyquist criteria is met and if the data set used is sampled for an integer multiple of the period of the input sinusoid. Since there are multiple input sinusoids and none of their frequencies are known, the second condition is

not necessarily met, as the example in Figure 19 illustrates. However, the maximum non-zero input is still at plus and minus the CW frequencies, and the analysis first addresses these values.

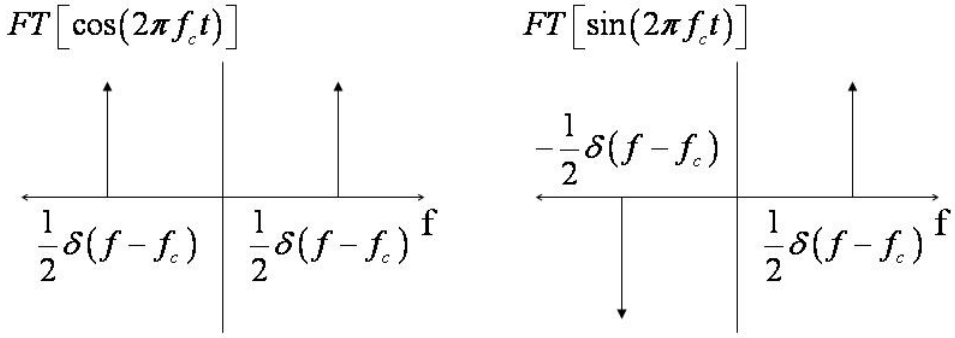

Figure 20 Fourier transform of sinusoids.

The next steps are to sum the RVs, take the absolute value squared of the summation, and derive the resulting pdf. The absolute value squared of the sum of the RVs influenced by the maximum non-zero CW input is

$$\tilde{Y}_l(k_c) = \left[X_{(l,i)}(k_c) + a_{l,c} \right]^2 + \left[X_{(l,q)}(k_c) + b_{l,c} \right]^2. \tag{2.61}$$

We can rewrite (2.61) as

$$\tilde{Y}_l(k_c) = X^2_{(l,i)}(k_c) + X^2_{(l,q)}(k_c) + 2a_{l,c}X_{(l,i)}(k_c) + 2b_{l,c}X_{(l,q)}(k_c) + {a_{l,c}}^2 + {b_{l,c}}^2. \tag{2.62}$$

The equation in (2.62) is further simplified to

$$\tilde{Y}_l(k_c) = \left\{ \left[X^2_{(l,i)}(k_c) + X^2_{(l,q)}(k_c) \right] + \frac{B^2}{4} \right\} + 2a_{l,c}X_{(l,i)}(k_c) + 2b_{l,c}X_{(l,q)}(k_c) \tag{2.63}$$

since ${a_{l,c}}^2 + {b_{l,c}}^2 = \frac{B^2}{4}$. As in (2.28) the pdf of the term in $[\cdot]$ is central chi-squared with two degrees of freedom. From (2.8) the pdf of the term in $\{\cdot\}$ is (2.30) where $Y_l(k_c)$ is shifted by $\frac{-B^2}{4}$.

The substitution of $b_{l,c}$ for $g\left(\theta_{l,c}\right)$ and (2.55) for $f_{\theta_{l,c}}\left(\theta_{l,c}\right)$ in (2.19) yields the characteristic function of $b_{l,c}$

$$\Phi_{b_{l,c}}(\omega)=\int_{-\infty}^{\infty}\exp\left[j\omega\frac{B}{2}\sin\left(\theta_{l,c}\right)\right]\frac{1}{2\pi}\operatorname{rect}\left(\frac{\theta_{l,c}}{2\pi}\right)d\theta_{l,c} \tag{2.64}$$

which can be further simplified to

$$\Phi_{b_{l,c}}(\omega)=\frac{1}{2\pi}\int_{-\pi}^{\pi}\exp\left[j\omega\frac{B}{2}\sin\left(\theta_{l,c}\right)\right]d\theta_{l,c}. \tag{2.65}$$

From [50] (2.65) is the Bessel function of the first kind and order zero:

$$\Phi_{b_{l,c}}(\omega)=J_0\left(\frac{B\omega}{2}\right). \tag{2.66}$$

The characteristic function of $a_{l,c}$ is obtained similarly, except an alternate representation of the Bessel function of the first kind and order zero, given by

$$J_0\left(z\right)=\frac{1}{\pi}\int_0^{\pi}\exp\left[\pm jz\cos\left(\theta\right)\right]d\theta \tag{2.67}$$

is used along with symmetry to produce [47, 50].

$$\Phi_{a_{l,c}}(\omega)=J_0\left(\frac{B\omega}{2}\right). \tag{2.68}$$

Substituting (2.68) for $a_{l,c}$ and (2.66) for $b_{l,c}$ into (2.10), we get the pdfs of $a_{l,c}$ and $b_{l,c}$ as

$$f_{a_{l,c}}\left(a_{l,c}\right)=\frac{1}{2\pi}\int_{-\infty}^{\infty}J_0\left(\frac{B\omega}{2}\right)\exp\left(-j\omega a_{l,c}\right)d\omega \tag{2.69}$$

$$f_{b_{l,c}}\left(b_{l,c}\right)=\frac{1}{2\pi}\int_{-\infty}^{\infty}J_0\left(\frac{B\omega}{2}\right)\exp\left(-j\omega b_{l,c}\right)d\omega, \tag{2.70}$$

respectively.

The pdf of the product of two RVs is

$$f_z\left(z\right)=\int_{-\infty}^{\infty}\frac{1}{|x|}f_{xy}\left(x,\frac{z}{x}\right)dx \tag{2.71}$$

where the function of the RV z is $z=xy$ and $f_{xy}\left(x,y\right)$ is the joint pdf of x and y [42]. Since $a_{l,c}$ and $X_{(l,i)}(k_c)$ are independent RVs, (2.71) is used to determine the pdf of the

term $2a_{l,c}X_{(l,i)}(k_c)$, where the constant is accounted for by applying (2.8). The pdf of $2b_{l,c}X_{(l,q)}(k_c)$ may be obtained in a similar manner. The last step in finding the pdf of $\tilde{Y}_l(k_c)$ in (2.63) is to use (2.53) to sum the RVs $2a_{l,c}X_{(l,i)}(k_c)$, $2b_{l,c}X_{(l,q)}(k_c)$, and $Y_l(k_c)$ shifted by $\frac{-B^2}{4}$. Since the RVs are not independent their joint pdf does not equal the product of their individual pdfs. Thus, an analytic solution for $f_{\tilde{S}|x=i+n}(\tilde{S} \mid x = i+n)$ is mathematically intractable.

The exponential averaging FH detector along with the signals and metrics used with the detector were presented in this chapter. The detector's two combining methods, quotient and scaled-subtraction-combining, were discussed. The analytic solution to the pdf that models the detector's output with scaled-subtraction-combining and an AWGN plus BPSK input was developed. Finally, it was shown that an analytic expression for the pdf that models the detector's output with either combining method and an AWGN plus BPSK plus CW input is mathematically intractable using the given approach. Therefore, a heuristic approach to estimating the pdf of $f_{\tilde{S}|x=i+n}(\tilde{S} \mid x = i+n)$ is addressed in the next chapter.

III. EXPONENTIAL AVERAGING DETECTOR SIMULATION METHODS AND RESULTS

This chapter describes the exponential averaging detector's simulation set-up, develops the decision criteria selected and presents simulation results. The simulation set-up includes a description of the various parameters and signals used. The decision criteria section investigates two methods to heuristically estimate the pdf of the RV that models the detector's output; histograms and goodness-of-fit tests. Simulation results include performance guidelines, a sample histogram of the data, and an evaluation of goodness-of-fit tests considered in this work, a postulated pdf of the RV representing the detector's output supported with probability plots of the data, the selection of a threshold, and an evaluation of the detector's performance.

Simulations discussed in this chapter were generated using MATLAB. The FH-MSK, BPSK, and CW signals used are approximately 20 ms long, with a sampling frequency equal to 50 MHz (i.e. 1,032,192 samples). The FFT length used to compute the spectrum was generally set to a power of 2. A minimum spectral resolution of 24 kHz is assumed for the simulations resulting in a minimum FFT length equal to 2^{11}. The minimum number of points in the FFT is used unless stated otherwise. The minimum spectral resolution assumption is based on a-priori knowledge of the modulation type, hop rate, and the minimum frequency spacing required for signal orthogonality. Initial results obtained after zero padding the data to increase the spectral resolution did not yield a substantial improvements and therefore zero padding was not considered further. The search range selected for the simulations was from 0 to 25 MHz. The frequency hops of interest lie between 6 and 13 MHz. For this reason, the *x* axis of the figures displaying the frequency response is limited from 5 to 15 MHz, even though the data is processed between 0 and 25 MHz.

A. INTERFERENCE/NOISE SPECTRUM ESTIMATION

The scaled spectral estimate of the interference shown earlier in Figure 17 plus AWGN is generated using (2.2) and is shown in Figure 21 for SIR equaling zero dB and

SNR equaling nine dB. Figure 21 is comparable with Figure 17 which does not include AWGN since a relatively large value of SNR compared to SIR is used. The spectrum is generated using a 2^{14} point FFT which is eight times larger than the minimum FFT length so that Figure 21 compares better with Figure 17, which was generated using a 2^{20} point FFT. A direct comparison with a 2^{20} point FFT cannot be done without zero padding since the data is segmented to facilitate exponential averaging. Although the different scaling of Figure 17 and Figure 21 does not show it clearly, Figure 21 has a larger average magnitude than Figure 17. This phenomenon is attributed to the fact that the results in Figure 21 include a FH signal and AWGN, which are not included in Figure 17. The SIR and SNR are obtained by holding the FH signal amplitude constant and varying the power of the interference and AWGN signals to obtain the desired SIR and SNR, respectively.

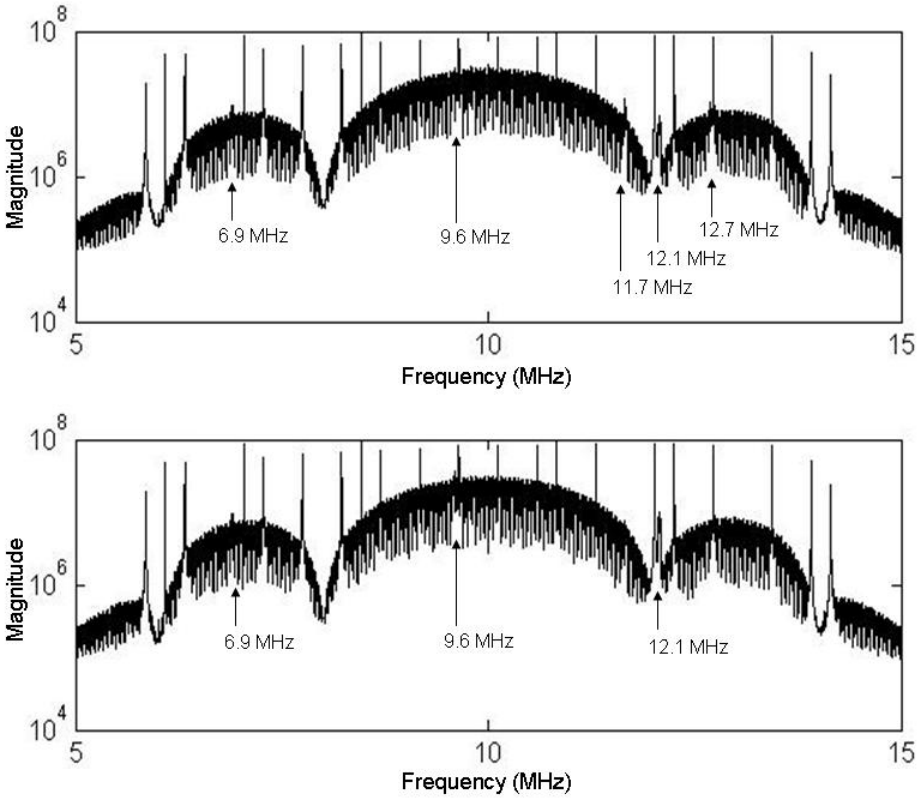

Figure 21 Scaled spectral interference estimates for $\rho = 0.99$ (top) and $\rho = 0.9$ (bottom).

Two interference-plus-AWGN spectral estimates are shown in Figure 21 to illustrate the influence of ρ on the estimate. The two most noticeable differences between the two estimates are the emerging spike at 11.7 MHz when $\rho = 0.99$ and the slightly larger magnitude of the spike at 12.1 MHz when $\rho = 0.9$. Less obvious are differences at 6.9, 9.6, and 12.7 MHz. The spikes at 9.6, and 12.7 MHz are somewhat obscured on this scale since they are within 75 and 35 kHz, respectively, of CW signals. The spike at 12.1 MHz is not obscured by the CW signal that is within 50 kHz since it is in a null of the BPSK spectrum. The spikes are components of the FH-MSK signal. From these observations, it can be deduced that different values of ρ suppress components of the FH signal differently. A method for exploiting this behavior is discussed in the next section.

B. FH SIGNAL SPECTRUM ESTIMATION

Variations in the emphasis of the FH signal due to changing ρ can be exploited using the quotient and scaled-subtraction combining methods described in Section I.A. The exponential averaging detector's output with quotient-combining is shown in Figure 22 with SNR and SIR equal to zero and a 2^{13} point FFT. The numbers 1 through 7 in Figure 22 show the temporal hop order with seven being the most recent hop. A few of the factors that contribute to the variance in the magnitude of the hop frequencies in the spectral FH signal estimate are: the interference spectrum near the hop frequency, the BW of each FFT bin and the BW of the FH-SS, the SNR level, and the value of ρ. Trends in the hop magnitude variability are discussed; however a detailed explanation of the influence from each of these factors on the hop magnitude variability is reserved for future work.

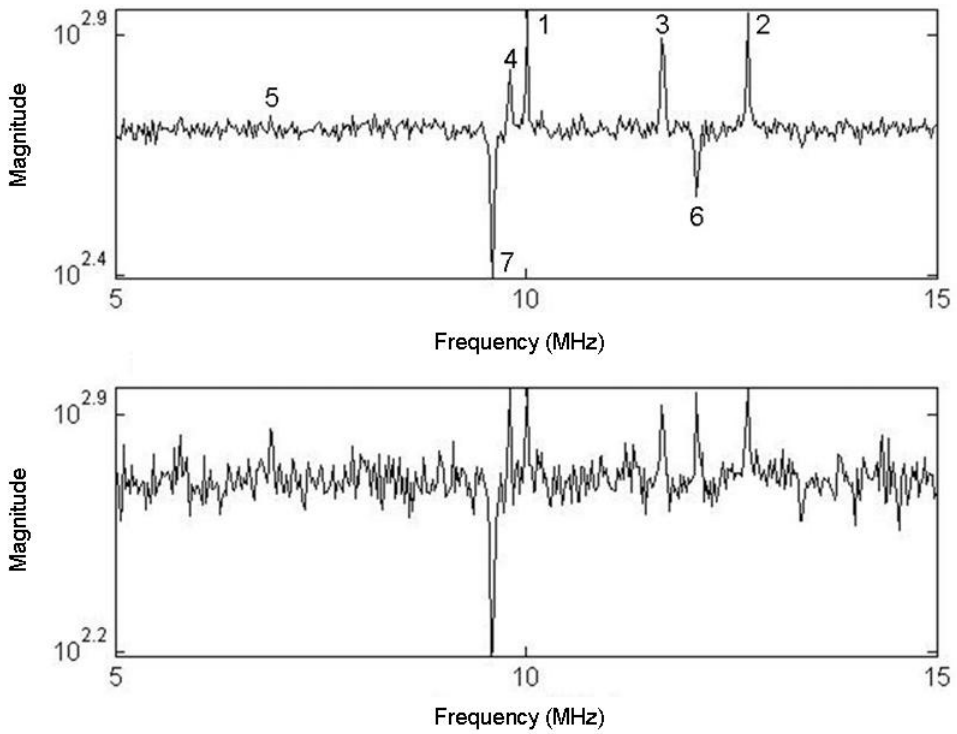

Figure 22 Spectral FH signal estimate using quotient-combining for $\rho = 0.99$ (top) and $\rho = 0.9$ (bottom).

It is speculated that, the dips in the spectral FH signal estimation in the top plot of Figure 22 at hops six and seven are attributed to the over emphasis of those hops in the noise plus interference spectral estimate. Hops one through four are underestimated or suppressed in the noise plus interference spectral estimate which result in peaks. Hop number five is not shown in the top plot of Figure 22 since it is proportionally estimated in the noise plus interference spectral estimate. The smaller value of $\rho = 0.9$ in the bottom plot in Figure 22 shows similar results except that the shift between positive and negative hops occurs quicker and allows hop number five to potentially be detected. Finally, Figure 22 shows that the noise variance significantly increases as ρ decreases.

The exponential averaging detector's output with scaled-subtraction-combining is shown in Figure 23 with SNR and SIR equal to zero and a 2^{13} point FFT. The phenomenon of the hops shifting from above to below the noise floor does not occur with scaled-subtraction-combining as it does with quotient combining, nor does the noise floor

variance increase as significantly as ρ decreases. The quotient-combining method is more sensitive to changes in ρ with respect to the lower noise floor variance and, thus, requires a larger ρ value to maintain a certain performance level. The scaled-subtraction-combining method is less sensitive to the perturbation and has similar performance levels for the range $0.8 < \rho < 1$. Although a better understanding of the factors contributing to the magnitude variance could lead to further exploiting the differences mentioned (i.e.; hop order estimation) this area of research is reserved for future work.

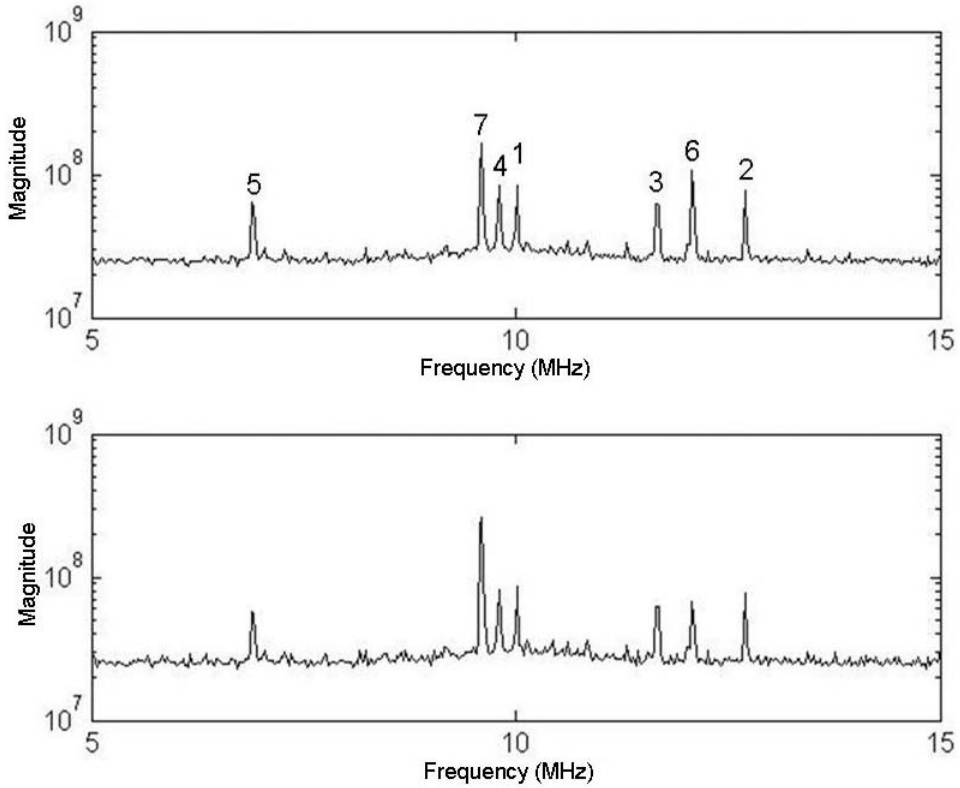

Figure 23 Spectral FH signal estimate using scaled-subtraction-combining for $\rho = 0.99$ (top) and $\rho = 0.9$ (bottom).

This difference in sensitivity relegates the quotient-combining method to values of ρ relatively close to one. Since the contribution of earlier segments increases as the

value of ρ approaches one, more data segments are needed when ρ is closer to one. This result indicates that the quotient-combining method requires more data segments than does the scaled-subtraction method. As the SIR and SNR are lowered, however, the quotient-combining method outperforms the scaled-subtraction-combining method as shown in Table 1 and Table 2. The values in the tables are generated using a few simulations and are representative of general trends observed. The Table 1 and Table 2 results are presented as performance guidelines versus performance measures since they were evaluated visually and do not include any probabilistic measures.

Table 1 Number of frequency hops visually detected by the exponential averaging FH detector given a seven hop FH/MSK signal, quotient-combining, and respective SNR and SIR.

SNR dB (across) SIR dB (down)	0	-3	-6	-9	-12
2	6	6	6	6	5
-1	6	6	6	6	4
-4	6	6	6	5	4
-7	6	6	5	5	3
-10	4	4	4	4	2
-13	3	3	2	2	1
-16	1	1	0	0	0

Table 2 Number of frequency hops visually detected by the exponential averaging FH detector given a seven hop FH/MSK signal, scaled-subtraction-combining and respective SNR and SIR.

SNR dB (across) SIR dB (down)	0	-3	-6	-9	-12
2	7	7	7	7	2
-1	7	7	7	7	2
-4	7	7	5	3	1
-7	5	4	3	2	0
-10	2	1	1	1	0

C. DECISION CRITERIA TOOLS

The decision criteria are determined by estimating P_f and solving for the decision threshold γ using (1.6). The heuristic estimation of $f_{\tilde{S}|x=i+n}(\tilde{S} \mid x = i+n)$ is addressed in this section to obtain the threshold γ. Three methods to estimate $f_{\tilde{S}|x=i+n}(\tilde{S} \mid x = i+n)$ heuristically are discussed; first we consider a histogram based scheme to estimate the data pdf or cumulative distribution function (CDF). Next, we investigate a model based scheme where we hypothesize a specific distribution and then test the data against the hypothesis to determine if their similarities are statistically significant using a goodness-of-fit test [51]. Finally, we cover graphical analysis, which is an easy and common way of supporting a postulated distribution without providing any objective statistical measure with which to evaluate how well the postulated distribution matches the data [52]

The probability plotting and the goodness-of-fit based method have the advantage of modeling the required pdf with a specifically defined function, which may provide a better understanding of the process, whereas the histogram estimate of the pdf is a purely heuristic approximation. The goodness-of-fit based scheme is preferred to the probability plotting and histogram schemes since it produces a statistical measure of significance, when the goodness-of-fit test requirements are met and a hypothesized pdf can be determined with a sufficient confidence to justify the increased complexity of the goodness-of-fit test(s).

Note that a maximum-likelihood simulation based approach may also be used to estimate the pdf. Classical maximum-likelihood estimation can be summarized as finding the value of θ that maximizes the likelihood of

$$f_n\left(\vec{\mathrm{x}}\right) = \prod_{m=1}^{n} f\left(\vec{\mathrm{x}}_{\mathrm{m}} \mid \theta\right), \tag{3.1}$$

where $\vec{\mathrm{x}}_{\mathrm{m}}$ is vector of *n* IID RVs, and θ is an unknown parameter in $f\left(x\right)$ [53]. We selected not to pursue this approach further because we assume $f\left(x\right)$ to be known a-priori; and there is no indicator in the maximum-likelihood method to determine how inaccurate $f\left(x\right)$ is when the assumption is incorrect.

1. The Histogram as a pdf Estimator

The oldest and most commonly used pdf estimator is the histogram [54]. A histogram is a graphical representation of the number of events in adjacent intervals over a given range. To generate a histogram, we divide the range $[a,b]$ into N equally wide bins $s_n = \left[a + (n-1)\left(\frac{a+b}{2}\right), a + n\left(\frac{a+b}{2}\right)\right]$ where $n = 1,2,...,N$, sum the number of events M that occur in each bin x_n, $(n = 1,2,...,N)$, and plot the value of x_n over the corresponding bin interval s_n. The histogram pdf estimate $\tilde{f}_x(\mathrm{x})$ is then scaled by $\frac{N}{(b-a)M}$ so that $\int_a^b \tilde{f}_x(x)dx = 1$.

An issue with histogram pdf estimation is that $\tilde{f}_x(x)$ has up to $N+1$ discontinuities at the intersections of the bins. Thus, this method of construction leaves room for improvement when $f_x(x)$ is assumed to be smooth. A simple approach to smooth $\tilde{f}_x(x)$ is to use spline interpolation [53]. Another approach is to apply a windowing function scaled by x_n at the center of each bin and sum the results to determine $\tilde{f}_x(x)$. The windowing function is called a kernel, and a Gaussian shape is an example of a commonly used kernel [53, 54]. Reference [55] calls the process described above Parzen's estimator.

The histogram pdf estimate $\tilde{f}_x(x)$ is still defined on a truncated range and models when $f_x(x)$ has an infinite range such that [53]

$$\tilde{f}_x(x) = \begin{cases} \dfrac{f_x(x)}{\int_a^b f_x(x)\,dx} & \text{for } a \le x \le b \\ 0 & \text{otherwise.} \end{cases} \tag{3.2}$$

Note that the accuracy of $\tilde{f}_x(x)$ increases as *M* increases, as shown by the fact that the mean squared error (MSE) of $\tilde{f}_x(\mathrm{x})$ goes to zero as $M \to \infty$ [53]. The accuracy of $\tilde{f}_x(x)$ is also dependent on *N* and how histogram discontinuities are smoothed out.

The selection of *N* can be based on different rules of thumb such as using seven to ten bins, $N = \sqrt{M}$, $N = 10\log(M)$ for $M > 30$, or some scaled version of these rules [56]. One analytic method to determine *N* is based on minimizing the mean integrated squared error (MISE) defined as [54]

$$MISE\left[\tilde{f}_x(x)\right] \equiv \frac{1}{T}\int_0^T E\left[\tilde{f}_x(x) - f_x(x)\right]^2 dx. \tag{3.3}$$

The value of *N* that minimizes the MISE is determined by minimizing the parameter *C* defined as

$$C = \frac{(2k - \nu)}{\Delta^2}, \tag{3.4}$$

where the mean of the events in the bins is equal to $k = \frac{1}{N}\sum_{n=1}^{N} x_n$, the variance of the events in the bins $\nu = \frac{1}{N}\sum_{n=1}^{N}(x_n - k)^2$, and the bin width $\Delta = \frac{b-a}{N}$ [57].

2. Goodness-of-Fit Tests

Estimating the pdf type through hypothesis testing has the major disadvantage that the test is only valid for a specified distribution. However, the test produces a metric by which to judge how well the data matches the specified distribution. There are different types of goodness-of-fit tests. This discussion focuses on specific tests and then moves to a more general discussion.

The Kolmogorov-Smirnov (K-S) test described in [51] and [58] compares a *empirical* or *heuristic* CDF $F_M(x)$ with the hypothesized CDF $F(x)$ and then evaluates the distribution of the result, which is not dependent on $F(x)$ when it is continuous. The function $F_M(x)$ is generated by summing the number of events X_i that are less than *x* and dividing by the total number of events *M*; i.e.,

$$F_M(x) = \frac{\text{number of } X_1, X_2, ..., X_M \text{ that are} \le x}{M}, \tag{3.5}$$

where X_i, $i = 1, 2, ..., M$ are independent observations [58, 59]. The two components to the comparison of $F(x)$ and $F_M(x)$ are [58]

$$\begin{aligned} K_M^+ &= \sqrt{M}\ \max\left[F_M(x) - F(x)\right], \\ K_M^- &= \sqrt{M}\ \min\left[F(x) - F_M(x)\right]. \end{aligned} \tag{3.6}$$

The statistical significance of $F_M(x)$ with respect to $F(x)$ is then reduced to a table look up using K_M^+ and K_M^- [58].

A possible application of the K-S test in this research is to select $F(x)$ as the histogram pdf estimate and evaluate how well additional data fits the hypothesized $F(x)$. Another application is to examine the histogram of the data and determine if it visually compares well with any known distributions and then use those distributions as $F(x)$. However, the K-S test cannot be used since $F(x)$'s parameters should *not* be estimated from the data itself, and no other mean and variance estimates are known [51]. Further, another drawback of the K-S test is that it is most sensitive to data at the median of the distribution. Therefore, other goodness-of-fit tests without such drawbacks are considered next.

Perhaps the best known, most used, and oldest goodness-of-fit test is the chi-squared test, which was introduced by Karl Pearson in 1900 [51], [52], and [58]. The chi-squared test is similar to the histogram in that the test first divides the data into *N* adjacent intervals or bins $[a_0, a_1), [a_1, a_2), ..., [a_{N-1}, a_N]$, where x_n $n = 1, 2, ..., N$ equals the number of data points in the n^{th} interval [51]. If $a_0 = -\infty$ or $a_N \to \infty$, then the appropriate inclusive square brace is changed to a exclusive curved brace [51]. The test statistic is given by

$$\chi^2 = \sum_{n=1}^{N} \frac{\left(x_n - M\breve{f}_n\right)^2}{Mf_n}, \tag{3.7}$$

where M is the total number of data points, and $\breve{f}_n = \int_{a_{n-1}}^{a_n} \breve{f}_x(x)dx$, where $\breve{f}_x(x)$ is the hypothesized pdf. As the name indicates, the test statistic is modeled as a chi-squared RV regardless of $\breve{f}_x(x)$. If the hypothesis is true, then the distribution of χ^2 converges to chi-squared with degree-of-freedom $N-1$ as $M \to \infty$ when the data is independent [51, 59, 60].

Unlike the K-S test, the chi-squared test is valid when $\breve{f}_x(x)$ parameters are estimated using the data. For the case when the mean and variance are estimated to specify a Gaussian pdf as $\breve{f}_x(x)$, the degree-of-freedom for χ^2's pdf is reduced by two [61]. Tables of χ^2 with respect to the acceptance or rejection of the null hypothesis are provided in [58], [61], and [62].

Comparing the performance between two similar schemes such as the K-S test and the chi-squared goodness-of-fit tests becomes an issue. According to [63], [64], and [65], the advantages of the K-S test over the chi-squared test is that the K-S test is valid with smaller data sets than the chi-squared test, and for any data set size it appears to be a more accurate test. Hubert Lilliefors modified the K-S test so that data estimated pdf parameters can be included in the hypothesized pdf [65]. The advantages of the K-S test over the chi-squared test are maintained with the modified K-S test. The modified K-S test in [65] is now known as the Lilliefors' test. Tables of the statistical significance of Lilliefors' test statistic are computed using Monte Carlo simulations and may be found in [65].

Goodness-of-fit tests can be separated into five broad categories: the chi-squared test, empirical distribution function (edf) tests, moment tests, regression tests, and miscellaneous tests [52]. The chi-squared test is the only test in the chi-squared test category, while the K-S test and the Lilliefors' test are edf tests. The inclusion of a moment test provides broad coverage of the goodness-of-fit test categories.

There are a number of goodness-of-fit tests in the moment category including the first one introduced by Karl Pearson in 1895 [52]. The Jarque-Bera (J-B) test, or Bera-

Jarque test, depending on the author, is selected as the moment categorized goodness-of-fit test since it uses multiple moments. As a side note, the original papers list Bera first, but placing Jarque first is more common in the literature, so J-B is used here. The J-B test is designed to determine if data can be accepted or rejected as Gaussian distributed data within a specified statistically significance, by using the properties of the third and fourth standard moments of a Gaussian distribution. The third standard moment is also called the measure of skewness or just skewness b_1. The fourth standard moment is also called the measure of kurtosis or just kurtosis b_2. The skewness is a measure of symmetry and is defined as

$$b_1 \equiv \frac{\mu_3}{\sigma^3}, \tag{3.8}$$

where μ_i is the i^{th} moment, and σ is the standard deviation or $\sqrt{\mu_2}$ [66]. The kurtosis is a measure of peakness and is defined as [66]

$$b_2 \equiv \frac{\mu_4}{\sigma^4}. \tag{3.9}$$

For a Gaussian pdf $b_{1\,G} = 0$ which shows that the pdf is symmetric and $b_{2\,G} = 3$. Some texts use excess kurtosis $b_{2\,excess} = b_2 - 3$ versus kurtosis, so that the skewness and excess kurtosis of a Gaussian pdf are both equal to zero.

The J-B test statistic is defined as

$$\lambda \equiv M\left[\frac{\tilde{b}_1}{6} + \frac{\left(\tilde{b}_2 - 3\right)^2}{24}\right], \tag{3.10}$$

where M is the number of data samples x_m $m = 1, 2, ..., M$, and $\tilde{b}_1$ and $\tilde{b}_2$ are generated by substituting the data estimated appropriate i^{th} moments $\tilde{\mu}_i = \frac{1}{M}\sum_{m=1}^{M} x_m^i$ into (3.8) and (3.9), respectively [66]. It has been shown that the pdf of the test statistic λ converges to a chi-squared distribution with two degrees of freedom as $M \to \infty$ [66]. We note the J-B test is sensitive to outlying data points since it is based on multiple moments [67].

3. Graphical Analysis

Graphical analysis has the disadvantages of being less formal and producing subjective results which are evaluated visually and the advantages that it is easily implemented and commonly accepted in engineering analysis [52]. The histogram plotted with an equation can be a method of graphical analysis as shown in Figure 24, which plots a histogram of the exponential averaging detector's output and compares it to a Gaussian pdf (red line). This graphical analysis provides visual support that the exponential averaging detector's output can be modeled as a Gaussian pdf.

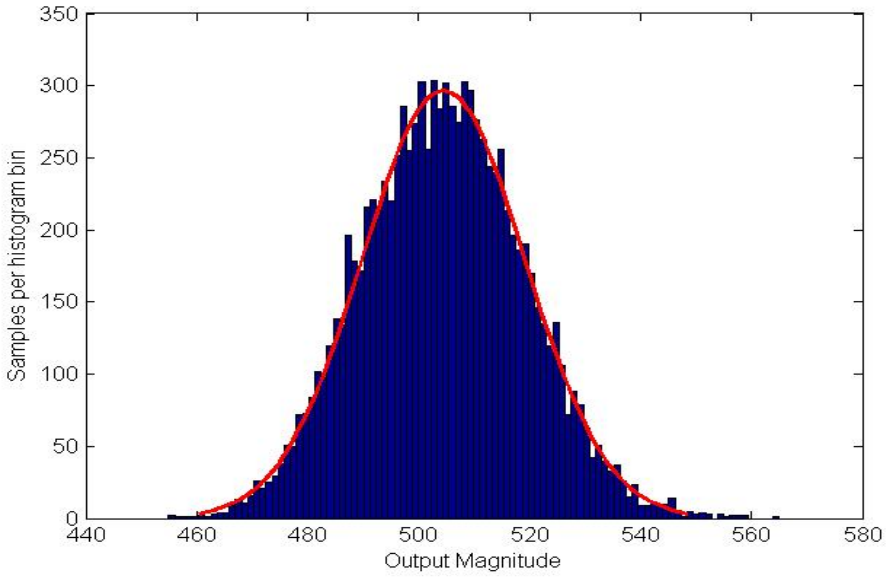

Figure 24 Gaussian estimate (line) and histogram of a single frequency bin component within the composite spectral estimation.

The empirical CDF used in the K-S test, (3.5), can be plotted and compared with a hypothesized CDF to graphically analyze the data, as shown in Figure 25, where the 25 data elements used to construct the empirical CDF were randomly generated with the hypothesized CDF expression. The results in Figure 25 represent the worst visual comparison between the empirical CDF and hypothesized CDF for a dozen simulations to illustrate the errors associated with graphical analysis compounded by the use of a small

data set. The estimated CDF parameters can be obtained by iteratively least-squares-fitting the data and the hypothesized CDF, where the least-squares-fit is the minimum sum of the squares of the residuals of the data and the hypothesized CDF.

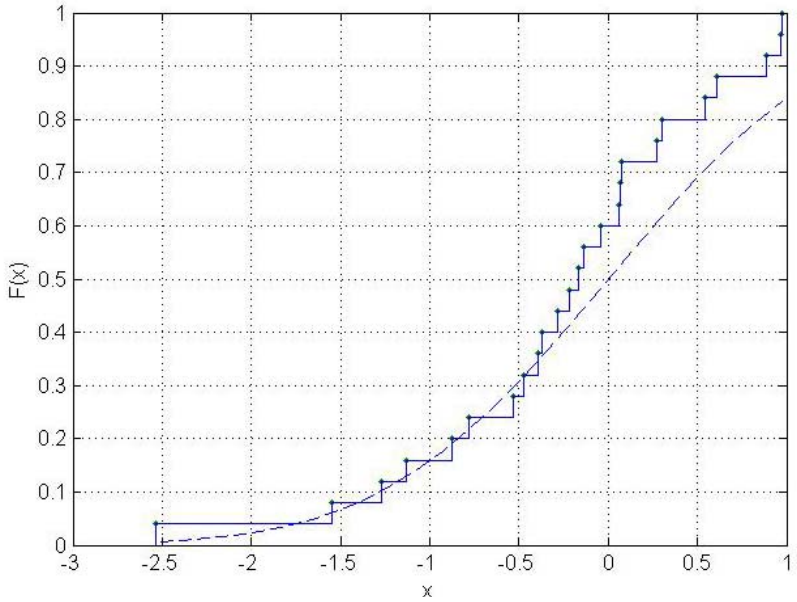

Figure 25 Empirical CDF (solid line with data points) and hypothesized CDF (dashed line).

The quantile versus quantile (qq) plot is another way to visually compare data to a distribution, which transforms the hypothesized distribution into a straight line so that the linearity of the transformed data illustrates the relation between the hypothesized distribution and the data. A quantile is a segment taken at a regular interval; i.e., each quantile is a percentile when there are one hundred quantiles. The qq plot plots the quantiles of the distribution versus the quantiles of the data. The qq plot is most susceptible to error at the tail regions of the pdf. The qq plot of a sample of the exponential averaging detector's output and that of a Gaussian pdf are shown in Figure 26, and support the postulate that the exponential averaging detector's output can be modeled as a Gaussian RV. Note that data mean on the *y*-axis corresponds to zero on the *x*-axis, and the variance is the slope when the qq-plot distribution and data are Gaussian.

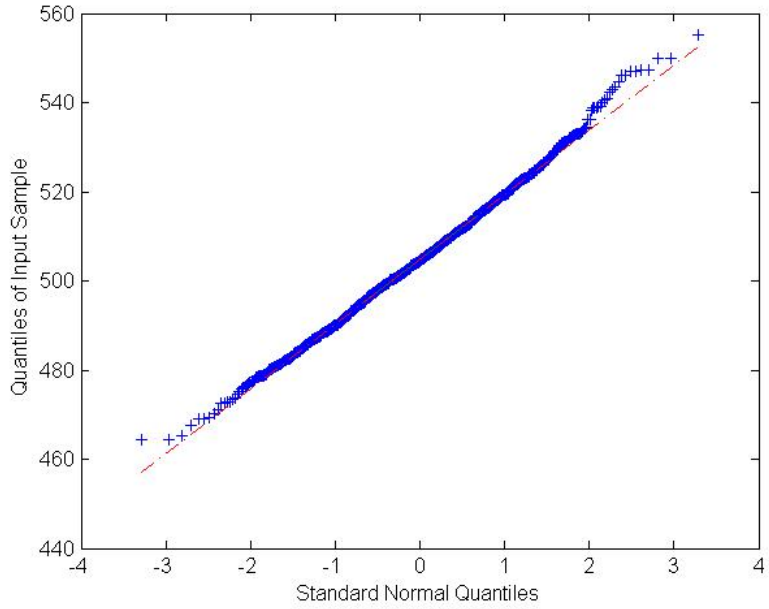

Figure 26 QQ plot of output data from the exponential averaging detector versus a Gaussian distribution.

D. SIMULATION RESULTS

The two areas of focus with respect to the simulation results are the generation of the decision criteria and an appraisal of the detector's performance. Simulations are performed using MATLAB, where intrinsic MATLAB functions are used when available. From (1.6) and Figure 13, the two parameters required to obtain the threshold are P_f and $f_{\tilde{S}(k)|x=i+n}\left[\tilde{S}(k) \mid x = i+n\right]$, $k = 0,1,...,N-1$, where N is the number of FFT bins. The value of P_f is based on performance parameters which are subjectively chosen. The value of $N = 2^{11}$. To narrow the scope of the dissertation, the remainder of the exponential averaging research uses quotient-combining since quotient-combining has performance advantages over scaled-subtraction-combining at low SNR values, as shown in Table 1 and Table 2.

1. Detector Output Distribution Graphical Analysis

Based on the ranges of NIR used in the simulation detector performance appraisal in Subsection III.D.4, the values of NIR considered are 10 through -10 dB, and $\rho = 0.99$. The data matrices used in the plots have dimensions $1,000$ by $1,024$ where the first dimension represents the number of times the detector simulation was run with AWGN and interference inputs, and the second dimension corresponds to the minimum number of positive frequency FFT bins, covering frequencies 0 to 25 MHz. The number of detector simulations chosen was based on trying different numbers of simulations and subjectively choosing 1,000. Histograms with a Gaussian fit and qq-plots for all positive frequency bins are visually comparable and support the postulate that the detector's output can be modeled as a Gaussian RV when $\rho = 0.99$ and NIR ranges from 10 to -10 dB. A random cross section of the results when $\rho = 0.99$ and NIR$= -10$ dB is shown in Figure 27 and Figure 28.

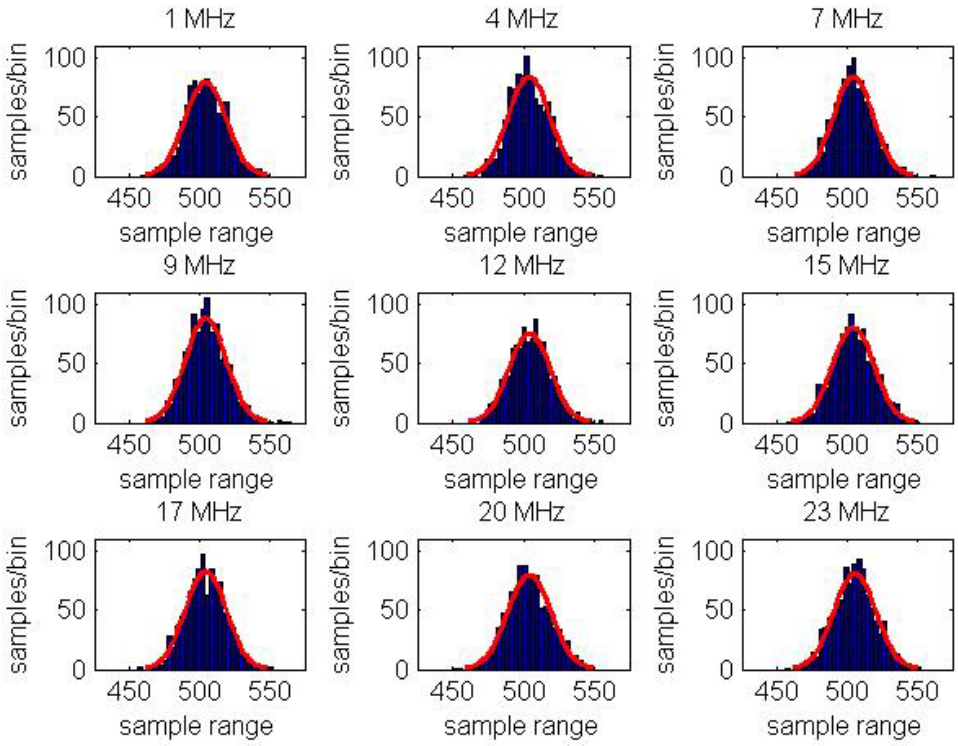

Figure 27 Gaussian estimate (line) and histogram of nine frequency bins from the output of the exponential averaging detector with NIR$= -10$ and $\rho = 0.99$.

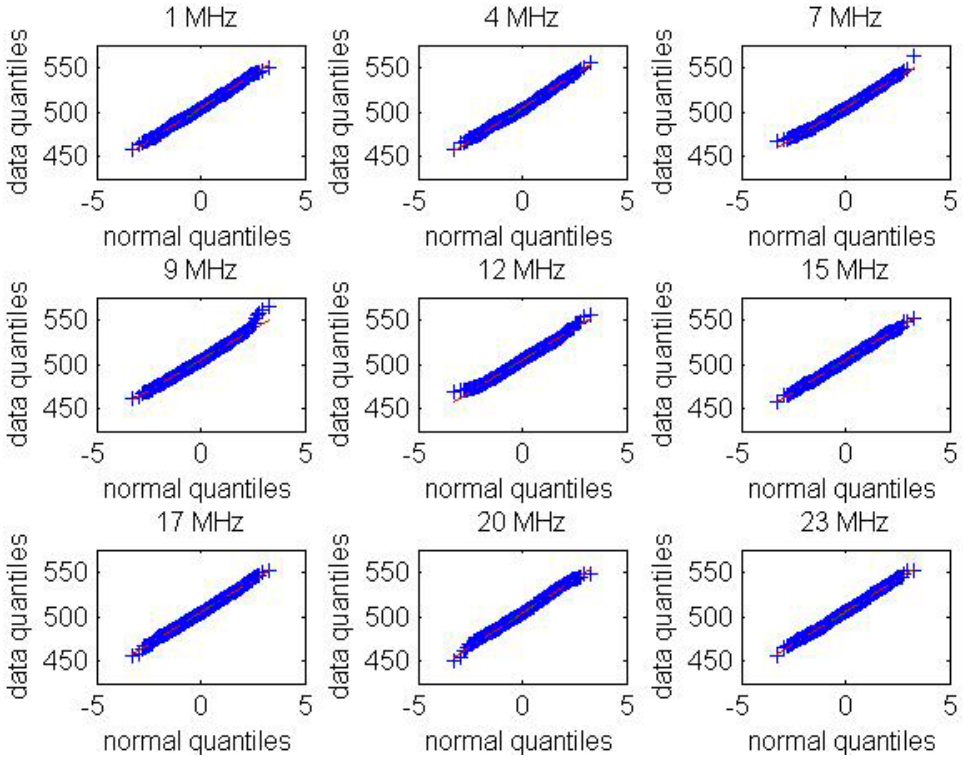

Figure 28 QQ plot of output data of nine frequency bins from the output of the exponential averaging detector with NIR= –10 and $\rho = 0.99$.

Further validation of the Gaussian postulate is recommended for future work due to the disadvantages of this approach as discussed in Section III.C. Additional simulations when $\rho < 0.99$ showed significantly different results, and this trend is considered in the next subsection using the goodness-of-fit tests discussed in Subsection III.C.2.

2. Distribution Model Trend Analysis

The three goodness-of-fit tests are used to analyze the distribution model trend. The three steps used to analyze the distribution model trend are:

1) evaluate the goodness-of-fit tests using Gaussian distributed random numbers,

2) evaluate the goodness-of-fit results when evaluating a distribution where changing parameters makes it visually more similar to a Gaussian.

3) evaluate the data trend from the output of the exponential averaging detector as ρ changes when it is processed by the goodness-of-fit tests and compare the results to the performance measures determined in the previous two steps.

The goodness-of-fit tests output can be viewed as a binary output of either accept or reject the null hypothesis that the data has a Gaussian distribution for a specific statistical significance α [51, 52 58]. The value of α corresponds to the probability that the data has a Gaussian distribution but the null hypothesis is rejected, i.e., α is the probability of false rejection of the null hypothesis. The output of the goodness-of-fit tests can instead be the value of α at which the test transitions from accepting to rejecting the null hypothesis. A common value of α for the goodness-of-fit tests used in this research is 0.05 [42, 51, 52, 58].

The data matrices used in the tests have dimensions $1,024$ by $1,000$ as in Subsection III.D.1. Simulations used to evaluate steps one through three use the goodness-of-fit test binary output of either accepting or rejecting the null hypothesis. The binary goodness-of-fit output is generated for the 1,024 rows of data. The value of α is linearly incremented over the range $0.01 \le \alpha \le 0.2$. Test results are plotted as α versus the unit normalized number of data rows where the goodness-of-fit test rejects the null hypothesis. The unit normalization maps the range $[0, 1024]$ to $[0, 1]$, to allow for a direct comparison between *x* and *y* axes.

The evaluation of the goodness-of-fit tests using Gaussian distributed random numbers (solid line) is shown in Figure 29. Note that Figure 29 includes the plot of α versus α (dashed line) as a frame of reference to illustrate the rate which Gaussian distributed random sequences are expected to be rejected by the goodness-of-fit tests. As expected, the number of rejections of the Gaussian distributed random numbers (solid line) increases as α increases. Figure 29 also provides a visual representation of the minimum amount of error that can be expected from the goodness-of-fit tests when evaluating Gaussian distributed data. Thus, data which is tested cannot be expected to be

closer to the reference (dashed line) than the Gaussian distributed random sequences (solid line) are. The solid line plots in Figure 29 are included as a performance reference in all goodness-of-fit plots that follow.

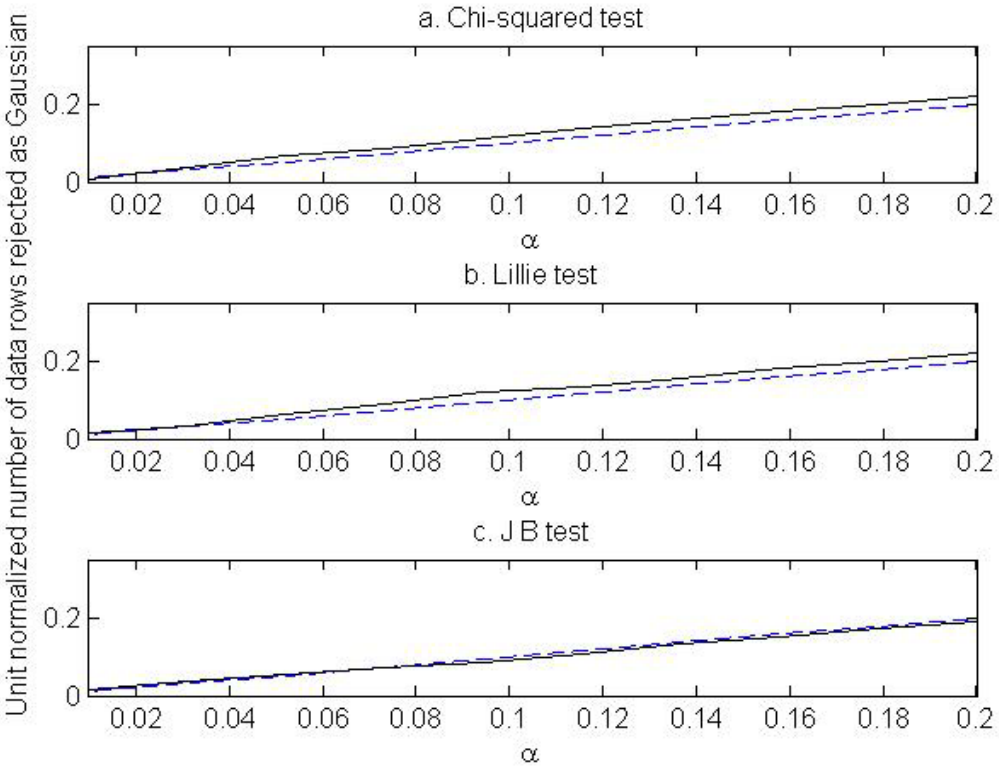

Figure 29 Goodness-of-fit tests using Gaussian distributed random numbers (solid line) and α versus α (dashed line) as a frame of reference.

Next, the goodness-of-fit tests are evaluated for random sequences that follow a central chi-squared distribution (2.30). This type of distribution is selected since it arose in Chapter II. The chi-squared distribution parameter degrees-of-freedom d is varied to evaluate the chi-squared distribution for a number of different shapes. The range evaluated is $d = [1,100]$. Figure 30 is included to provide examples of the potential visual similarity between chi-squared pdfs with degrees of freedom greater than thirty nine and Gaussian pdfs that have been visually fit to the chi-squared distributions. The 'chi-squared' subscripts in Figure 30's legend indicate the degrees-of-freedom parameter for

the chi-squared plots and the 'Norm' subscripts indicate which chi-squared distribution the normal distribution was visually fitted to. The left 'Norm' plots were fitted at the peaks of the chi-squared plots and the right 'Norm' plots were fitted at the tails. Visually, the chi-squared and Gaussian pdfs are similar, especially as d increases.

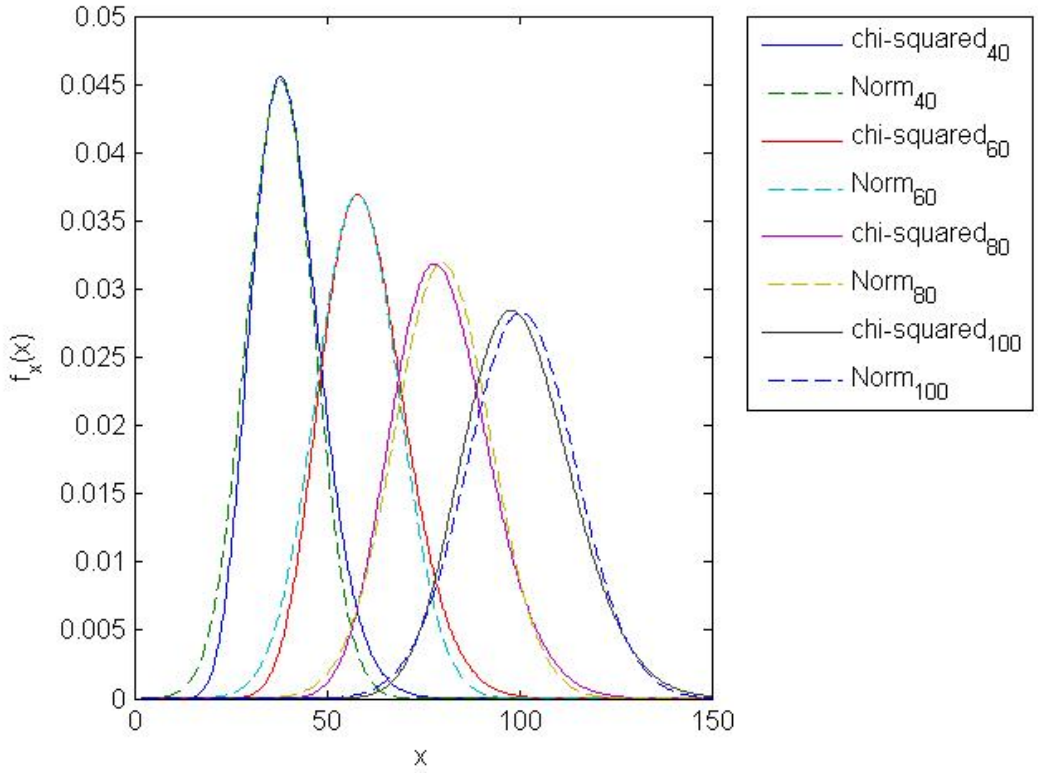

Figure 30 Chi-squared pdfs where the degrees of freedom are indicated by the subscript (solid line) and corresponding Gaussian pdfs (dashed line).

The evaluation of the goodness-of-fit tests using random sequences with a chi-squared distribution where the degree-of-freedom is the subscript (solid lines) and Gaussian distributed random numbers (dashed line) as a frame of reference for the range $d = [40,100]$ by increments of 20 is shown in Figure 31. The visual similarity of the chi-squared pdfs and the Gaussian pdfs shown in Figure 30 indicate that the goodness-of-fit tests restrictively accept the null hypothesis as shown in Figure 31. The goodness-of-fit

tests' performance in Figure 31 shows the capability of the tests to identify the increased similarity between the chi-squared and Gaussian pdf as the chi-squared degrees-of-freedom parameter increases. Of the three goodness-of-fit tests used, the J-B test is the strictest test when chi-squared distributed data is used, as shown by the results in Figure 31.c being closer to unity than Figure 31.a and Figure 31.b.

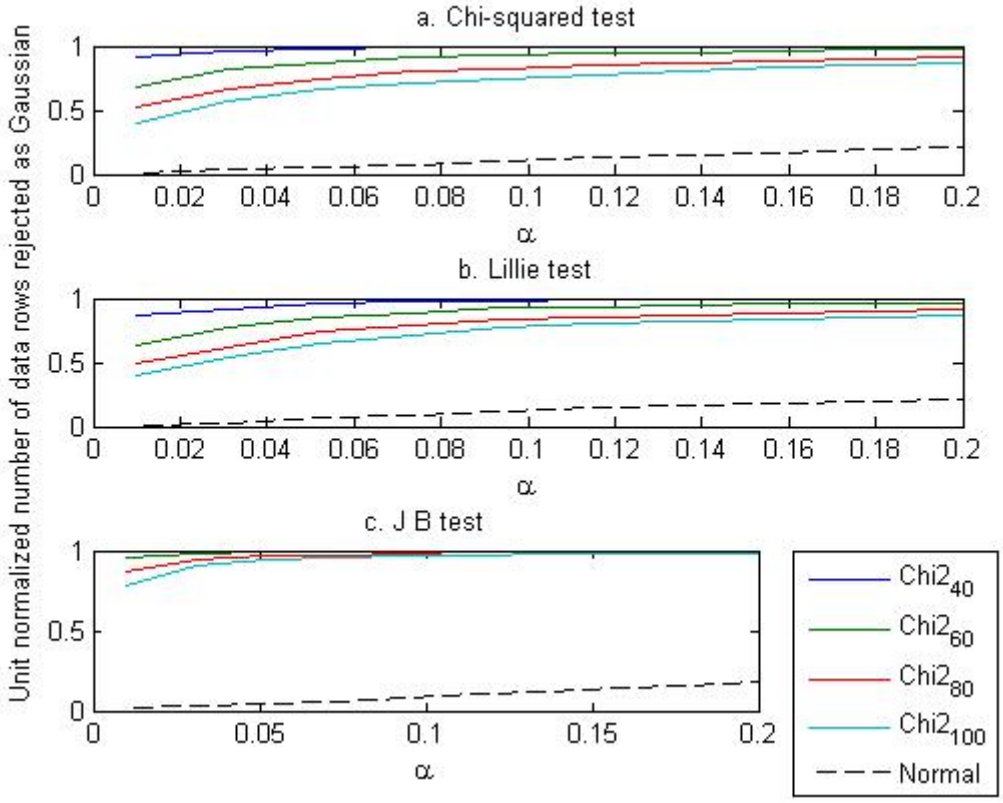

Figure 31 Goodness-of-fit tests using chi-squared distributed random numbers where the degree-of-freedom is the subscript (solid lines) compared with and Gaussian distributed random numbers (dashed line) as a frame of reference.

Four other distributions were chosen to visually evaluate the goodness-of-fit tests. The Gamma and Student T distributions are chosen for their similarities to the Gaussian distribution in some cases [68]. As an aside, the chi-squared and exponential distributions are special cases of the Gamma distribution. The Rayleigh and uniform distributions are

chosen for their dissimilarities to the Gaussian distribution, while at the same time the uniform distribution is symmetric and the Rayleigh distribution is not as unsymmetrical as some other distributions such as the exponential distribution.

The pdf for the Gamma distribution is given by

$$f_x(x)_\Gamma = \begin{cases} \dfrac{\beta^a}{\Gamma(a)} x^{a-1} \exp(-\beta x), & x > 0; a > 0; \beta > 0 \\ 0, & x < 0, \end{cases} \tag{3.11}$$

where a and β are parameters of the distribution and $\Gamma(a)$ is the gamma function [68]. Figure 32 is included to provide examples of the visual similarity between Gamma pdfs with $a \geq 25$ and Gaussian pdfs. For the simulations shown Figure 33, $\beta = 1$ and $a = [25,100]$. Figure 33 shows that the tests are very effective at distinguishing between Gaussian and Gamma distributed data while at the same time being able to recognize the trend of increased pdf similarities for the two data types. Of the three goodness-of-fit tests used, the J-B test is the strictest test when Gamma distributed data is used, as shown by the results in Figure 33.c being closer to unity than Figure 33.a and Figure 33.b.

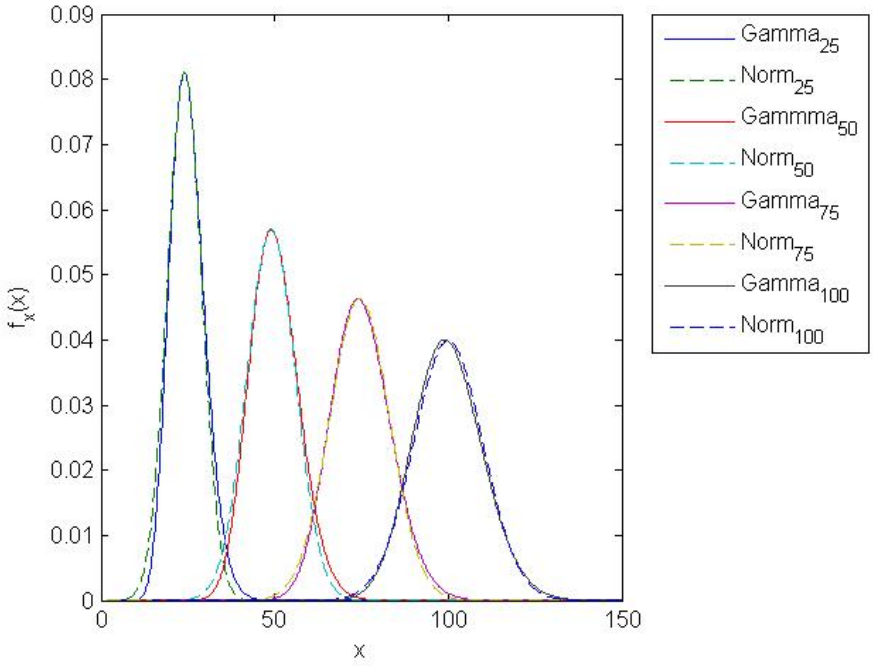

Figure 32 Gamma pdfs where $\beta = 1$ and a is indicated by the subscript (solid line) and corresponding Gaussian pdfs (dashed line).

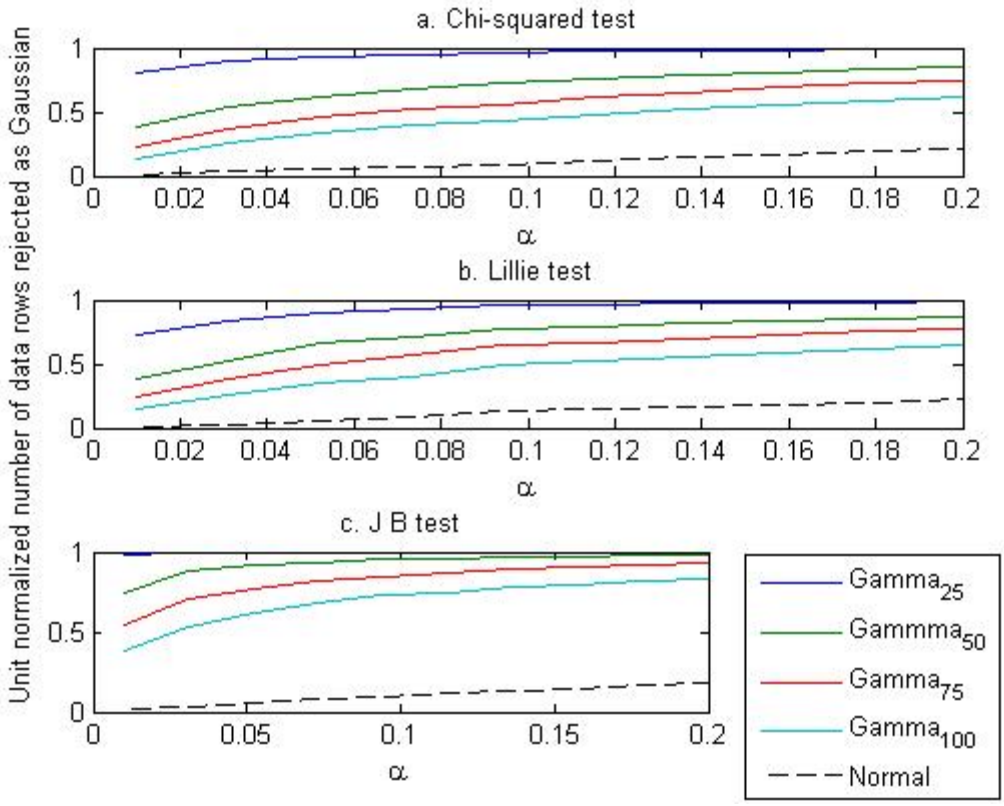

Figure 33 Goodness-of-fit tests using Gamma distributed random numbers where $\beta = 1$ and a is the subscript (solid lines) compared with and Gaussian distributed random numbers (dashed line) as a frame of reference.

The pdf for the Student's t distribution is given by

$$f_x(x)_T = \frac{\Gamma\left(\frac{\nu+1}{2}\right)}{\sqrt{\pi\nu}\,\Gamma(\nu/2)}\left(1+\frac{x^2}{\nu}\right)^{-(\nu+1)/2}, \tag{3.12}$$

where ν is a parameter of the distribution [68]. Figure 34 is included to provide examples of the potential visual similarity between Student's t pdfs with $\nu \geq 4$ and Gaussian pdfs. For the simulations shown in Figure 35, $\nu = [8, 25]$. When $\nu = 1$ and $\nu = 2$, the chi-squared goodness-of-fit test generated a constant output of approximately 0.007 and 0.39, respectively, for the entire range of $\alpha = [0.01, 0.2]$, and MATLAB generated the warning 'After pooling, some bins still have low expected counts. The chi-square approximation may not be accurate.' The MATLAB warning and the dubious

constant results make this type of error easy to identify and disregard. The rest of the results are consistent with the results shown in Figure 35 which shows that the tests are effective at distinguishing between Gaussian and Student's t distributed data while at the same time being able to recognize the similarities of the two data types in certain cases. For example, as ν increases and the Student's t pdf becomes more similar to a Gaussian pdf, the goodness-of-fit tests' results in Figure 35 get closer to the Gaussian distributed random numbers (dashed line) which is used as a frame of reference for distribution trend analysis.

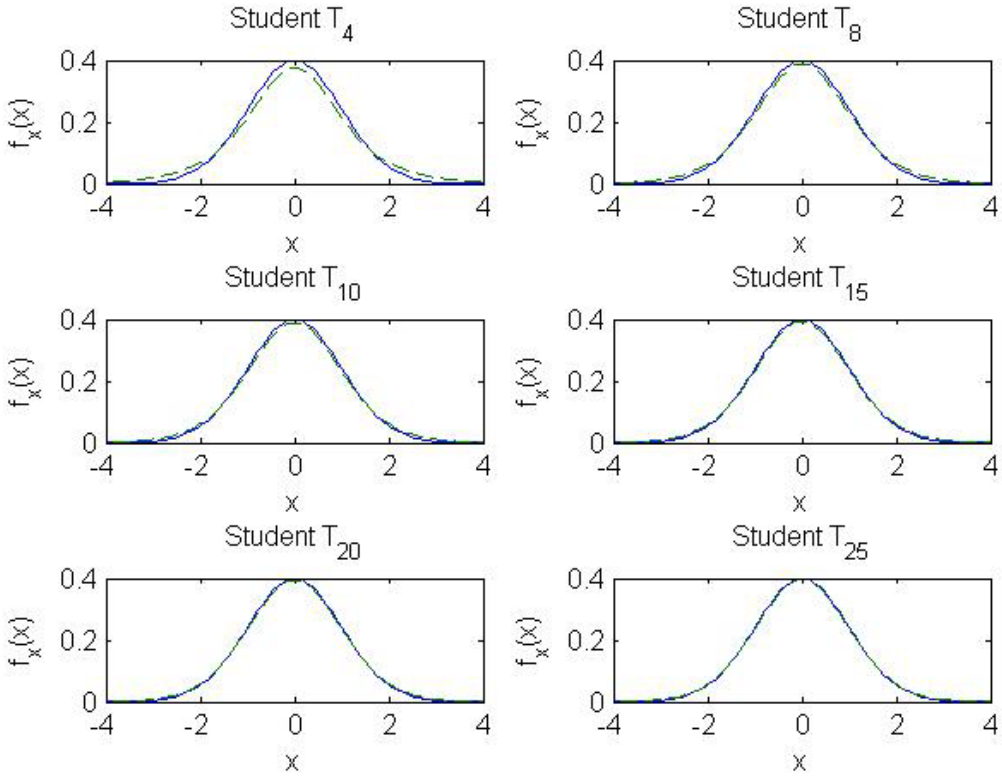

Figure 34 Student's t pdfs where ν is indicated by the subscript (solid line) and corresponding Gaussian pdfs (dashed line).

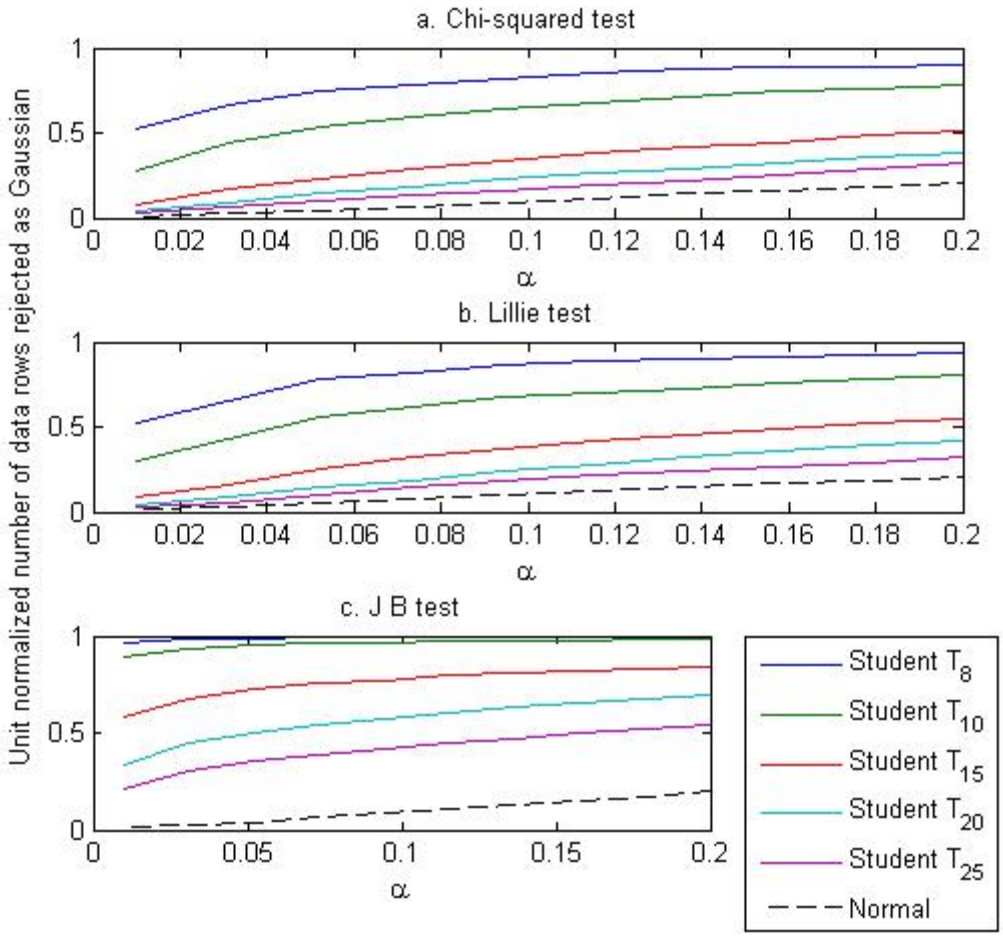

Figure 35 Goodness-of-fit tests using Student's t distributed random sequences where $\nu \geq 4$ is the subscript (solid lines) compared with and Gaussian distributed random sequences (dashed line) as a frame of reference.

The pdf expression for the Rayleigh distribution is given by

$$f_x(x)_R = \begin{cases} 2ax\exp\left(-ax^2\right), & x > 0;\ a > 0 \\ 0, & x \leq 0, \end{cases} \tag{3.13}$$

where a is a parameter of the distribution [68]. Plots of the results are not shown since the goodness-of-fit test simulations rejected the null hypothesis completely over the range $a = \left[10^{-1}, 10^{-7}\right]$ for the random sequences generated with a Rayleigh distribution. The goodness-of-fit test simulations also rejected the null hypothesis completely for random sequences generated with a uniform distribution. This result was expected since Rayleigh and uniform distributions do not remotely resemble a Gaussian distribution.

Now that the goodness-of-fit tests ability to evaluate the trend of increased data to Gaussian pdf similarity for several different distributions, the data from the output of the exponential averaging detector is evaluated using goodness-of-fit tests. The variables considered when evaluating the output of the exponential averaging detector with the goodness-of-fit tests are the NIR, and the weight factor ρ from (2.2) for quotient-combining. The data pdf Gaussian postulate is better supported as ρ increases for the simulations presented, as shown in Figure 36. The results improved slightly with an NIR of 10 dB and degraded slightly with an NIR of -10 dB. The results obtained with an NIR of ± 10 dB does not warrant showing since the change is slight.

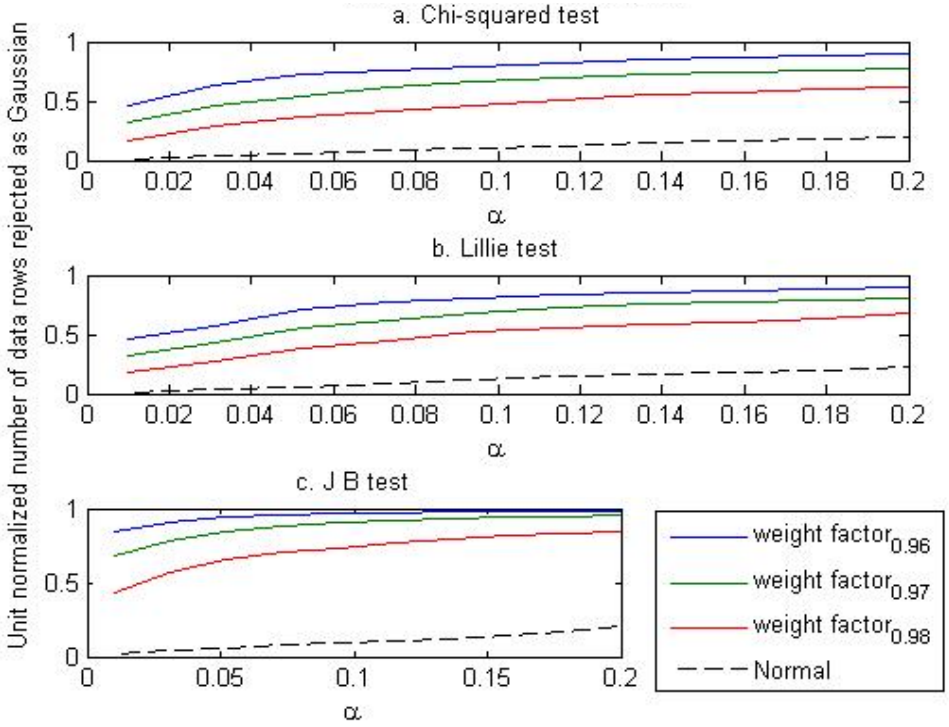

Figure 36 Goodness-of-fit tests using the output from the exponential averaging detector with 0 (dB) NIR, a ρ of 0.96, 0.97, and 0.98, and quotient-combining (solid lines) compared with Gaussian distributed random numbers (dashed line) as a frame of reference

3. Setting the Threshold

The previous subsection substantiates the claim that the output of the exponential averaging detector can be modeled as a Gaussian RV when the scaling factor ρ is sufficiently close to one. To fully define a Gaussian pdf, the mean and variance must be known. The focus of this subsection is to estimate the mean and variance of a Gaussian pdf that can then be used to set a threshold value for the positive frequency bins of the exponential averaging detector's output.

With the exponential averaging detector's output modeled as a Gaussian RV, estimated mean and variance are now determined. The standard deviation (std) is used instead of the variance since it is a common input for determining threshold values with a Gaussian RV. The mean and std of each bin for NIR equaling ten, zero, and negative ten dB are shown in Figure 37, Figure 38, and Figure 39, respectively. The scale for all three plots is the same for comparison purposes. The complexity of the comparison increases as the NIR level decreases since the interference signal's influence is increased. This increased influence is especially significant around the carrier frequency of the BPSK interference signal which corresponds to bin 410 as shown in Figure 38 and Figure 39. This increased influence results in maximum mean values and a local std decrease centered around bin 410. These results are obtained from a single trial which used 1,024 sets of 1,000 data elements each.

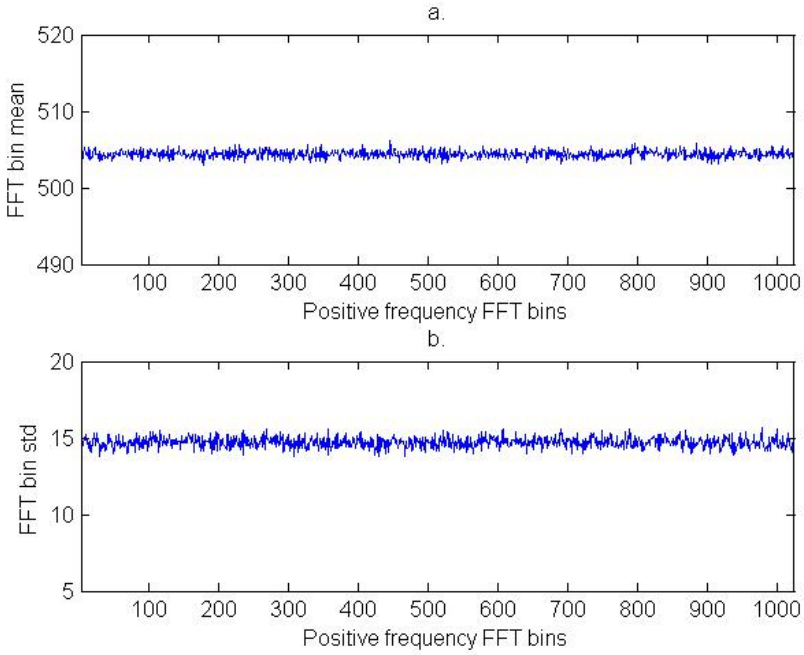

Figure 37 Quotient-combining, NIR=10 dB, ρ =0.99 FFT frequency bin versus FFT bin mean (top) and FFT frequency bin versus FFT bin std (bottom).

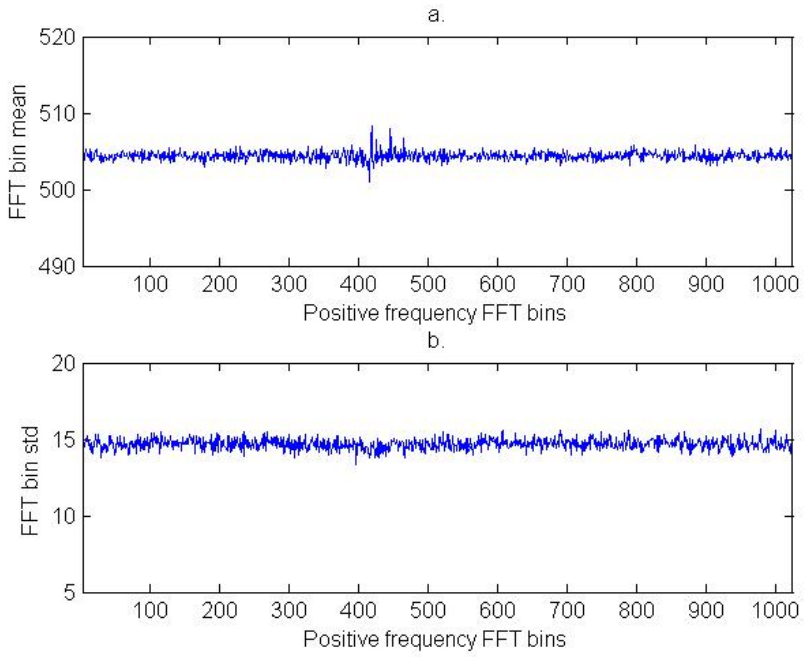

Figure 38 Quotient-combining, NIR=0 dB, ρ =0.99 FFT frequency bin versus FFT bin mean (top) and FFT frequency bin versus FFT bin std (bottom).

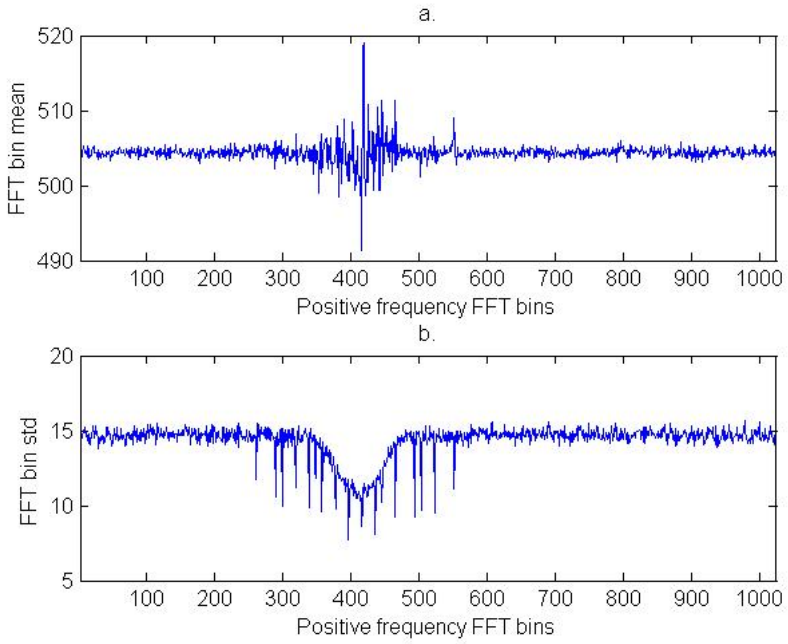

Figure 39 Quotient-combining, NIR= –10 dB, ρ =0.99 FFT frequency bin versus FFT bin mean (top) and FFT frequency bin versus FFT bin std (bottom).

Two methods to evaluate the data shown in Figure 37 to Figure 39 are developed to provide an upper and mid-estimate of P_f. Two estimates are developed so that they can be compared to the simulation based estimate of the P_f and the closer estimate method selected for later work. The mean and std used for the upper-estimate correspond to the bin with the maximum value of $\left(\overline{x}+3\sigma_x\right)$, where $\overline{x}$ is the mean and σ_x is the std for the three data sets shown in Figure 37 to Figure 39, resulting in the upper-estimate $P_{f,u}=1.3\times10^{-3}$. The std estimate is based on the minimum variance unbiased estimator, which uses a normalizing factor of one minus the number of data elements [61, 69].

The method used to obtain the mid-estimate of the probability of false alarm $P_{f,m}$ is to determine the average number of std of separation from the mean to the upper-estimate threshold for all the bins and then use this threshold to determine $P_{f,m}$. The estimate $P_{f,u}$ or $P_{f,m}$ closest to the simulation-based false alarm ratio $P_{\tilde{f}}$ is selected as the probability of false alarm estimate for future work.

Table 3 shows the results from the two methods discussed above. Results are obtained with FFT length equal to 2^{11}, there are 2^{10} positive frequency bins that correspond to frequencies from 0 to 25 MHz, the output from each one of these bins is considered a RV, and the methods described to set mid and upper-estimates of P_f. The std and the mean rows in Table 3 correspond to the bin mean and std values which maximize $\left(\overline{x}+3\sigma_x\right)$. The mid-estimate of P_f is computed using a rounded average number of std of separation from the mean to the upper-estimate threshold for all bins in the three cases presented in Table 3.

Table 3 The extreme threshold values in Figure 37, Figure 38, and Figure 39 and the process of computing them.

NIR (dB)	10	0	–10
std	15.7	14.5	11.4
Separation (# std)	3	3	3
Product	47.1	43.5	34.2
Mean	504.5	508.4	519.1
Bin max. $\left(\overline{x}+3\sigma_x\right)$	551.6	551.9	553.3
γ_u	553.3	553.3	553.3
Threshold mean	548.5	548.5	547.4
Average # std	3.4	3.5	3.8

The probability density function is consistent for noise to interference ratios from 20 dB to -16 dB throughout the spectrum. Before the threshold is applied, the FH signal's effect on the distribution must be understood. The effect of a hop on a frequency bin's distribution varies depending on whether the hop is detected as a minimum or a maximum. If the hop is detected as a maximum, then the mean is positively shifted.

When the hop is detected as a minimum, the mean is negatively shifted. Thus, the threshold must be used at both positive and negative values to ensure that both maxima and minima hops are detected. This doubles the value of P_f.

4. Detector Performance

The simulation results are presented as graphs of the detector's performance for each specific hop. The graphs plot estimated P_d verses SIR for a fixed SNR. Hops are numbered according to their temporal order as indicated in previous figures. Hop number five was not included since its estimated P_d is less than 0.01. The P_d estimates are based on 5,000 simulations, and SNR values are -3 dB, -9 dB, and -15 dB in order to cover the exponential averaging detector's effective range of performance.

The threshold for the simulation is set using the upper-estimate of the probability of false alarm and a std separation of three. The simulation based false alarm error ratio $P_{\tilde{f}}$ is 6.7×10^{-4}. The false alarm ratio is generated using 250,000 simulations where each simulation processed over a million data points. These results indicate that the upper-estimate is conservative since $P_{f,u}$ is larger than $P_{\tilde{f}}$. The mid-estimate computed from the last row of Table 3 is $P_{f,m}=3.6\times10^{-4}$ and underestimates P_f. Thus, the upper estimate is selected as the preferred probability of false alarm estimation method based on the simulation-based false alarm error ratio and the a conservative estimation approach. The consequences of the probability of false alarm upper-estimate selection are that the detector's performance is displayed as detecting at higher SINR for a given estimated P_f and decreased probability that $P_{\tilde{f}}$ is greater than the estimated P_f. In other words, using the upper-estimate gives a more pessimistic result for the SINR required to successfully detect the signal but is a more conservative technique than using the mid-estimate, which gives overly optimistic results.

The general trend that the number of hops that are detectable is reduced as the SIR decreases is illustrated from the simulation results when SNR = -3 dB, as shown in Figure 40. The order at which specific hops are obscured from detection is a combination of the local SIR at the hop frequency, the SNR, and the temporal hop order where the

mid-hops are more obscured, as discussed in Section III.B. In an SIR dominated environment, the temporal hop order and local SIR at the hop frequencies predominantly determine the order at which specific hops are obscured. The frequency hop with the lowest local SIR is hop four with hops one and seven a fraction of a dB higher, hops two, three, and five about 6 dB higher, and hop six approximately 10 dB higher, as shown in Figure 18.

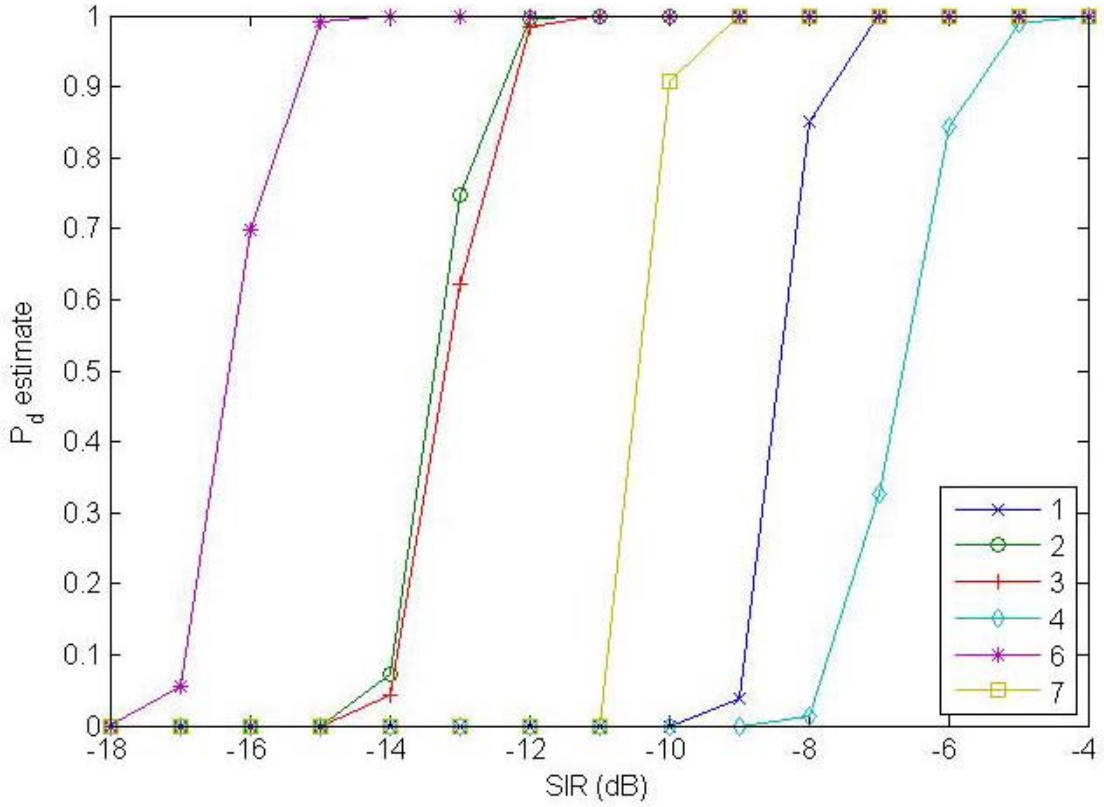

Figure 40 Estimated P_d versus SIR with an SNR = – 3 dB for six of the seven hops as indicated using an exponential averaging FH detector with quotient-combining. Hop number five was excluded due to its low estimated P_d.

Based on the local SIR and temporal order, the first hop expected to be obscured from detection is hop four; however, as discussed in Section III.B, hop five is obscured from detection. Thus, the temporal order of hops obscured is shifted to more recent temporal mid-hops. Hop four is the next hop to be obscured from detection, followed by

hops one and seven as a result of the local SIR. The more recent end-hop, hop seven, has a one dB performance advantage over the earlier end-hop, hop one, showing the emphasis of the *recent* end-hop. At low SIR relative to the SNR, the detector's performance with hops two and three is dominated by the SIR as compared to the one dB performance difference shown by the hop order influence with hops one and two. Note that the relative performance between hop four and hops two and three is approximately 6 dB, which corresponds to the local SIR difference between the hops. Figure 40 shows that the last hop to be obscured from detection is hop six, which is obscured 9 dB down compared to hop four and closely corresponds to hop six being 10 dB up from hop four with respect to the local SIR. The abrupt change in the estimated probability of detection for specific hops is indicative of a jamming environment or, equivalently, an environment where the influence of SIR versus SNR dominates the detector's performance. Finally, no relation is observed between the estimated probability of detection for a specific hop and the hop's proximity to a CW signal when SNR= -3 dB.

Simulation results obtained for SNR= -9 dB further support the general observation that the number of detectable hops is reduced as SIR decreases, as shown in Figure 41. The increased influence of SNR on the detector's performance is shown by the less abrupt change of the estimated probability of detection for hops two, three, four, and six in Figure 41. The detector's better performance with end-hops versus mid-hops as the significance of SNR increases over SIR is also illustrated by performance differences between hops two and three as shown in Figure 40 and Figure 41. In addition the minimum influence of SNR on the detection of hops one and seven is shown by the similar abrupt change in the estimated probability of detection. These observations indicate that the relation between the hop order and the detector's performance increases as SNR increases as relative to SIR. Finally, the results shown in Figure 40 indicate no specific relationship between the estimated probability of detection for a specific hop and the hop's proximity to a CW signal seems to exist when SNR= -9 dB.

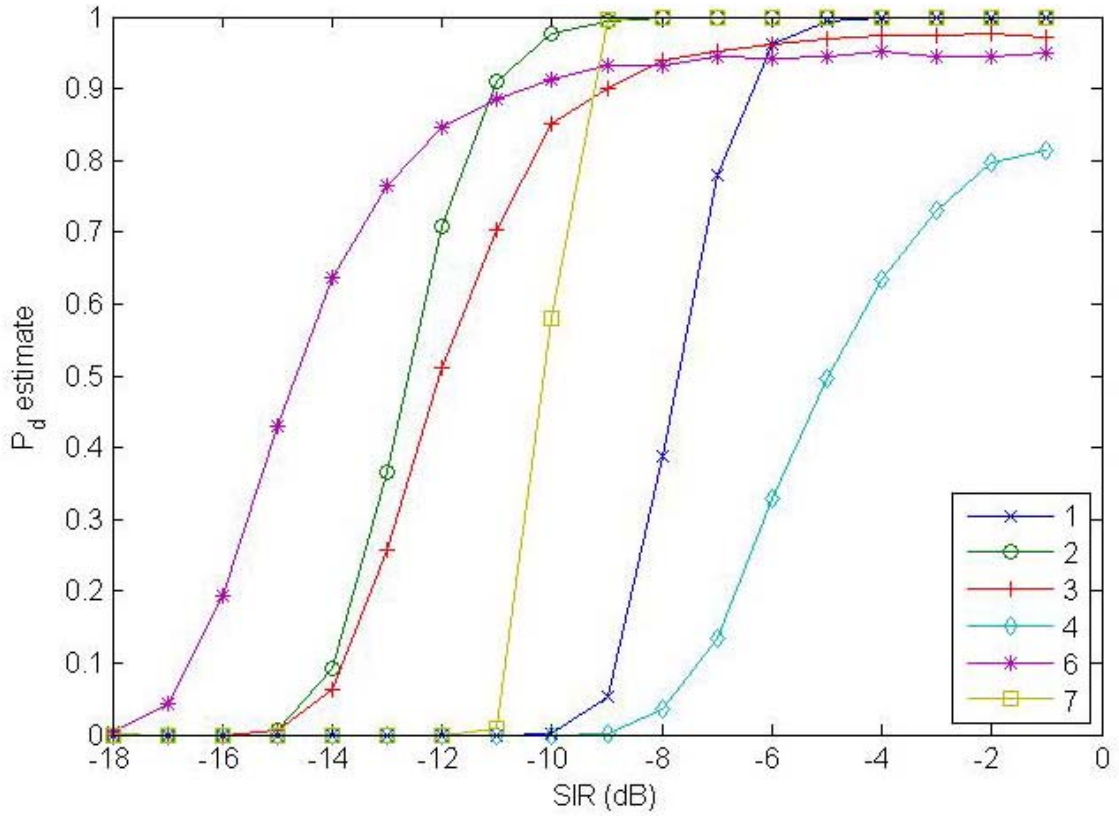

Figure 41 Estimated P_d versus SIR with an SNR = -9 dB for six of the seven hops as indicated using an exponential averaging FH detector with quotient-combining. Hop number five was excluded due to its low estimated P_d.

Figure 42 presents results obtained for SNR= -15 dB. The following comments can be made: the number of detectable hops are reduced as SIR decreases, the gradual change in the estimated probability of detection for all hops is due to the dominant influence of SNR versus SIR with respect to the detector's performance, and the detector exhibits better performance with end-hops one, two, and seven as compared to mid-hops three and six which illustrates the relationship between the end-hop versus mid-hop performance as SNR increases relative to SIR. Finally, the performance results when SIR dominates provide a limiting performance measure for decreased SNR illustrated in Figure 41 and Figure 42.

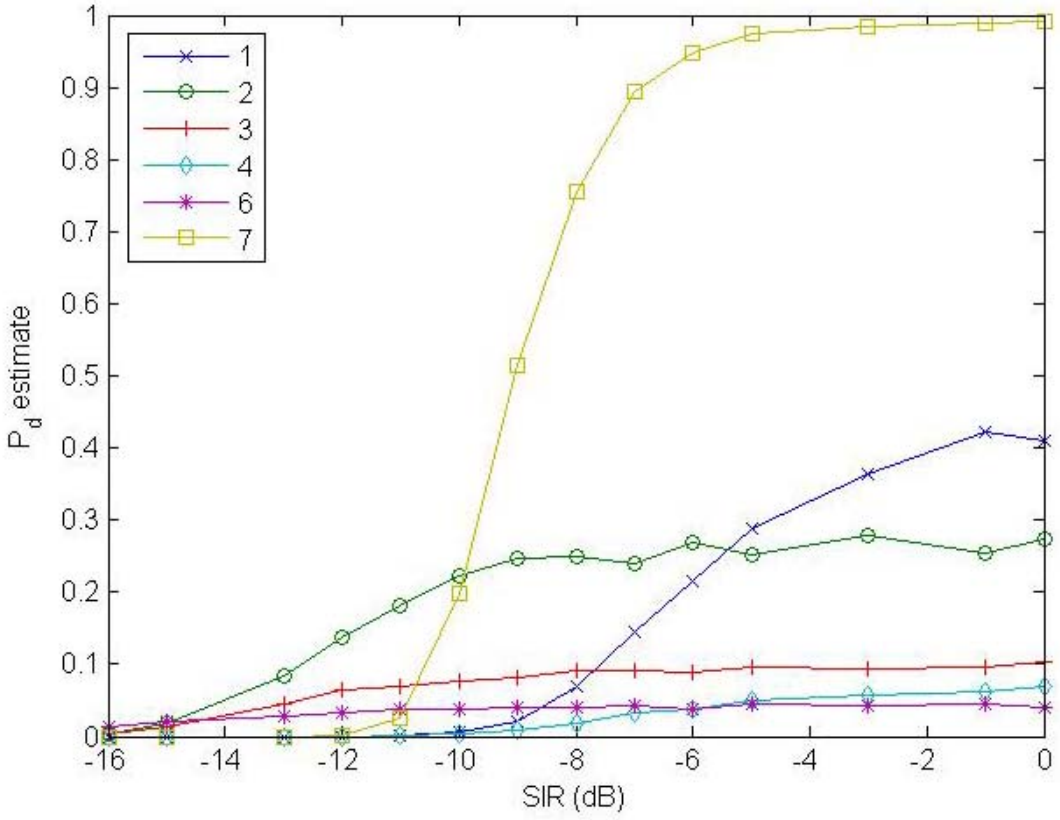

Figure 42 Estimated P_d versus SIR with an SNR = -15 dB for six of the seven hops as indicated using an exponential averaging FH detector with quotient-combining. Hop number five was excluded due to its low estimated P_d.

Figure 43 compares the detector's performance when the threshold γ is set to 3.5 stds (dashed line) and 3 stds (solid line) above the mean, corresponding to probabilities of false alarm upper-estimates of $P_{f,u} = 4.6 \times 10^{-4}$ and $P_{f,u} = 2.6 \times 10^{-3}$, respectively. Results show the loss of performance is approximately 0.5 dB for the decreased probability of false alarm. The simulation-based false alarm error ratio $P_{\hat{f}}$ is 2.12×10^{-4}, which further supports the use of the probability of false alarm upper-estimate.

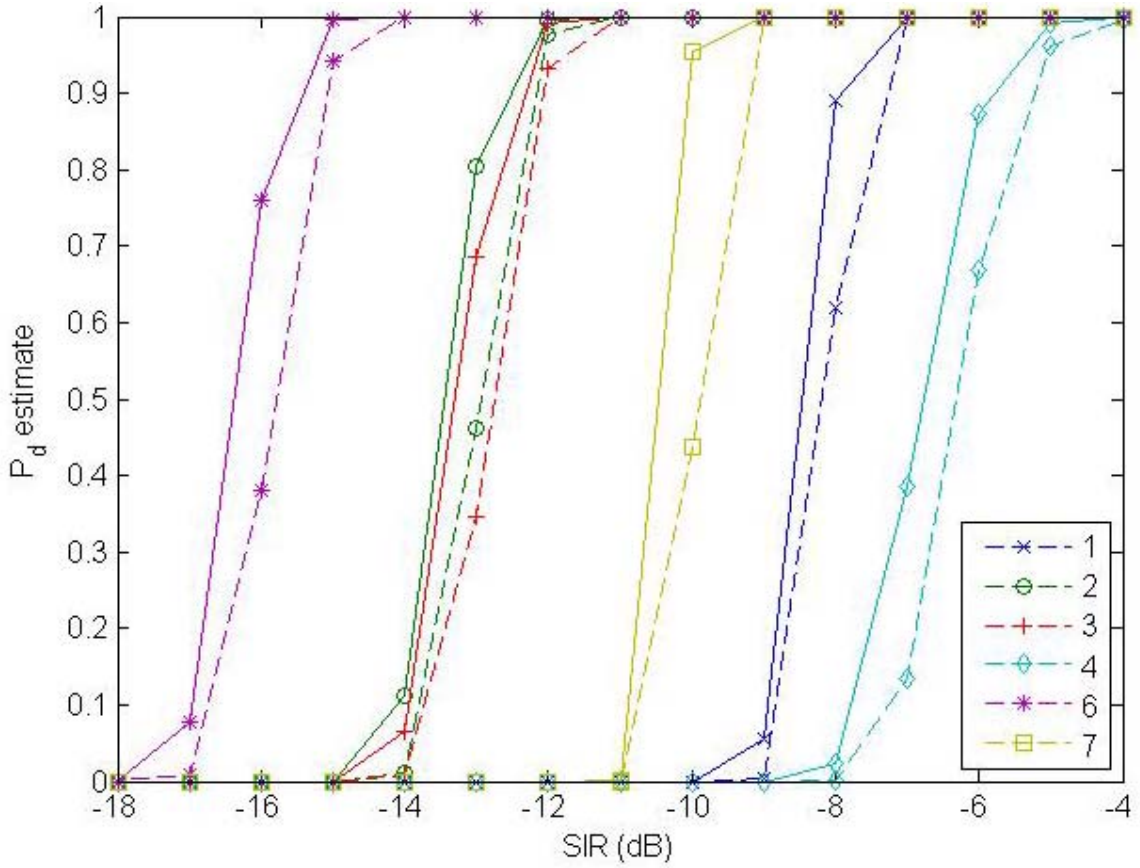

Figure 43 Estimated P_d versus SIR with an SNR = -3 dB with γ set at 3.5 stds (dashed line) and 3 stds (solid line) above the mean for six of the seven hops as indicated using an exponential averaging FH detector with quotient-combining. Hop number five was excluded due to its low estimated P_d.

The simulation set-up, decision criteria development, and the simulation results were presented in this chapter. The simulation set-up included a description of the various parameters and signals used. The decision criteria discussed three methods to heuristically estimate a pdf to model the RV representing the detector's output; histograms, probability plots, and goodness-of-fit tests. Findings heuristically support the postulate that the RV that models the detector's output can be modeled as Gaussian. From the postulated pdf, the detector's threshold was set, and upper and mid-estimates for the probability of false alarm were developed.

IV. ACRE THEORY

An intermediate step between the detection and interception of signals is the estimation of signal characteristics. One of the primary signal characteristics of DS-SS signals is the chip rate R_c. This chapter and the next investigate the performance of an ad-hoc non-linear chip rate estimator for DS-SS pulse-shaped, PSK signals.

A common method of chip rate detection is the CRD discussed in Chapter I and shown in Figure 3. The theoretical and laboratory performance of a CRD is well documented for rectangular pulse shapes [1, 11]. The a-priori signal knowledge that the CRD requires to operate is discussed in this chapter along with a simple analysis of the degradation of the CRD performance due to half-sine shaped pulses versus rectangular pulses. The CRD requires an a-priori estimation of the chip rate. Thus, as the name implies, the primary purpose of the CRD is to detect the chip rate and not to estimate it. From this discussion of the CRD, a digital ad-hoc chip rate estimator (ACRE) is developed and described. Similarities and differences between the CRD and the ACRE are presented later in the chapter.

A. CRD PERFORMANCE WITH HALF-SINE PULSE SHAPING

The CRD performance is degraded when the signal uses pulse shaping. The degradation resulting from using a half-sine shaped pulse over a rectangular pulse is briefly considered. The deterministic pulse-trains generated by the half-chip-delay-and-multiply for both a rectangular pulse and a half-sine pulse are shown in Figure 44. The signal generated from the delay-and-multiply of the half-sine shaped pulse is a half-sine at twice the frequency and half the amplitude, as shown in the center plot of Figure 44.

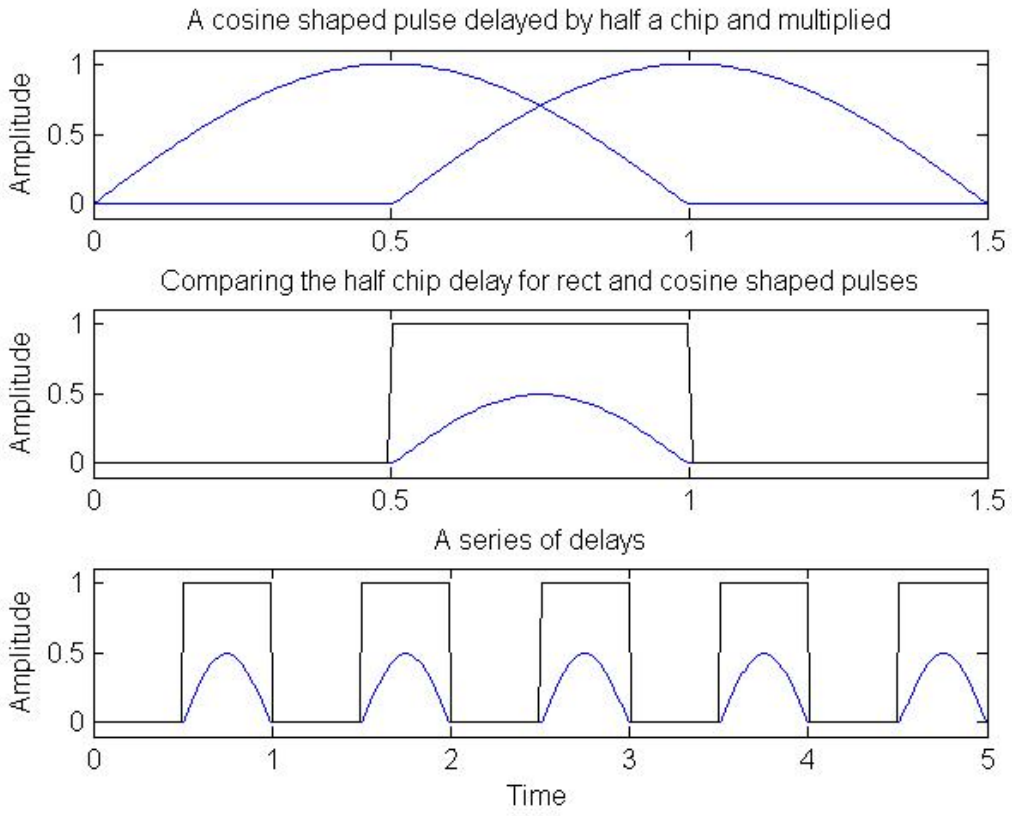

Figure 44 Half chip delay and multiply results for a half-sine shaped pulse and a rectangular pulse.

From (1.13), the power in the R_c rate-line for a half-sine shaped pulse is computed using the exponential Fourier series coefficient c_{R_c} that corresponds to the R_c frequency, where c_{R_c} is defined as

$$c_{R_c} = \frac{2}{T_c}\int_0^{T_c}\left\{\sin(\pi R_c t)\sin(\pi R_c(t-D))\,\mathrm{rect}\left[\frac{t-0.5(T_c-D)}{T_c-D}\right]\right\}\exp(-j2\pi R_c t)\,dt. \quad (4.1)$$

Following the approach used for rectangular pulses, we evaluate the integral in (4.1) by expanding the product of the sine terms which leads to

$$c_{R_c} = \frac{1}{T_c}\int_0^{T_c-D}\left\{\cos(\pi R_c D) - \cos\left[\pi R_c(2t-D)\right]\right\}\exp(-j2\pi R_c t)\,dt. \quad (4.2)$$

Next, integrating the top term in $[\cdot]$ in (4.2) and expressing the exponential as trigonometric functions using Euler's formula (4.2), we get

$$c_{R_c} = \frac{1}{T_c}\left\{\frac{\cos(\pi R_c D)}{-j2\pi R_c}\left\{\exp\left[-j2\pi R_c\left(T_c - D\right)\right]-1\right\}- \int_0^{T_c-D}\cos\left(\pi R_c(2t-D)\right)\left[\cos\left(2\pi R_c t\right)- j\sin\left(2\pi R_c t\right)\right]dt\right\}. \tag{4.3}$$

Finally we evaluate the integral in (4.3) by expanding the product of the trigonometric functions as the sum of trigonometric functions which leads to

$$\begin{aligned} c_{R_c} = \frac{1}{T_c}\Bigg\{&\frac{1}{\pi R_c}\cos(\pi R_c D)\sin\left[\pi R_c\left(T_c - D\right)\right]\exp\left[-j\pi R_c\left(T_c - D\right)\right]- \\ &\frac{\left(T_c - D\right)}{2}\cos(\pi R_c D)+\frac{1}{8\pi R_c}\sin\left[\pi R_c\left(4T_c - 5D\right)\right]+\frac{1}{8\pi R_c}\sin(\pi R_c D)+ \\ &\frac{j}{8\pi R_c}\cos(\pi R_c D)-\frac{j}{8\pi R_c}\cos\left[\pi R_c\left(4T_c - 5D\right)\right]-\frac{\left(T_c - D\right)}{2}\sin(\pi R_c D)\Bigg\}. \end{aligned} \tag{4.4}$$

The magnitude of (4.4) does not reduce to a compact expression as in (1.18) for rectangular pulses, so (4.4) is evaluated numerically, and results shown in Figure 45. The equation is evaluated in MATLAB and the results checked by numerically integrating with MathCAD. The normalized power in the R_c rate-line for a half-sine shaped pulse as a function of *D* with half-sine pulse shaping is much different than the rectangular pulse as shown in Figure 45 and Figure 5, respectively. Results show that the maximum R_c rate-line power is located at a delay of zero (i.e., a squaring circuit versus a delay-and-multiply). From this observation, it is clear that the nonlinear operation of a delay-and-multiply for half-sine shaped pulses is sub-optimum.

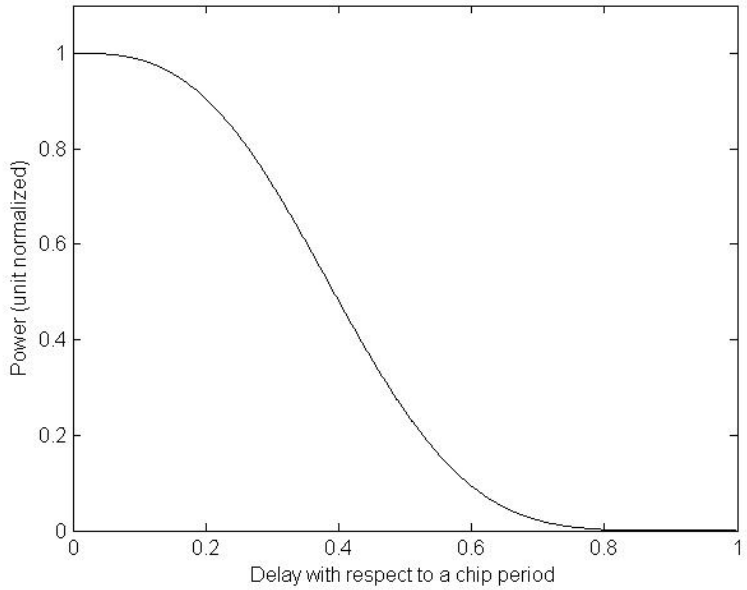

Figure 45 Normalized power in the CRD R_c rate-line as a function of delay with respect to the chip period for a half-sine pulse.

B. AD-HOC CHIP RATE ESTIMATOR (ACRE) DESCRIPTION

1. Overview of ACRE through the PSD Estimator

The ACRE is constructed from the basic structure of the CRD. The block diagram of the ACRE is shown in Figure 46. The DS-SS signal is first down converted to baseband. The down-converted signal is represented in complex baseband form. Analogous to the CRD, f_c is either known or estimated using the procedure discussed in Chapter I. The I and Q channels are converted from analog to digital waveforms. Since the signals of interest are phase-shift keyed signals, with their data in the phase component, the signal phase is generated using $\theta(k) = \arctan\left\{\mathrm{Im}\left[r(k)\right]/\mathrm{Re}\left[r(k)\right]\right\}$ with a four quadrant arctan where $r(k)$ is the input into the phase detector and *k* is a digital time reference. This transformation is the first of three non-linear transforms used in the ACRE scheme.

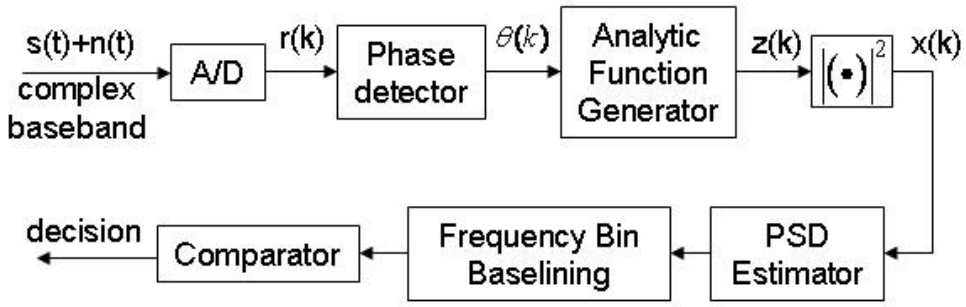

Figure 46 Block diagram of ACRE.

Following the phase detector, a Hilbert transform-based envelope detector is then used. The idea of using the Hilbert transform in this work loosely originated from its application in AM single-side-band demodulation and the instantaneous phase changes observed in a DS-SS signal. The Hilbert transform generates $z(k)$ as discussed in Chapter I. The analytic representation of $\theta(k)$ is $z(k)$, as shown in Figure 47 and illustrated in Figure 7. The second non-linear process in the ACRE squares the I and Q components of the analytic function $z(k)$ to produce the envelope squared. Note, that the square root of the squared envelope could be taken to produce the envelope, but was deemed unnecessary since only the relative difference between the noise and the signal is desired.

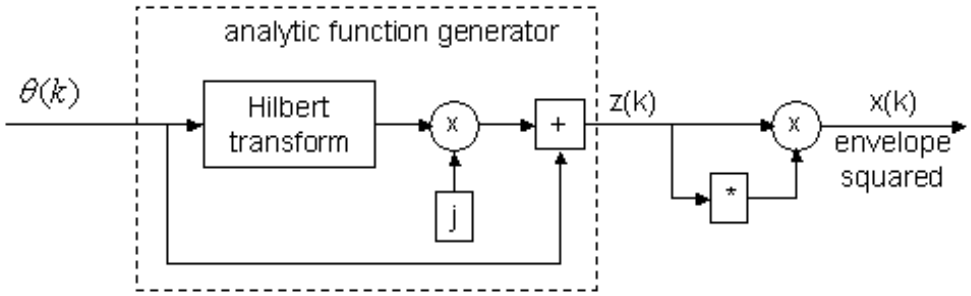

Figure 47 Envelope squared generator.

The PSD of the envelope detector's output is estimated next. The PSD estimator block in ACRE is loosely analogous to the non-linearity and the spectral component

blocks in the CRD. The first step in drawing this analogy is to view the PSD estimate process as two separate parts, first the discrete estimation of the autocorrelation, and second the Fourier transform of the autocorrelation. The PSD estimate may be computed using the biased form of the sampled autocorrelation $\widehat{R}_x[l]$:

$$\widehat{R}_x[l] = \frac{1}{N_s} \sum_{n=0}^{N_s-1-l} x[n+l]x^*[n]; 0 \le l < N_s, \tag{4.5}$$

where N_s is the total number of samples and ( )* is the complex conjugate operation.

The estimated PSD $\widehat{S}_x(e^{j\omega})$, also known as the correlogram is obtained by computing the discrete time Fourier transform of (4.5) as

$$\widehat{S}_x(e^{j\omega}) = \sum_{l=-L}^{L} \widehat{R}_x[l]e^{-j\omega l}; L < N_s, \tag{4.6}$$

where L is usually one-tenth N_s [70]. The autocorrelation operation is the third and final non-linearity in the ACRE process. The transform step in (4.6) is digitally analogous to the analog spectral component in the CRD. The step of multiplying $e^{-j\omega l}$ in the summation in (4.6) is analogous to the offset frequency generator block in the CRD diagram. When the PSD estimator block is viewed this way, it is clear that the chip rate is automatically searched for in the ACRE scheme, whereas the CRD scans for the chip rate. Obviously, a disadvantage of this process is its increased complexity. In addition the ACRE scheme does not automatically take advantage of the chip rate knowledge, when it is available. Thus, other methods of chip rate detection may be better suited when the chip rate is known prior to detection. As a related aside, intermediate filtering can be included when the potential frequency range of the chip rate is narrowed, as this operation will result in increased SNR and subsequently improves the detector's performance.

The summation in (4.6) is digitally analogous to the analog integration of the CRD spectral component. Although the two previous analogies were direct, the indices of summation and the limits of integration are indirectly analogous. The reason for the last analogy being referred to as indirect is that the discrete autocorrelation's maximum is less than the number of samples, and the PSD's maximum summation index is also less than

the number of samples without zero padding. Depending on the method used to estimate the PSD, the summation may have more than an order of magnitude fewer elements than the number of samples when the PSD estimated is computed discretely [70].

To further illustrate the 'indirect' analogy, the spectral resolution of the integrator is the inverse of the integration time, whereas the spectral resolution is determined by the sampling frequency and the number of angular frequencies used in the discrete PSD estimate. The output of each bin of the PSD estimate is analogous to the output voltage *V* of the CRD. Thus, the PSD estimate acts as a filter bank which illustrates how ACRE scans for, detects, and estimates the chip rate simultaneously.

From this simple analysis it is seen that the transform within the ACRE PSD estimator block has analogous properties to the spectral component block of the CRD. Although the correlogram PSD estimation method is useful to illustrate the motivation behind using a PSD estimator, other PSD estimation methods are more effective with respect to data required and frequency resolution [70]. The PSD estimate used in the ACRE simulations is the periodogram $\widehat{P}_x(e^{j\omega})$ defined as

$$\widehat{P}_x(e^{j\omega}) = \frac{1}{N_s}\left|X(e^{j\omega})\right|^2, \tag{4.7}$$

using Welsh windowing where N_s is the total number of samples and $X(e^{j\omega})$ is the Fourier transform of the input signal [70].

2. ACRE Frequency Bin Baselining

A specific rate-line R_c is detected in the CRD scheme. In the ACRE scheme a frequency range is scanned, and R_c is detected and estimated simultaneously. These simultaneous scan, detect, and estimation operations require multiple frequency bins outputs to be evaluated. Unlike the CRD integration output, the PSD estimator output in a specific bin is highly dependent on the PSD of the DS-SS signal, and there are a large range of PSD estimator output values when comparing a low frequency bin to a high frequency bin. This range of values within a bin is primarily attributed to bins located at the PSD's nulls. The larger range of values between low frequency and high frequency bins is attributed to the general downward trend of the PSD. Thus, ACRE deviates from

the CRD in that the outputs from the various bins are locally averaged. This operation is done so that the most likely rate-line estimate, denoted as R_{ce}, can be selected from the frequency bins. The frequency bin baselining allows a comparison of bins across the frequency search range so that R_{ce} can be evaluated. The evaluation is a relative evaluation (i.e., R_{ce} is 3 dB greater than the second most likely estimate). The idea of baselining is illustrated in Figure 48, where the response in red at 1 MHz is distinct but is not the maximum value. The blue line is the smoothed data that is used to baseline the response in red so that the maximum value selection criteria can be used.

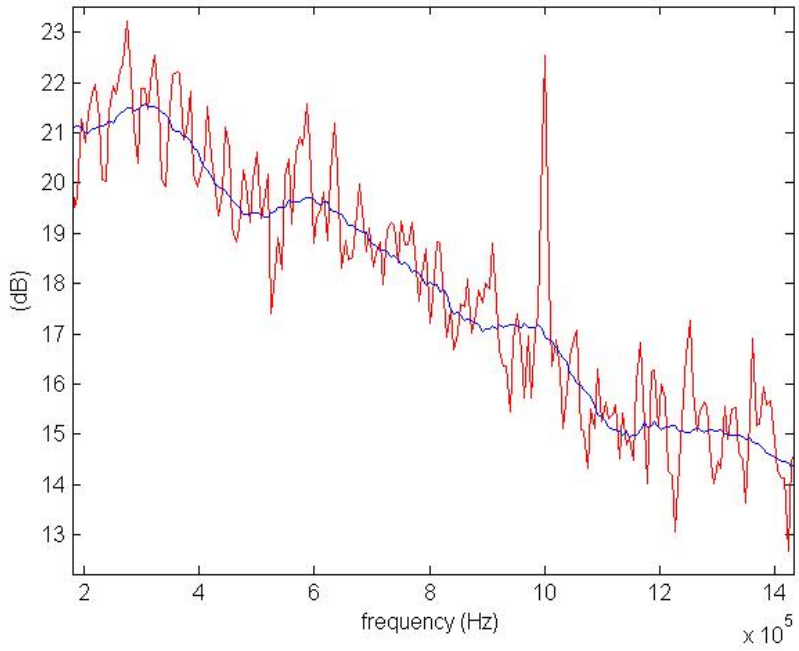

Figure 48 An illustration showing the motivation for baselining a signal so that it can be compared throughout its entire frequency range.

Three approaches to baselining the frequency bins are considered next. The first approach uses the theoretical ACRE PSD estimate, from which simulation results can be baselined. Unfortunately, the theoretical ACRE PSD is mathematically intractable. A second approach estimates the ACRE PSD with a long sample of AWGN only as input to

baseline the signal. However, this approach does not account for changes in the channel and is computationally intensive. A third possible approach uses LPF data as the baseline.

The LPF baseline implementation uses the fact that frequency bin outputs can be compared to each other when each output is baselined by a local average of the frequency bins near it. A local average operation is obtained by summing a number of elements near the frequency bin of interest. Note that dividing the results by the number of summed elements is not necessary when the same number of elements is used for all averages. The process of discrete summing is equivalent to analog integration, while integration can be viewed as a type of LPF. This thought process led to the use of a LPF in baselining the data.

The LPF data is then combined with the non-filtered data by subtraction in the bottom branch and by division in the top branch of the baseliner, as shown in Figure 49. The two methods of baselining and the LPF used were obtained experimentally. The same LPF is used in both LPF blocks and is a linear phase FIR filter of order 50 with a cutoff frequency of 100 kHz, a sampling frequency of 50 MHz, passband ripple of one-half a dB, a stopband ripple five dB, passband desired amplitude of unity, a stop band desired magnitude of zero and was generated using a Parks-McClellan based algorithm in MATLAB.

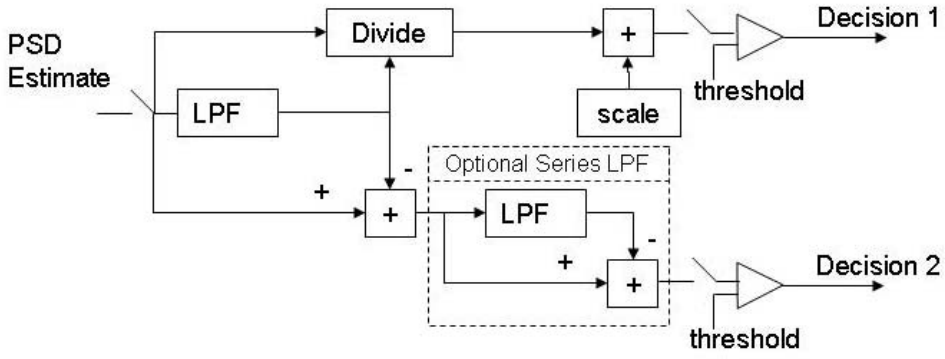

Figure 49 Frequency bin baselining and comparators.

The idea of applying filters in series loosely came from the series filter setup in wavelet schemes. The LPFs in a series configuration versus a single LPF of twice the order experimentally provided smoother results with lower computations in the initial evaluations of a small sample set of experiments and further analysis of this phenomenon is not presented in this work. Simulations showed that decision 1 and 2 configurations generate similar initial results. The top branch leading to decision 1 is referred to as the *division baseline method* and the bottom branch leading to decision 2 is referred to as the *summing baseline method*.

The probability density function (pdf) of the RV that models the signal at the input of the comparator is estimated using simulations. This step is necessary as the thresholding method used in the CRD scheme is not theoretically shown to be applicable, and a theoretical solution for the PSD estimator output RV pdf is mathematically intractable. From the estimated pdf, a threshold is generated using (1.6) and a selected P_f value, and a simulation-based estimate of the probability of detection is generated.

This chapter introduced the concept of the ACRE scheme, and compared it to the CRD approach. The performance of the CRD with half-sine pulse shaping was investigated using Fourier series coefficients. Two baseline methods used to compare the different frequency bin outputs of ACRE were presented.

V. ACRE SIMULATION METHODS AND RESULTS

The simulation set-up, decision criteria development, and the simulation results are presented in this chapter. Various parameters and signals which are used to evaluate ACRE's performance are described in the simulation set-up. The functional relationship between the decision criteria and the time bandwidth product (TBW) is discussed. Some subjective comparisons are made between CRD and ACRE performances. Finally, a summing baseline method is selected, three variations on the ACRE detector are discussed and their performances presented.

A. SIMULATION SET-UP

Simulations are performed using MATLAB. The noise is generated with an intrinsic function in MATLAB. The signal used is a QPSK signal with half-sine pulse shaping. The evaluation represented is in terms of SNR level. Note that the SNR parameter must be converted to energy per chip-to-noise power spectral density E_c/N_o to compare the results for the CRD in [11], which leads to:

$$SNR = \frac{E_c/T_c}{N_0 BW} = \frac{E_c}{N_0}\frac{R_c}{BW}, \tag{5.1}$$

where BW is the bandwidth.

The duration of the data processed is labeled and is generally between 1 and 32 ms. The bin bandwidths used to evaluate ACRE are approximately 6 kHz and 24 kHz. Based on the bin bandwidths used, the maximum resolution of R_c using ACRE is approximately 3 kHz regardless of the duration of the data processed, when the estimate of the chip-rate is selected as the mid-frequency of the chosen bin. The number of bins is increased or the frequency range is decreased to improve the resolution of R_c. The expected range of R_c varies between 0.5 to 25 MHz. The assumed R_c search range requires that the sampling frequency f_s be equal to or greater than 50 MHz by the Nyquist theorem. The FIR realization of the Hilbert transform reduces the low end of the

R_c frequency search range from zero to 500 kHz and is a potential source of error. The direct connection input to the output summer from Figure 6 zero pads the front and back of the data with one half the Hilbert filter order.

LPFs used to provide frequency bin baselining reduce the lower end of the R_c search range if the LPF cutoff frequency is within the R_c search range. Experimental results show that R_c is not detected when $R_c < 0.002 f_s$, the detection of R_c is not affected by the frequency bin baselining when $R_c > 0.05 f_s$, values of R_c between these ranges are progressively less affected as R_c increases. The frequency bin baselining in the following simulations do not limit the search range of R_c.

B. DECISION CRITERIA

The approach used in this chapter to support the postulate that the ACRE output can be modeled as a Gaussian RV is similar to that described in Chapter III. One difference in the approach used in this chapter is that the TBW is the primary limiting factor with respect to whether ACRE's output can be modeled as a Gaussian RV as compared to the weight factor being the primary limiting factor for the exponential averaging detector. The TBW metric is selected since it is used in other detectors to determine whether or not the central limit theorem can be applied to the output of those detectors to assume that the detector output can be modeled as a Gaussian RV [3, 23, 29].

The ACRE output data used for the initial comparison with Gaussian distributed data has a $TBW \approx 6$ when the number of frequency bins is 2^{13}, covering frequencies -25 to 25 MHz, and the duration of the data sets is one ms with a sampling frequency of 50 MHz. The $TBW \approx 6$ value is selected since it is the lowest value of TBW considered. Figure 50 through Figure 53 illustrate the visual similarities between the output of ACRE and Gaussian data for the summing and division baselining methods discussed in Subsection IV.B.2, using both histograms fit with a Gaussian estimate and qq plots. The output data is postulated as Gaussian since the results in Figure 50 through Figure 53 support that postulate.

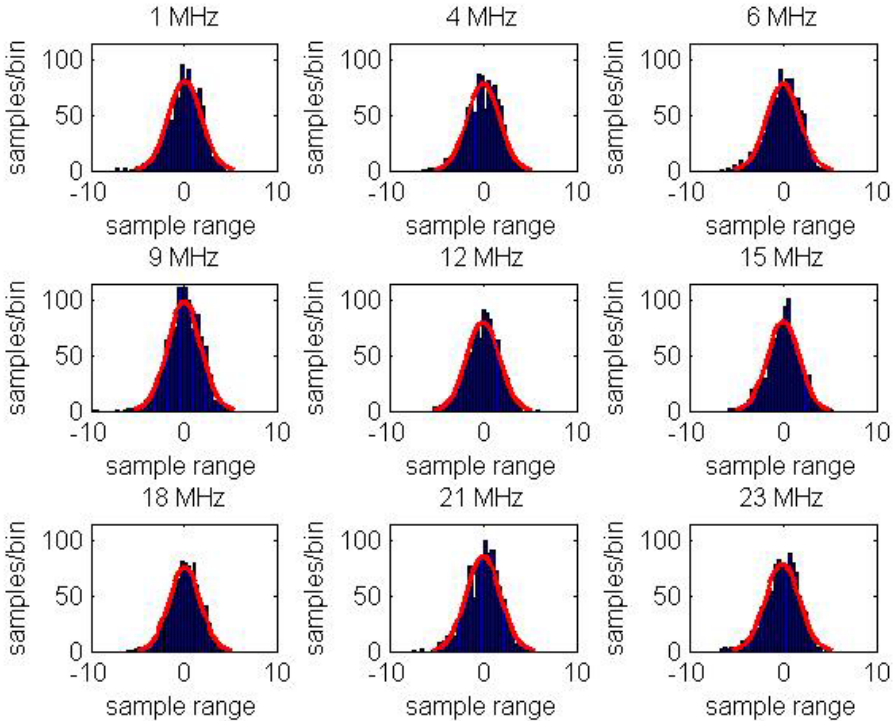

Figure 50 Gaussian estimate (line) and histogram of nine frequency bins from the output of the ACRE with the summing baseline method and $TBW \approx 6$.

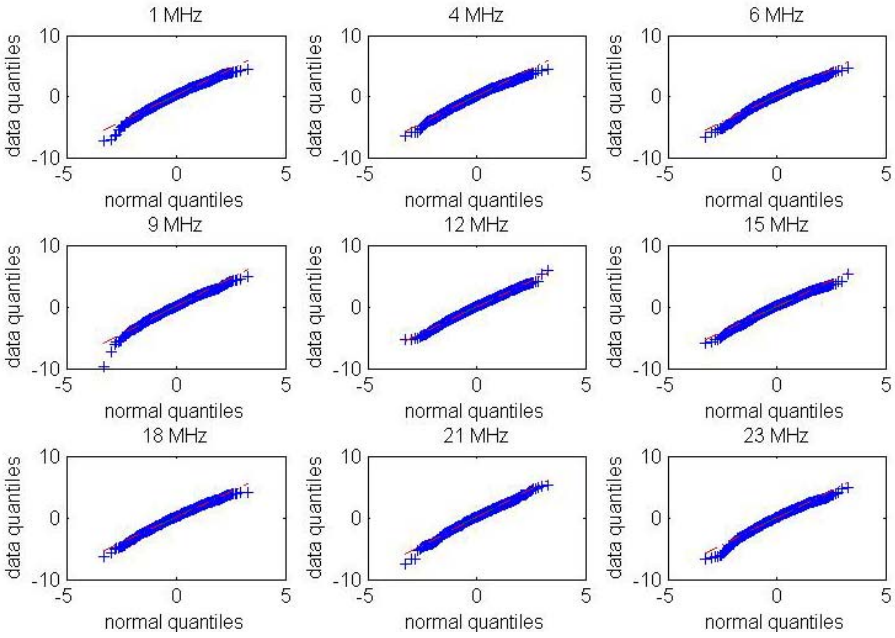

Figure 51 QQ plot of output data of nine frequency bins from the output of the ACRE with the summing baseline method and $TBW \approx 6$ versus a Gaussian distribution.

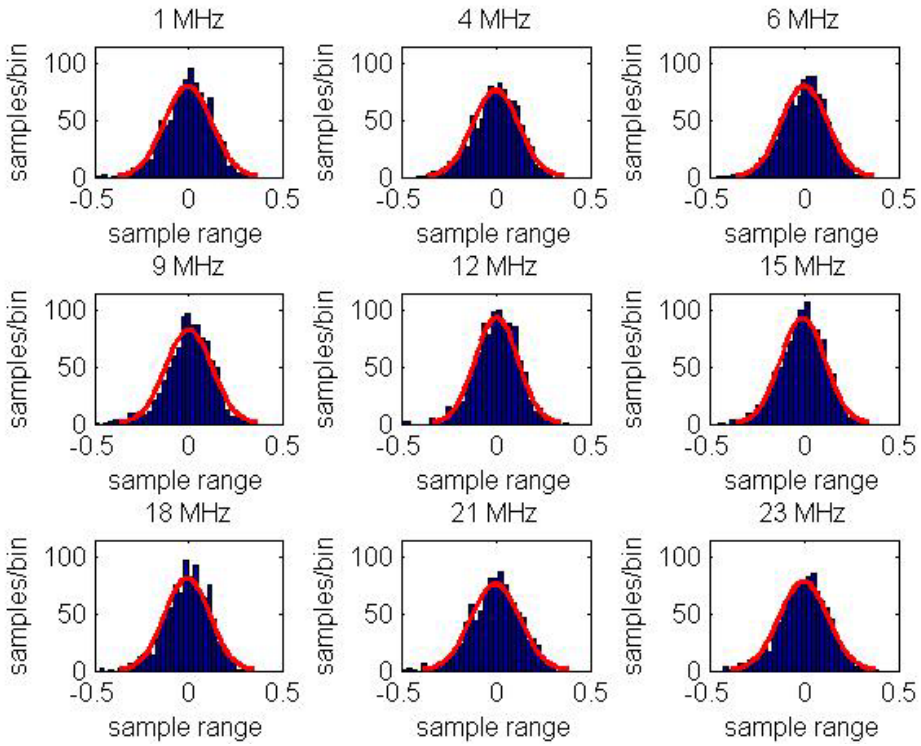

Figure 52 Gaussian estimate (line) and histogram of nine frequency bins from the output of the ACRE with the division baseline method and $TBW \approx 6$.

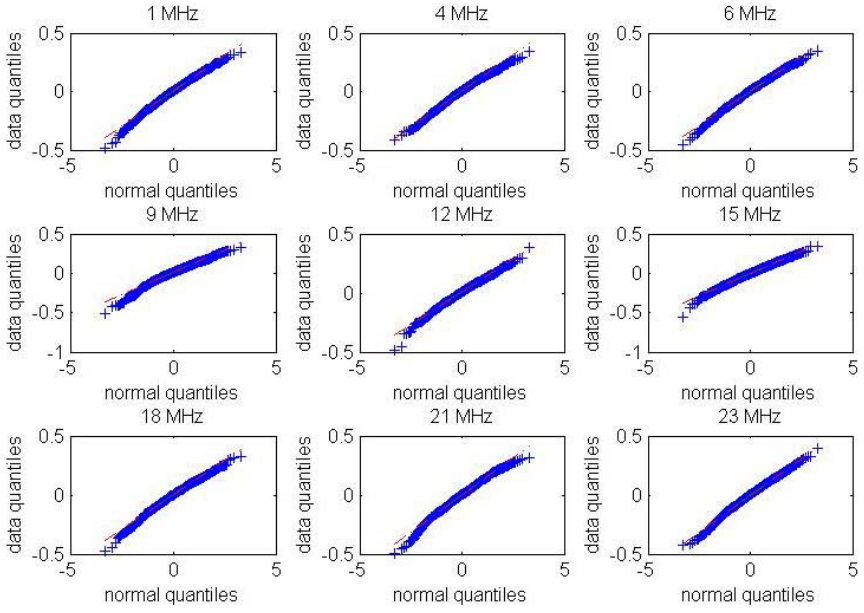

Figure 53 QQ plot of output data of nine frequency bins from the output of the ACRE with the division baseline method and $TBW \approx 6$ versus a Gaussian distribution.

The goodness-of-fit tests used in Chapter III are applied for four combinations of BW and time as shown in Figure 54 and Figure 55 for both ACRE baseline methods, and the results, in light of Chapter III, support the assumption that the Gaussian model improves as TBW increases. These results are not intended as proof that the data is well modeled as Gaussian but rather as support of the trend with respect to TBW. The performance of the two baseline methods with respect to the goodness-of-fit tests used is surprisingly similar.

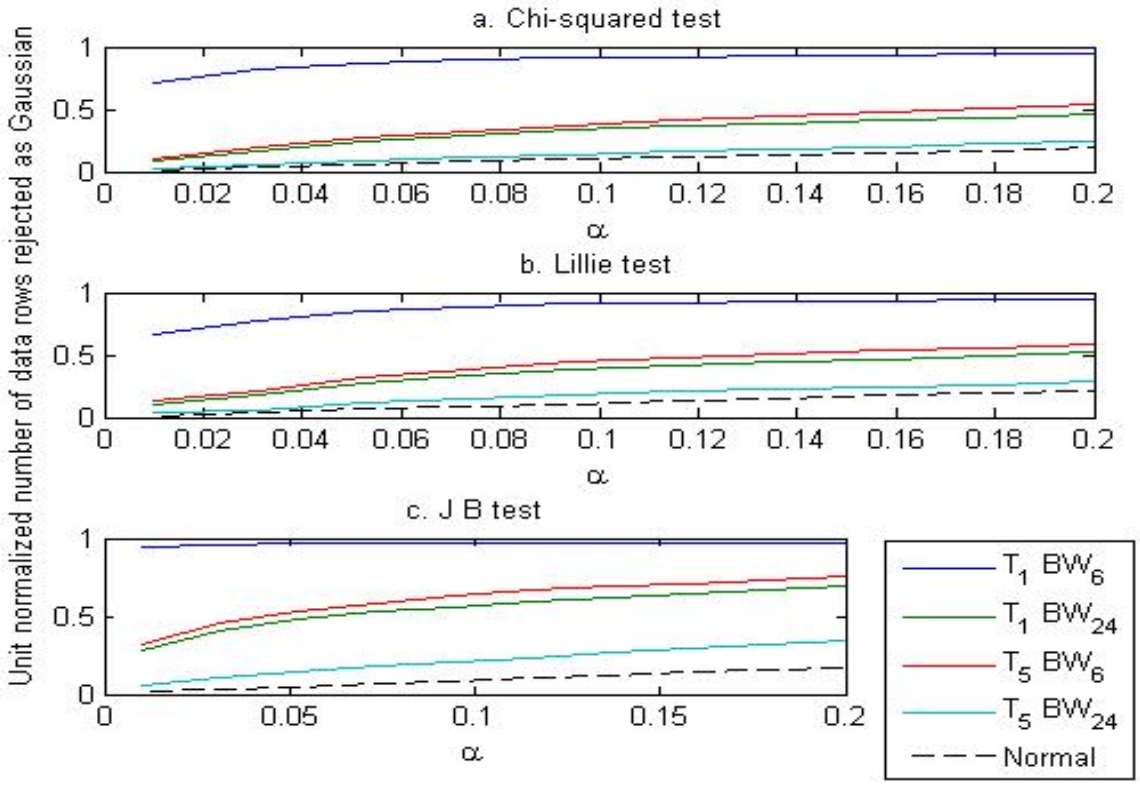

Figure 54 Goodness-of-fit tests using the output from ACRE with the summing baseline method the subscript of T is the time in ms and the subscript of BW is the bandwidth in kHz (solid lines) compared with Gaussian distributed random numbers (dashed line) as a frame of reference.

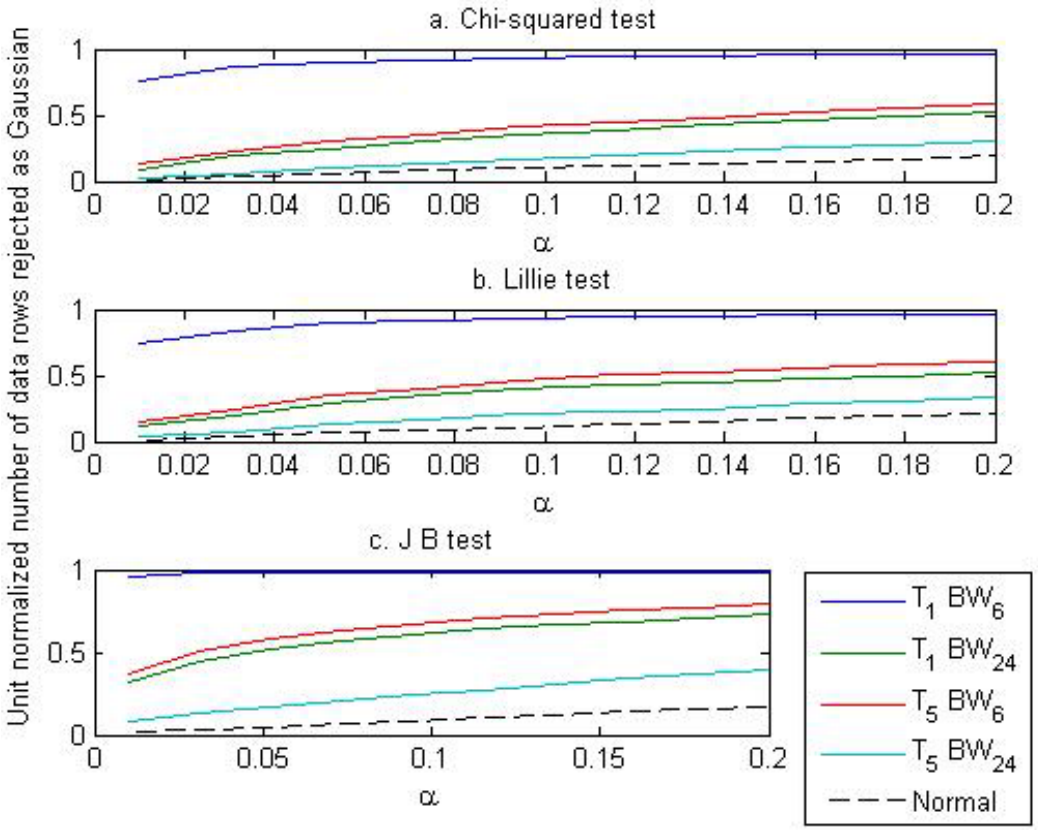

Figure 55 Goodness-of-fit tests using the output from ACRE with the division baseline method the subscript of T is the time in ms and the subscript of BW is the bandwidth in kHz (solid lines) compared with Gaussian distributed random numbers (dashed line) as a frame of reference

Only one baseline method is needed, and the summing baseline method is chosen to determine the threshold since this method results in an output that is modeled as a Gaussian slightly better than with the division baseline method. The spectral growth in Section V.C also supports the selection of the summing baseline method over the division baseline method. The mean and std for each bin for the ACRE output using the summing baseline method when $TBW \approx 30$ is shown in Figure 56. The results in Figure 56 show that the mean and std of the ACRE output from bin to bin are low variance variables. Since the results for the other values of TBW are similar to those shown Figure 56, they are not shown. The ACRE output bin mean and bin std appear similar to AWGN: they are examined using a histogram fitted with a Gaussian distribution in Figure 57 for $TBW \approx 30$ and are postulated as Gaussian based on the results.

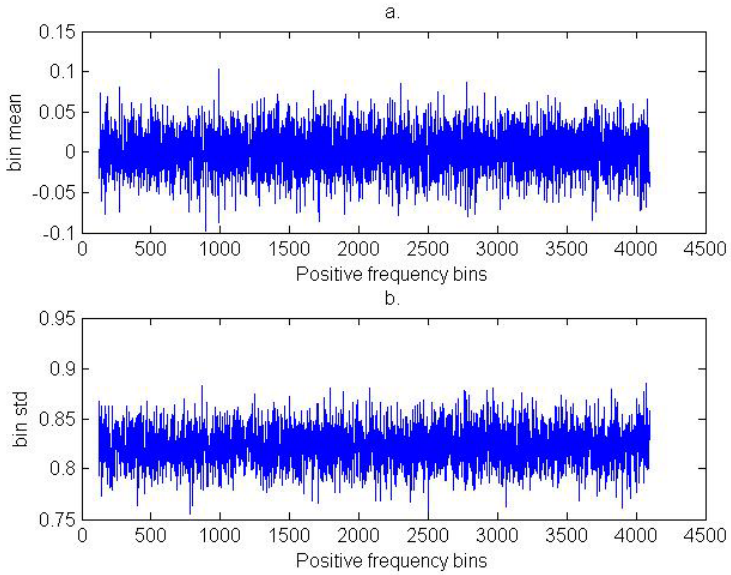

Figure 56 Frequency bin versus bin mean (top) and frequency bin versus bin std (bottom) for ACRE output with the summing baseline method and $TBW \approx 30$.

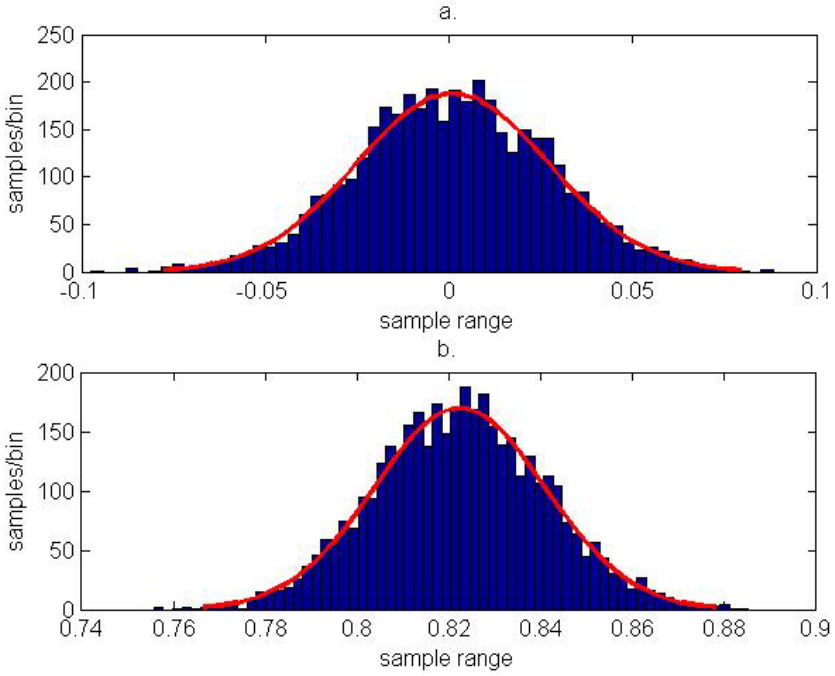

Figure 57 Gaussian estimate (line) and histogram of nine frequency bins from the output of the ACRE with the division baseline method and $TBW \approx 30$.

Mid and upper-estimates of the mean and std of the Gaussian pdf which models ACRE's output are obtained from the data using the postulate that ACRE's output, the bin mean, and bin std can all be modeled as a Gaussian distributed RV. The mid-estimate of the ACRE output mean $\overline{x}_{\overline{b}}$ is obtained by first taking the mean of each bin output $\overline{b}$ and then taking the mean of the bin means for the bins within the frequency search range. The mid-estimate of the ACRE output std $\overline{x}_{\sigma_b}$ is obtained by first taking the std of each bin output σ_b and then taking the mean of the bin stds for the bins within the frequency search range.

To obtain an upper-estimate of the ACRE output mean and std, an additional parameter *d* is needed. The parameter *d* is analogous to the number of std above the mean that a threshold is set to achieve a desired probability of false alarm. The upper-estimate of the ACRE output mean is obtained by first taking the mean of each bin output $\overline{b}$, then taking the std of the bin means $\sigma_{\overline{b}}$ multiplied by *d*, and then summing the result with the mid-estimate of the ACRE output mean resulting in $\left(\overline{x}_{\overline{b}} + d\sigma_{\overline{b}}\right)$. The upper-estimate of the ACRE output std is obtained by first taking the std of each bin output σ_b, then taking the std of the bin stds σ_{σ_b} multiplied by *d*, and then summing the result with the mid-estimate of the ACRE output std resulting in $\left(\overline{x}_{\sigma_b} + d\sigma_{\sigma_b}\right)$.

Given the foregoing, the ACRE threshold is set. The threshold upper-estimate is postulated as

$$\gamma_u = \left[\left(\overline{x}_{\overline{b}} + d\sigma_{\overline{b}}\right) + d\left(\overline{x}_{\sigma_b} + d\sigma_{\sigma_b}\right)\right], \tag{5.2}$$

where *d* is the same as discussed in the preceding paragraph. The threshold mid-estimate is postulated as $\gamma_m = \overline{x} + d\sigma_x$. Threshold estimates and associated statistics for seven different TBW values are shown in Table 4. The values for the threshold estimates are set such that the probability of false alarm $P_f = 2.33\times10^{-4}$, which corresponds to $d = 3.5$ std above the mean [43]. The additional lower value of $d = 3.18$ for the threshold upper-estimate and higher value of $d = 3.89$ for the mid threshold estimate are shown in Table 4 to facilitate a comparison of the two threshold estimations in Section V.C.

Table 4 Simulation based statistics used to compute the threshold estimates along with two values for the threshold estimates with respect to the TBW.

TBW	$\overline{x}_{\bar{b}}$	$\sigma_{\bar{b}}$	$\overline{x}_{\sigma_b}$	σ_{σ_b}	γ_u		γ_m	
d	-	-	-	-	3.5	3.18	3.89	3.5
24	10^{-3}	0.0261	0.8222	0.0186	3.20	2.88	3.20	2.87
36	10^{-3}	0.0213	0.673	0.0154	2.62	2.35	2.62	2.36
48	10^{-3}	0.0184	0.578	0.0129	2.25	2.03	2.25	2.03
72	10^{-3}	0.0149	0.4711	0.0107	1.83	1.66	1.83	1.65
96	10^{-3}	0.0129	0.4076	0.0093	1.59	1.43	1.59	1.43
144	10^{-3}	0.0105	0.3328	0.0074	1.29	1.17	1.30	1.17
192	10^{-3}	0.0092	0.2879	0.0064	1.12	1.01	1.12	1.01

From Table 4 it is clear that the simulation based std statistics used to compute the threshold estimates vary with respect to the TBW. Since only the std related statistics vary, some properties of the variance are considered. The first property considered is that the variance of the product of a RV and a constant is

$$\text{var}\left(aX\right) = a^2 \,\text{var}\left(X\right) = a^2\sigma^2, \tag{5.3}$$

where a is a constant, X is a RV, and σ^2 is the variance of the RV [71]. Another property is that the variance of the sum of n IID RVs with variance σ^2 is [71]

$$\text{var}\left(\sum_{i=1}^{n} X_i\right) = n\sigma^2. \tag{5.4}$$

Applying (5.3) to the scalar $1/n$ and (5.4) to the summation $\sum_{i=1}^{n} X_i$, we get the variance of the sample mean $\overline{X} = \frac{1}{n}\sum_{i=1}^{n} X_i$ as

$$\text{var}\left(\overline{X}\right) = \left(\frac{1}{n}\right)^2 n\sigma^2 = \frac{\sigma^2}{n}. \tag{5.5}$$

The value *n* is related to the number of samples and, hence, TBW since the BW and sampling frequency are constant in the simulations, and the std equals the positive square root of the variance. As a result, it is expected that $\sigma_{\bar{b}}$ will vary as the inverse square of the TBW.

This expected result is confirmed in Figure 58.a along with similar results for $\bar{x}_{\sigma_b}$ and σ_{σ_b}, shown in Figure 58.b and Figure 58.c, respectively. The *y*-axis is normalized by the smallest TBW, which is 24. The *x*-axis is normalized by the value of the statistic which corresponds to the smallest TBW. From (5.5) and the results in Figure 58, a single measure of the statistics in Table 4 for a specific TBW can be extrapolated for other TBW values.

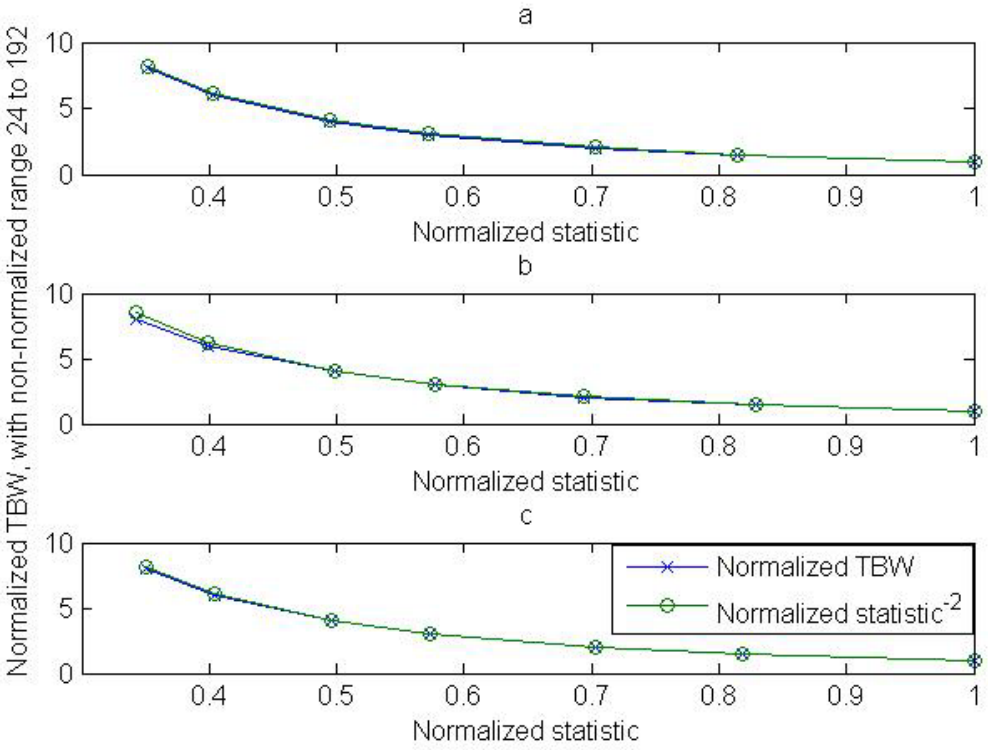

Figure 58 The Table 4 simulation results plotted using the normalized TBW and inverse square of the statistics $\sigma_{\bar{b}}$ (plot a), $\bar{x}_{\sigma_b}$ (plot b), and σ_{σ_b} (plot c).

C. STANDARD ACRE RESULTS (HALF-SINE PULSE SHAPING)

This section presents a simulation-based evaluation of standard ACRE. Variations of ACRE will be presented in Section V.D, and ACRE as thus far presented is referred to as "standard ACRE." The PSD estimate's output is in dB. An example of the output from the PSD estimator is shown in Figure 59. Figure 60 shows the output of standard ACRE. The results contributed to the decision of using the summing baseline method instead of the division baseline method. The output from the division baseline method is dimensionless. Decision 2 from Figure 49 is the output of the summing baseline method. As seen in Figure 60, the division baseline method (top) has spectral growth at the high frequencies.

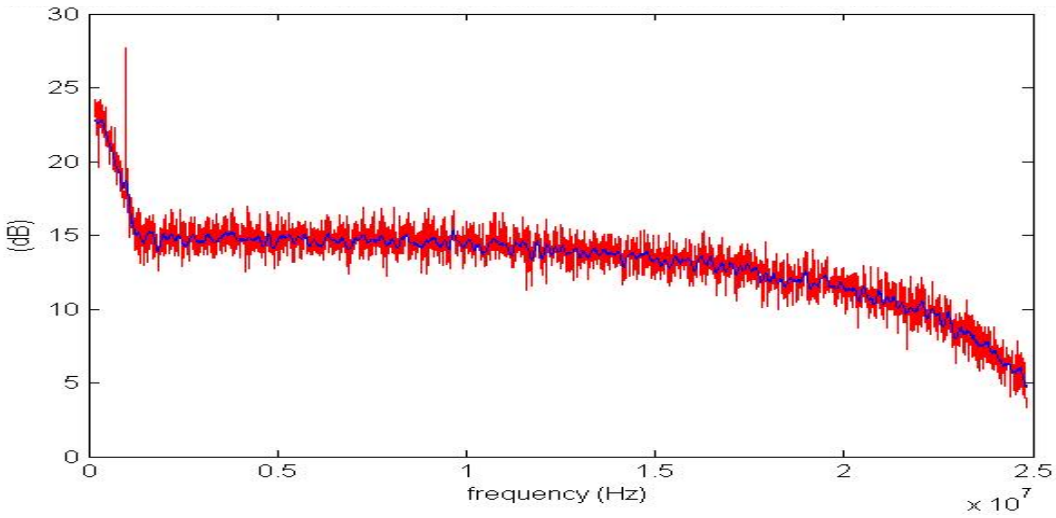

Figure 59 PSD output signal (red) with frequency bin baseline signal (blue).

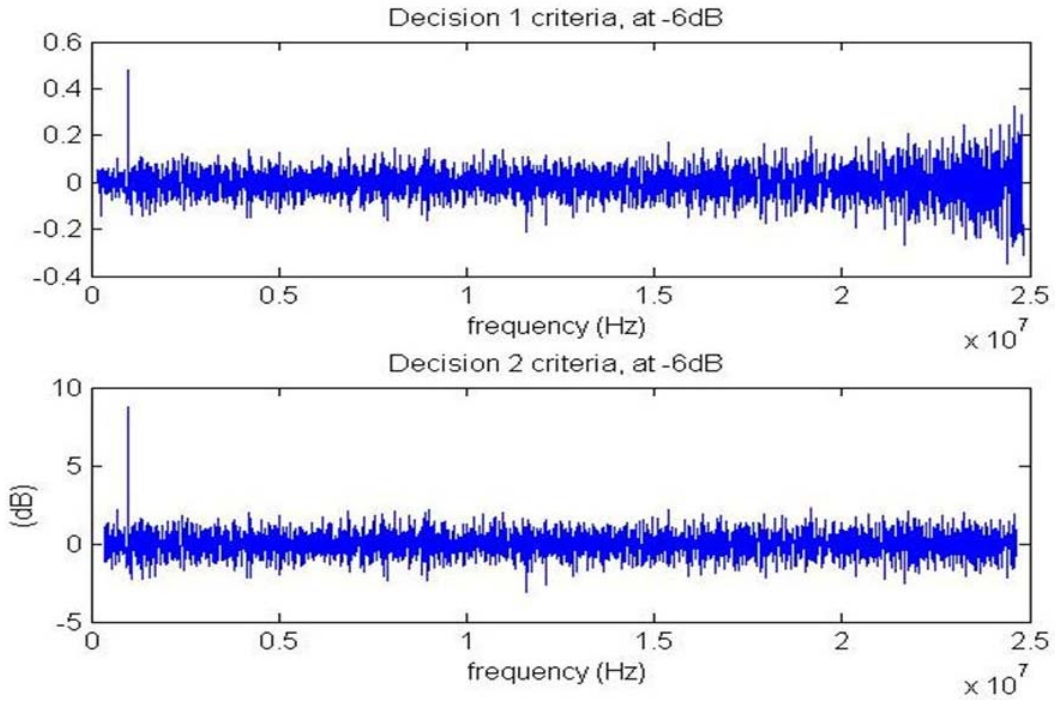

Figure 60 Input into the comparator for the division (top) and the summing (bottom) baseline methods.

Single simulations with chip rates that spanned the search range were evaluated to ensure that ACRE would perform over the entire chip rate search range. Figure 60 shows the simulation SNR values used are relatively high, as seen by the relative difference between the chip rate line and the noise. All single simulation results are within 2 dB for the summing baseline method. The chip rate shown in Figure 60 and the threshold upper estimates are used for the remaining simulations discussed in this chapter. The value $BW = 6$ kHz is used in the remaining simulations in this section. Figure 61 plots the probability of detection estimate versus SNR levels for various TBW values.

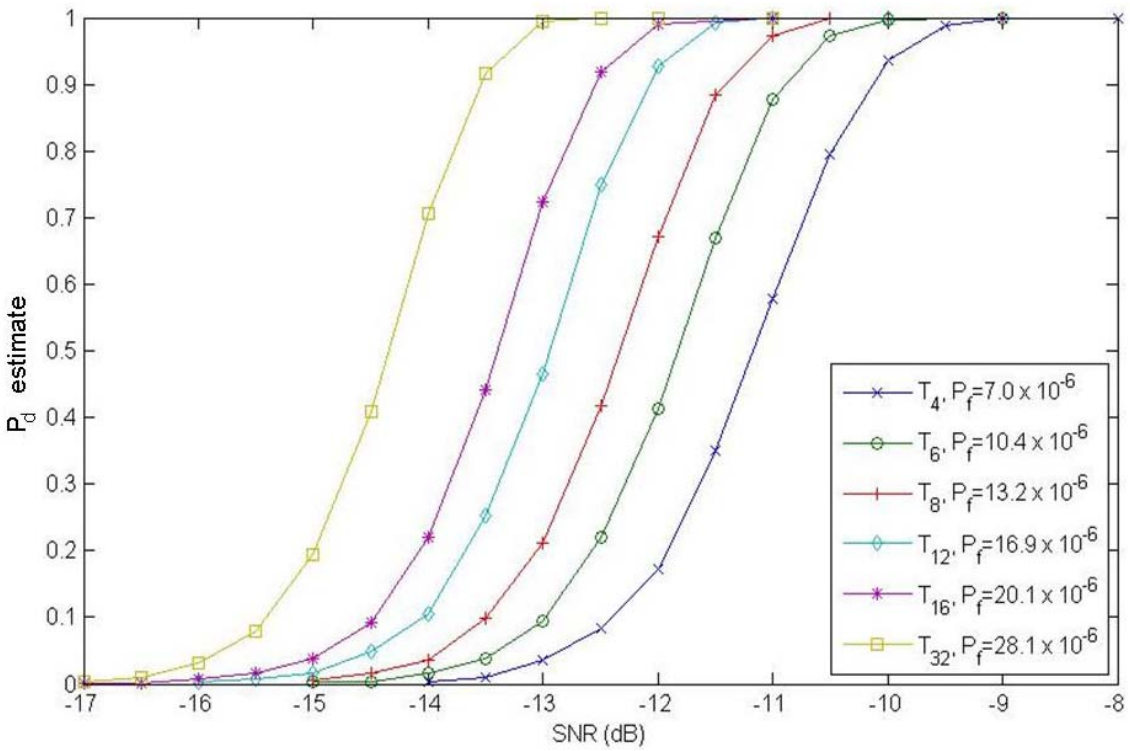

Figure 61 Estimated P_d versus SNR with standard ACRE for data durations from four to thirty-two ms with the associated upper-estimate of the probability of false alarm for d=3.5.

The probability of detection estimate is based on the ratio of the number of times the standard ACRE output exceeds the threshold at the frequency bin corresponding to the chip rate to the number of times that standard ACRE is cycled for that simulation run. Each simulation run corresponds to a specific value of TBW and SNR, the number of cycles per run is 5,000. The value $d = 3.5$ is selected to generate results shown in Figure 61. The simulation estimate of the probability of false alarm and the time for each simulation result, as indicated by T's subscript, are shown in the legend of Figure 61.

Simulation results in Figure 61 show a 1 dB standard ACRE performance improvement as the TBW is doubled. The estimate of the probability of false alarm for all TBW is significantly lower than the probability of false alarm associated with the threshold upper-estimate $P_{f\_u} = 2.33 \times 10^{-4}$ obtained using $d_u = 3.5$. The threshold mid-estimates with $d = 3.89$ are equivalent to the threshold upper-estimates for $d = 3.5$ with

specified TBW values as shown in Table 4. From this relation, the probability of false alarm associated with the threshold mid-estimate is $P_{f\_m} = 50 \times 10^{-6}$, obtained using $d_m = 3.89$. The simulation based estimate of the probability of false alarm ranges in value from 7×10^{-6} to 28×10^{-6}, as shown in Figure 61. These simulation based estimates of probability of false alarm exceed both $P_{f\_m} = 50 \times 10^{-6}$ and $P_{f\_u} = 2.33 \times 10^{-4}$, thus the threshold mid-estimate approach is selected.

An additional simulation set was run using a threshold upper-estimate with $d = 3.18$ or equivalently using a threshold mid-estimate with $d = 3.5$ per the results in Table 4, and results are shown in Figure 62. As expected the lower threshold shifts the standard ACRE performance curves to the left, and the estimated probability of false alarm increases. The improved estimated probability of detection is a little less than half a dB. The estimated probability of false alarm for all values of TBW are less than the probability of false alarm associated with the threshold mid-estimate of $P_{f\_m} = 233 \times 10^{-6}$. The final observation of the simulation results shown in Figure 61 and Figure 62 is that the estimated probability of false alarm increases with increasing TBW.

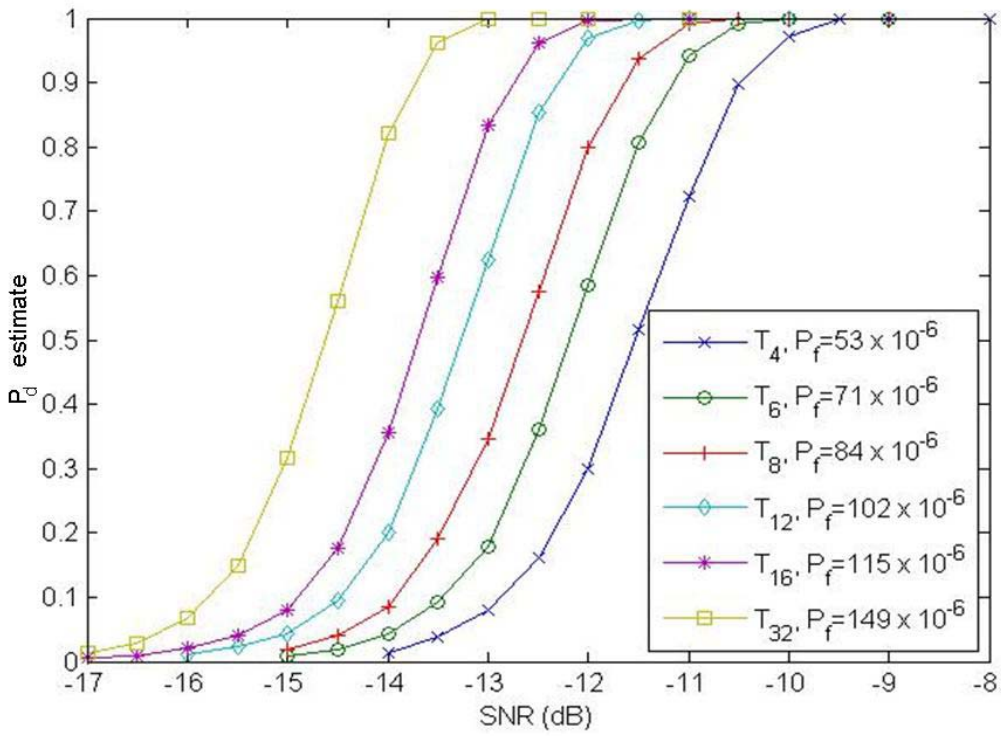

Figure 62 Estimated P_d versus SNR with standard ACRE for data durations from four to thirty-two ms with the associated upper-estimate of the probability of false alarm for d=3.18.

Simulations indicate that the relative change of the estimated probability of false alarms associated with the simulation results in Figure 61 is approximated by the relative change in TBW to the 0.65 power, using a similar approach which generated the results in Figure 58. The 0.65 power is determined visually verses a least squares fit since this result is intended to be a subjective observation. Similarly, the relative change of the estimated probability of false alarms associated with the simulation results in Figure 62 is approximated by the relative change in TBW to the 0.53 power. The explanation for this observation is undetermined.

D. INCREMENTING ACRE AND ACRE WITH ADDITIONAL FILTERING RESULTS (HALF-SINE PULSE SHAPING)

The probability of false alarm is set as $P_f = 0.025$ to compare ACRE and CRD approaches as in [11], which corresponds to 1.96 std above the mean [43]. In the

simulations there are numerous false alarms since the P_f is set such that on average a false alarm will occur once every 40 measurements. As a result, a different method is used to determine the estimated probability of detection. The bin with the maximum amplitude is assumed to be an estimate of the chip rate R_{ce}. The signal is present in the simulations, so the P_d estimate equals the number of times that $R_{ce} = R_c$ in a given simulation divided by the number of runs in the simulation. Each P_d estimate is computed with five thousand simulations.

An example of the output from the PSD estimator with additional filtering is shown in Figure 63. The flat frequency response in Figure 63 illustrates how filtering reduces the upper frequency search range. Another factor that contributed to the decision to use the summing baseline method versus the division baseline method is that the ACRE with division baselining appears to have a frequency component throughout the bins, as shown by the oscillating response of the ACRE output in the top plot of Figure 64.

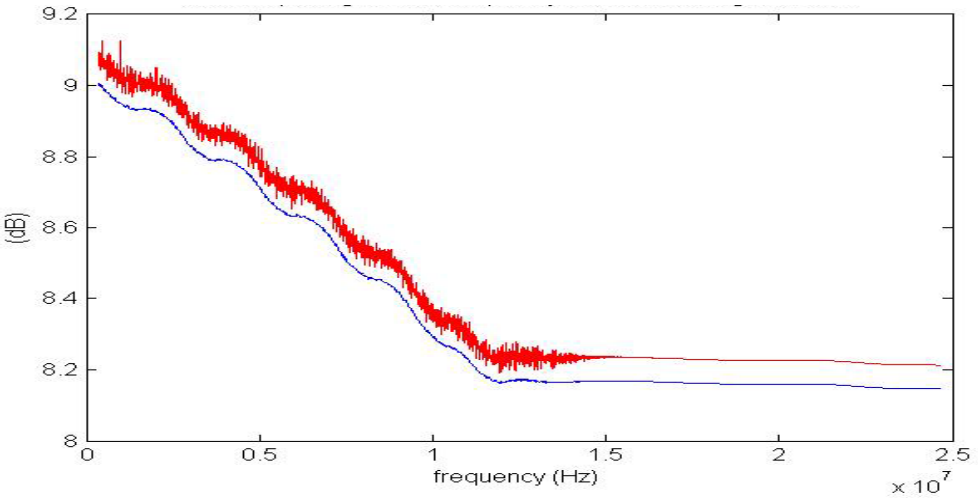

Figure 63 PSD output signal (red) with frequency bin baseline signal (blue) below with additional filtering.

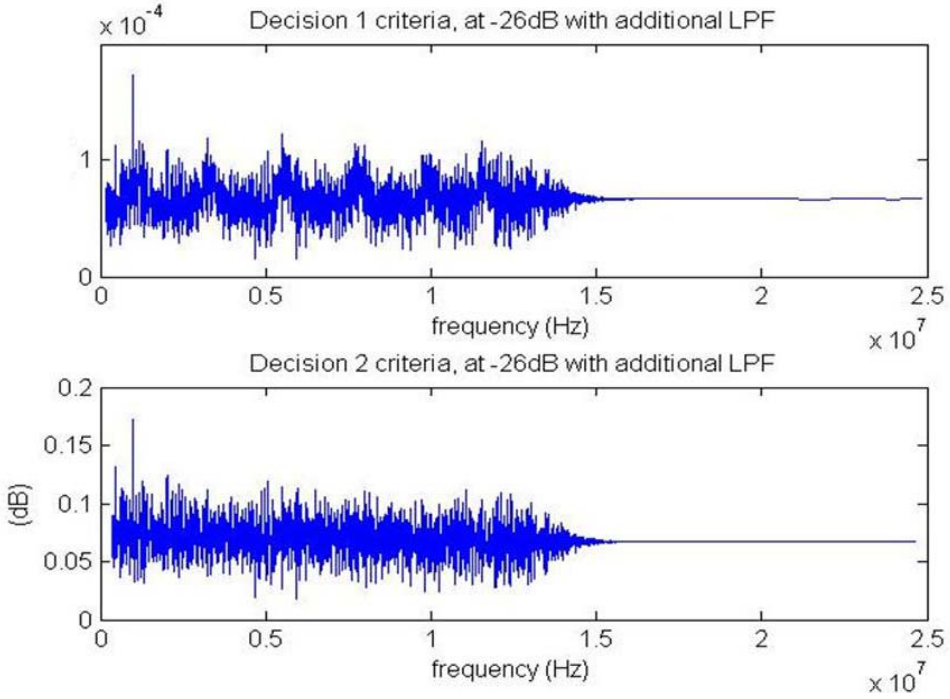

Figure 64 Comparator input for division (top) and summing (bottom) baseline methods when additional filtering is used. The duration of the data segment is greater than 32 ms.

The three main categories of simulation are standard-ACRE, ACRE with added filtering, and ACRE with incrementing. Standard-ACRE follows the block diagram in Figure 5, and results are presented in Figure 65. ACRE with added filtering has a LPF prior to the PSD estimator, thus reducing the R_c search range. The filtering used to produce the results in Figure 66 reduced the R_c search range to 0.5 to 6 MHz from 0.5 to 22.5 MHz. Additional filtering improves the performance by five to six dB at a cost of reducing the search range to about a quarter of the original range.

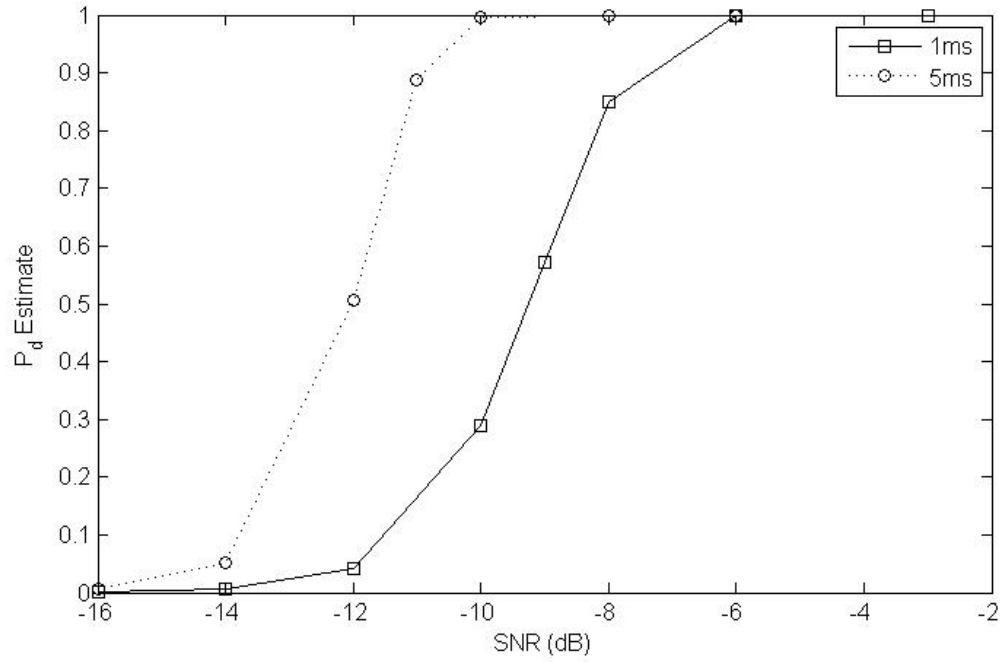

Figure 65 Estimated P_d versus SNR with standard ACRE for data durations of 1 ms and 5 ms.

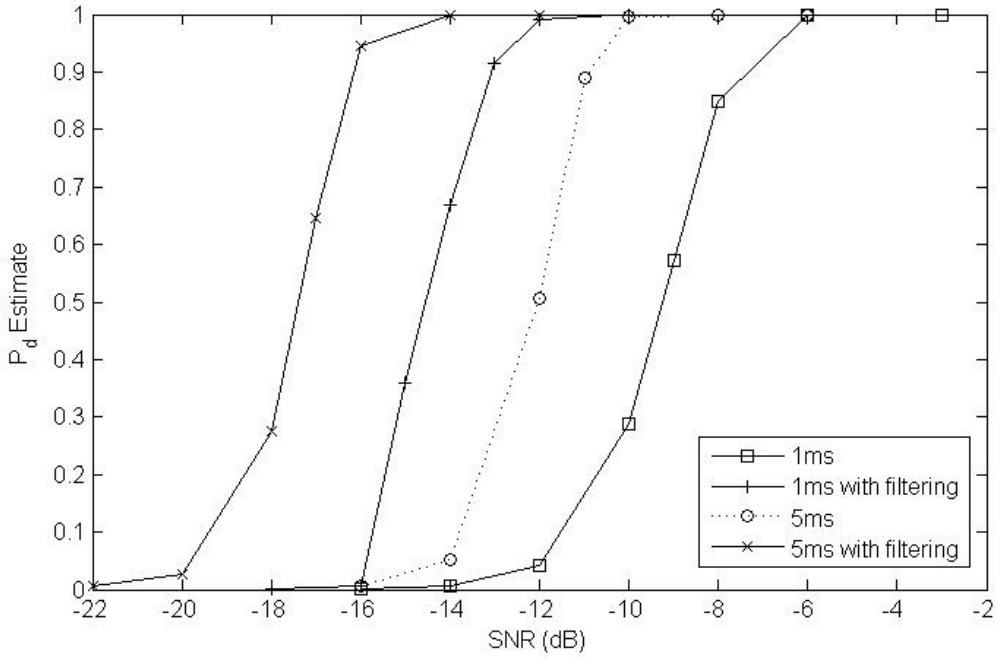

Figure 66 Estimated P_d versus SNR with added filter ACRE compared with standard ACRE for data durations of 1 and 5 ms.

The bandwidth of the CRD integrator is inversely proportional to the integration time [11]. To narrow the PSD estimator bin bandwidth, either more points must be included or less bandwidth must be covered. An alternate approach is to sum the output results for a number of independent time frames. The number of factors that must be met to ensure this approach is valid is not addressed in this work. Rather, the approach is evaluated with simulations. Set-size is the number of times that the PSD estimate is summed. The set-size can be non-overlapping such as a set size of 5 where data of duration 5 ms is separated into five 1 ms data sets, then processed and the results summed. Alternately, overlapping the time frames to produce more bin estimates within the same time frame is also briefly evaluated. Increment-size is the ratio of previously unprocessed data to the amount of data used to compute a PSD estimate.

ACRE with incrementing is accomplished by processing subsections of the data through the PSD estimator, summing the processed data, frequency bin baselining the summed data, and making a decision at the comparator. Figure 67 shows simulation results for two incrementing approaches which use a data duration of 5 ms. In the first approach the set-size is five and five separate 1 ms results are summed. In the second approach, twenty-one 1 ms subsection results are summed, where each successive subsection overlaps the next subsection by twenty percent, or 0.2 ms. The comparable performance of standard-ACRE and ACRE with incrementing illustrates the potential to process the data in parallel without performance loss.

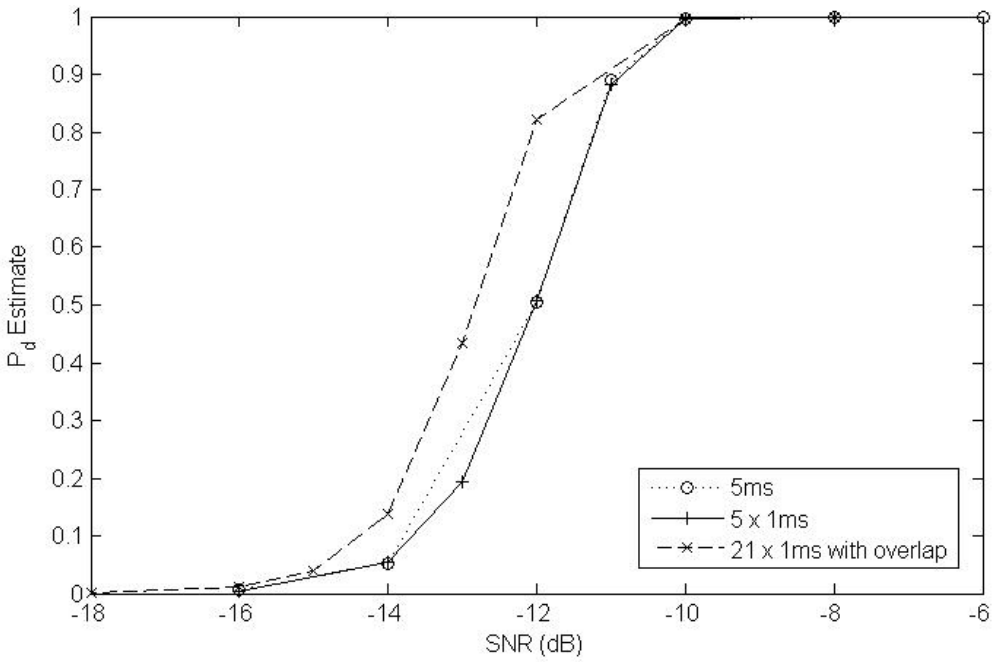

Figure 67 Estimated P_d versus SNR with standard ACRE compared with incremented ACRE, with and without overlap. The total data duration is 5 ms for all simulations.

The potential to parallel process the data has some distinct advantages. One advantage is that the time requirements to process data maybe greatly reduced. Another advantage is that previously processed data can be combined with unprocessed data to further validate results. The results in Figure 67 illustrate how increment-processing 1 ms segments can lower the noise floor and move the P_d curve to the left. The most obvious advantage is the 1 dB performance advantage achieved using overlap as illustrated in Figure 67. Overlapping provides improved performance at the cost of increased computational complexity.

Reference [11] has similarly shaped laboratory based performance curves with associated corresponding theoretical functions. Although some performance comparisons between the CRD and the ACRE can be discussed, it is not equitable to compare their performance closely. The comparison can only be taken so far since the ACRE is considerably more complex and is designed to estimate the chip rate, whereas the CRD requires more signal characteristic a-priori knowledge and is designed to detect the chip

rate when the baseband data waveform uses rectangular pulses. Other dissimilarities include digital versus analog computing and the respective chip rate frequency ranges for which the CRD and the ACRE are effective.

The simulation set-up, decision criteria development, and simulation results were presented in this chapter. The simulation set-up includes a description of the various parameters and signals used. The decision criteria as a function of TBW and the application of the central limit theorem were discussed. The summing baseline method was selected. Standard ACRE, ACRE with additional filtering, and incremented ACRE were discussed and their performances compared.

THIS PAGE INTENTIONALLY LEFT BLANK

VI. CONCLUSIONS

This research investigated detection and estimation methods for the two most common types of SS systems, frequency-hopped SS and direct sequence SS. For FH-SS, detection and estimation of the hop-frequencies was examined. For DS-SS, detection and estimation of the chip rate was examined. For FH-SS, we extended the work originally developed in [40] to evaluate the detector in an interference plus AWGN environment, and preliminary results are reported in [72]. For DS-SS, we considered an ad-hoc chip-rate estimator scheme, and preliminary results were reported in [73]. This section summarizes findings observed for the exponential averaging FH detector and the ad-hoc chip-rate estimator. Section VI.B provides recommendations for future work, and Section VI.C summarizes the contributions of this dissertation.

A. SUMMARY AND CONCLUSIONS

1. Exponential Averaging FH Detector

Chapter II presented an extension of the exponential averaging FH detector in [40]. Several major differences exist between the work discussed in [40] and that examined in this dissertation. This work investigates the effect of AWGN, which was not considered in [40], along with wideband interference and narrow band interference signals which was considered earlier. Next, estimation of the PSD was conducted using the absolute value squared instead of the absolute value operation, and the spectral estimate of the interference plus noise was computed using a summation, a weight factor, and a scaling factor instead of obtaining it recursively in order to reduce computational and analytic complexity.

Different initial conditions were used in terms of the recursive computation of the spectral estimate, resulting in improved detector performances for weight factors close to one. Note that the initial conditions in [40] are such that the number of estimated frequency hops decreases when the weight factor approaches unity, but the estimate of

the remaining hops is more pronounced. As an aside, although the use of the weight factor is described in a consistent way for the two references, the weight factor as described [40] is one minus the weight factor in [72] and this dissertation.

Signals used were described along with the metrics by which the detector is evaluated. The detector's performance was displayed as plots of SIR versus simulation-based estimates of the P_d for given SNR values. The scaled subtraction and quotient-combining methods were described, and the analytic expression for the pdf that models the detector's output with scaled-subtraction-combining and an AWGN plus BPSK input was developed. Finally, it was shown that an analytic expression for the pdf that models the detector's output with either combining method and an AWGN plus BPSK plus CW input is mathematically intractable as far as can be determined. Therefore, a heuristic approach to estimating the pdf of $f_{\tilde{S}|x=i+n}(\tilde{S} \mid x = i + n)$ was addressed in Chapter III.

Chapter III provided the exponential averaging detector's simulation set-up, decision criteria development, and various simulation results. The simulation set-up included the description of the various parameters and signals used. The decision criteria section investigated two methods to heuristically evaluate a pdf model of the detector's output: histograms and goodness-of-fit tests. Simulation results included performance guidelines, an evaluation of the goodness-of-fit tests, the detector data evaluated by the goodness-of-fit tests, threshold estimates, bounds on P_f, and an evaluation of the detector's performance. Finally, the performance of the detector for various values of SNR and SIR was investigated.

2. ACRE

ACRE was developed and described in Chapter IV. Although theoretical analysis of the system is investigated, simulation results are primarily used to describe and set parameters. The approach used to develop ACRE is by comparing and contrasting it to the CRD approach. One contrast between ACRE and the CRD is that the CRD requires an estimate of the chip rate, whereas ACRE only requires a range of values for the chip rate. Thus, as the name implies, the primary purpose of the CRD is to detect the chip rate and not to estimate it. ACRE simultaneously searches a specified bandwidth and

estimates the chip rate. This simultaneous search and estimation provides a significant performance advantage over the CRD, which requires that the detector scan through a specified bandwidth in order to detect the chip rate. However, simultaneous search and chip rate estimation results in increased complexity.

The performance of the CRD with half-sine pulse shaping is shown using Fourier series coefficients. Results showed the performance of the CRD with a half-sine shaped pulse is degraded significantly. ACRE is then described in a block diagram and the various blocks described. The PSD estimator block closely parallels the CRD spectral component.

The need to compare a number of sequential frequency bins, covering the frequency search range, requires that a method to baseline the bins' output be developed. The motivation for baselining a signal so that it can be compared throughout its entire frequency range was presented. The summing and division methods of baselining the bins' output were developed. Section IV.B briefly discussed the complexity of deriving an analytic expression for the pdf of the RV that models the ACRE output. The decision to use a simulation-based estimate of the RV that models the ACRE output was discussed in Chapter IV and implemented in Chapter V.

Chapter V presented the ACRE simulation set-up, decision criteria development and simulation results. The simulation set-up includes a description of the various parameters and signals used. In the decision criteria section, a threshold was generated using the estimated pdf and a predetermined P_f. The decision criteria as a function of TBW and the application of the central limit theorem were discussed. The summing baseline method was selected based on performance comparisons of the two baseline methods. Some subjective comparisons were made between the CRD and the ACRE performances.

Three ACRE-based simulation approaches were considered: standard-ACRE, ACRE with additional filtering, and ACRE with incrementing. Filtering trades off chip rate search range for estimation performance. A quantitative illustration of the trade-off is that the reduction of the search range to a quarter of the original range generated an

additional 5 to 6 dB in performance gain. Incrementing shows the potential for parallel processing without loss of performance as well as trading performance for computations. A quantitative illustration of incrementing shows that the relative computational cost, 20 times the standard cost, generated small 1 dB of performance gain. The performance of the three ACRE simulations were plotted with SNR versus a simulation based estimate of the probability of detection.

B. CONTRIBUTIONS OF THIS RESEARCH

This study expanded and improved original work presented in [40]. The increased complexity and realism of AWGN was added to the wideband plus narrow band interference detector input signals. It is a common mistake in research of this type to neglect the effects of AWGN since, generally, the narrowband interference noise power is assumed to be dominant. However, this approach often obscures the effect that AWGN has on the process and the significant interaction between the effects of AWGN and the narrowband interference that frequently occurs. Hence the addition of AWGN is a significant improvement over previous work on this detector. Next, detection performance was improved by changing the exponential averaging FH detector's initial conditions. The change in initial conditions allowed for the use of weight factors which are closer to one without the drawback of suppressing any estimated frequency hops, which was a drawback in [40].

The restructure of the detector code from a recursive algorithm and the addition of the scaling factor, along with other minor changes, facilitated changes in the initial conditions and allowed an analytic analysis of the pdf of the RV which models the detector's output for a special case. The analytic expression for the pdf of the RV which models the detector's output for the special case of the input being AWGN plus a BPSK signal given scaled-subtraction-combining was obtained. The study heuristically supported the postulate that detector's output can be modeled by a Gaussian RV. Upper and mid-estimates for the probability of false alarm were developed to set the detector's threshold.

The development of the exponential averaging FH detector's decision criteria laid the ground work for the detector to be evaluated. The detector's performance was evaluated over a significant range of SNR and SIR, and the results were plotted as a simulation-based probability of detection estimate versus SIR for fixed SNR and probability of false alarm. From the simulation estimate of the probability of false alarm, the upper-estimate for the probability of false alarm was selected.

Finally, this research also presented the conception, development, implementation, and evaluation of ACRE. This research heuristically supported the postulate that standard ACRE's output can be modeled as a Gaussian RV. Upper and mid-probability of false alarm estimates were developed and the mid-estimate was selected based on the simulation probability of false alarm results. Standard ACRE's performance with a pulse shaped signal input was evaluated, and the result plotted as a simulation-based probability of detection estimate versus SNR for a fixed probability of false alarm. The result was a probability of detection estimate of one-half at SNR= −11 dB and SNR= −15 dB for TBW=24 and TBW=196, respectively. Based on the simulation results, standard ACRE's performance improved 1 dB as the TBW was doubled.

ACRE with additional filtering and incremented ACRE were developed as two variations of standard ACRE. Results showed additional filtering improves performance at a cost of a reduced the search range and increased computational complexity. Incremented ACRE shows the potential for parallel processing without loss of performance. Incrementing ACRE with overlap exchanges processing for performance. The practical application of the ACRE scheme in this time of ever increasing inexpensive processing power is greatly expanded since it can be implemented with parallel processing and additional processing can be exchanged for performance.

C. RECOMMENDATIONS FOR FUTURE WORK

This investigation, while answering some questions, also led to some unanswered issues. This section provides some recommended areas of future work. It seems reasonable that the exponential averaging FH detector can be used to estimate the hop

order of a SS-FH signal imbedded in AWGN plus interference signals, and this is a promising area of future work. To flush out the idea, a hop-by-hop analysis of the detector's performance to determine factors for hop detection variation, along with methods to mitigate the performance differences, is recommended as a first step. One question to be answered is how the size of the shift influences which hop frequencies are suppressed when the shifted data is evaluated with the detector. The use of smaller data segments is a potential option since lower weight factors such as $\rho = 0.8$ are effective with scaled-subtraction-combining in the estimation of individual hops. The processed smaller data segments could potentially be combined and evaluated to obtain a hop order estimate.

Another area recommended for future work is the evaluation of both the exponential averaging FH detector and ACRE with other channels such as a fading channel, a wider set of parameters such as the weight factor and bin sizes, other signal types such as MPSK, other pulse shapes such as Gaussian and raised cosine, validate the Gaussian output postulate, and compare the performance of both schemes to other similar detection and estimation schemes. A final area recommended for future work is the investigation of the limits of ACRE with incrementing and the development of efficient algorithms to implement the parallel processing of incremented ACRE.

LIST OF REFERENCES

[1] D. L. Nicholson, *Spread Spectrum Design: LPE and AJ Systems.* Rockville, MD., Computer Science Press, 1988.

[2] A. Polydoros, and C. Weber, "Detection Performance Considerations for Direct Sequence and Time hopping LPI Waveforms," *IEEEE J. Selected Areas Communications,* Vol. SAC-3, pp. 727-744, September 1985.

[3] R. Peterson, R. Ziemer, and D. Borth, *Introduction to Spread Spectrum Communications,* Upper Saddle, NJ:, Prentice Hall, 1995.

[4] P. Green, "The Output Signal-to-Noise Ratio of Correlation Detectors," *IRE Transactions on Information Theory,* pp. 10-18, March 1957.

[5] J. Proakis, *Digital Communications*, 4th ed., Boston, MA., McGraw-Hill, 2001.

[6] D. Torrieri, *Principles of Secure Communication Systems*, 2nd ed., Boston, MA., Artech House, 1992.

[7] H. Van Trees, *Detection, Estimation, and Modulation Theory,* New York, NY., Wiley, 1971.

[8] K. Shanmugan, and A. Breipohl, *Random Signals Detection Estimation and Data Analysis,* New York, NY., Wiley 1988.

[9] H. Poor, *An Introduction to Signal Detection and Estimation,* New York, NY., Springer-Verlag, 1988.

[10] R. Bartoszynski, and M. Niewiadomska-Bagaj, *Probability and Statistical Interference,* New York, NY., John Wiley & Sons, 1996.

[11] D. Hill, and E. Felstead, "Laboratory performance of spread spectrum detectors," *IEE Proc.-Commun.,* Vol. 142, No. 4, pp. 243-249, August 1995.

[12] W. H. Beyer, *CRC Standard Mathematical Tables*, 25th ed., Boca Raton, FL., CRC Press, 1981.

[13] C. Chung, "Generalized likelihood-ratio detection of multiple-hop frequency-hopping signals," *IEE Proc.-Commun.,* Vol. 141, No. 2 pp. 70-78, April 1994.

[14] C. Chung, "Detection and Hop-Rate Estimation of Random FH signals via Autocorrelation Technique," *IEEE MILCOM,* pp. 345-349, 1991.

[15] B. Sklar, *Digital Communications Fundamentals and Applications*, Upper Saddle, NJ., Prentice Hall, 2000.

[16] G. R. Cooper, and C. D. McGillem, *Probabilistic Methods of Signal and System Analysis 2nd ed.*, New York, NY., Holt, Rinehart, and Winston, 1971.

[17] L. H. Crockett, N. C. MacEwen, E. Pfann, and R. W. Stewart, "Pulse Shaping for RF Communications in Wireless Sensor Networks" *Asilomar Conference Signals, Systems and Computers*, 39th Conference, 2005, pp. 442-446.

[18] Zigbee Alliance, http://www.zigbee.org/en/index.asp, last accessed 21 December 2006.

[19] R. C. Robertson, EC 3510 Communication Engineering. Unpublished lecture notes, Oct. 2006. (Word Processed).

[20] F. Stremler, *Introduction to Communication Systems*, 2nd ed., Reading, MA., Addison-Wesley, 1982.

[21] A. Polydoros, and C. L.. Nikias, "Detection of Unknown-Frequency Sinusoids in Noise: Spectral Versus Correlation Domain," *IEEE Transactions on Acoustics, Speech, and Signal Processing*, Vol 35, 1987, pp. 897-900.

[22] W. A. Gardener, Signal Interception: A Unifying Theoretical Framework for Feature Detection. *IEEE Communication*, Aug. 1988, pp. 897-906.

[23] H. Urkowitz, "Energy Detection of Unknown Deterministic Signals," *Proc. IEEE 1967*, 55, pp. 523-531.

[24] D. E. Reed, and M. A. Wickert, "Minimization of Detection of Symbol-Rate Spectral Lines by Delay and Multiply Receivers," *IEEE Trans. Commun.*, 1988, 36, pp. 118-120.

[25] J. F. Kuehls, and Evaggelos Geraniotis, "Presence Detection of Binary-Phase-Shift-Keyed and Direct-Sequence Spread Spectrum Signals Using a Prefilter-Delay-and-Multiply Device," *Journal on Selected Areas in Communications*, Vol. 8, Issue 5, 1990, pp. 915-933.

[26] D. A. Hill, and J. B. Bodie, "Experimental Carrier Detection of BPSK and QPSK Direct Sequence Spread Spectrum Signals" *MILCOM*, 1995, pp. 362-367.

[27] D. A. Hill, and J. B. Bodie, "Carrier Detection of Unbalanced QPSK Direct Sequence Signals," *MILCOM* 1999, pp. 437-441.

[28] D. A. Hill, and J. B. Bodie, "Carrier Detection of PSK Signals," *IEEE Transactions Communications,* Vol. 49, Issue 3, 2001, pp. 487-496.

[29] A. Polydoros, and W. Kai, "LPI Detection of Frequency-Hopping Signals Using Autocorrelation Technique," *IEEE Journal on Selected Areas in Communications*, Vol. 3, Issue 5, 1985, pp. 714-726.

[30] C. D. Chung, and A. Polydoros, "Detection and Hop-rate Estimation of Random FH Signals Via Autocorrelation Techniques," *MILCOM.1991.* pp. 345-349.

[31] C. D. Chung, and A. Polydoros, "Parameter Estimation of Random FH Signals Using Autocorrelation Techniques." *IEEE Communications*, February/March/April 1995, pp. 1097-1106.

[32] M. Janani, V. T. Vakili, and H. Jamali, "The Modified Autocorrelation Technique for Parameter Estimation of Random FH Signals," *Proceedings of ICSP*, 1998, pp. 188-190.

[33] W. A. Gardner, "Spectral Correlation of Modulated Signals: Part I--Analog Modulation," *IEEE Transactions on Communications,* Vol. 35, 1987, pp. 584-594.

[34] W. A. Gardner, "Spectral Correlation of Modulated Signals: Part II—Digital Modulation," *IEEE Transactions on Communications,* Vol. 35, 1987, pp. 595-601.

[35] W. A. Gardner, "Exploitation of Spectral Redundancy in Cyclostationary Signals," *IEEE Signal Processing Magazine,* Vol. 8, 1991, pp. 14-36.

[36] R. S. Roberts, W. A. Brown, and H. H. Jr. Loomis, "Computationally Efficient Algorithms for Cyclic Spectral Analysis," *IEEE Signal Processing Magazine,* Vol. 8, 1991, pp. 38-49.

[37] S. W. Dahlgren, N. H. Younan, and B. J. Skiner, "Radar Signal Detection Via ARMA Modeling," *Proceedings of the Twenty-Seventh Symposium on System Theory,* 1995, pp. 436-440.

[38] W. P. McPherson, D. A. Hill, Mai Loc; and J. S. Wight, "Chip rate Hopping Counters Chip rate Detection of Direct Sequence Spread Spectrum Signals," *MILCOM*, 1997, pp. 1366-1371.

[39] E. Reed, and M. A. Wickert, "Spread Spectrum Signals with Low Probability of Chip rate Detection," *IEEE Journal on Selected Areas in Communication*, Vol 7., No. 4. 1989, pp. 595-601.

[40] C. Brown, K. Kowalske, and C. Robertson, "Detection of Frequency-Hopped Waveforms Embedded in Interference Waveforms," *IEEE MILCOM,* pp. 747-753, 2005.

[41] R. D. Strum, and D. E. Kirk, *First Principles of Discrete Systems and Digital Signal Processing,* Reading, MA., Addison-Wesley, 1989.

[42] A. Papoulis, and S. Pillai, *Probability, Random Variables and Stochastic Processes* 4th ed., Boston, MA., McGraw Hill, 2002.

[43] P. Z. Peebles, *Probability, Random Variables and Random Signal Principles*, 4th ed., New York, NY., McGraw-Hill, 2001.

[44] G. R. Cooper, and C. D. McGillem, *Probabilistic Methods of Signal and System Analysis*, 2nd ed., New York, NY., Holt, Rinehart and Winston, 1971.

[45] E. Lukacs, *Characteristic Functions,* 2nd ed. New York, NY., Hafner Publishing Company, 1970.

[46] A. Leon-Garcia, *Probability and Random Processes for Electrical Engineering,* 2nd ed., Reading, MA., Addison-Wesley, 1994.

[47] R. N. McDonough, and A. D. Whalen, *Detection of Signals in Noise,* 2nd ed., New York, NY., Academic Press, 1995.

[48] A. V. Oppenheim, R. W. Schafer, and J. R. Buck, *Discrete-Time Signal Processing,* 2nd ed. Upper Saddle River, NJ., 1999.

[49] G. James, and R. C. James, *Mathematics Dictionary*, Princeton, NJ., D. Van Nostrand, 1967.

[50] I. S. Gradshteyn, and I. M. Ryzhik, *Table of Intergrals, Series, and Products,* New York, NY., Academic Press, 1980.

[51] A. M. Law, and W. D. Kelton, *Simulation Modeling and Analysis,* New York, NY., McGraw Hill, 1982.

[52] R. B. D'Angostino, and M. A. Stephens, *Goodness-of-Fit Techniques,* New York, NY., Marcel Dekker, 1986.

[53] R. A. Tapia, and J. R. Thompson, *Nonparametric Probability Density Estimation*, Baltimore, MD., The Johns Hopkins University Press, 1978.

[54] B. W. Silverman, *Density Estimation for Statistics and Data Analysis,* New York, NY., Chapman and Hill, 1986.

[55] K. S. Shanmugan, and A. M. Breipohl, *Random Signals Detection, Estimation and Data Analysis*, New York, NY., John Wiley and Sons, 1988.

[56] Wikipedia, http://en.wikipedia.org/wiki/Histogram, last accessed 28 December 2006.

[57] H. Shimazaki, and S. Shinomoto, "A Recipe for Optimizing a Time-Histogram," *Neural Information Processing Systems*, Vol. 19, pp. 1-8, 2007. http://books.nips.cc/papers/files/nips19/NIPS2006_0137.pdf, last accessed 28 December 2006.

[58] D. E. Knuth, *The Art of Computer Programming* Vol. 2, 2nd ed., Reading, MA., Addison-Wesley, 1981.

[59] L. J. Glesser, and D. S. Moore, "The Effect of Dependence on Chi-Squared and Empiric Distribution Tests of Fit," *The Annals of Statistics*, Vol. 11, No. 4, 1983, pp. 1100-1108.

[60] D. S. Moore, "The Effect of Dependence on Chi-Squared Tests of Fit," *The Annals of Statistics*, Vol. 10, No. 4, 1982, pp. 1163-1171.

[61] T. D. Sterling, and S. V. Pollack, *Introduction to Statistical Data Processing*, Englewood Cliffs, NJ., Prentice-Hall, 1968.

[62] M. Abramowitz, and I. A. Stegun, *Handbook of Mathematical Functions*, Washington, D.C. U.S. Government Printing Office, 1964.

[63] F. J. Massey, "The Kolmogorov-Smirnov Test for Goodness-of-fit," *Journal of the American Statistical Association*, Vol. 46, 1951, pp. 68-78.

[64] M. Kac, J. Kiefer, and J. Wolfowitz, "On Tests of Normality and Other Tests of Goodness-of-fit Based on Distance Methods," *The Annals of Mathematical Statistics*, Vol. 26, 1955, pp. 189-211.

[65] H. W. Lilliefors, "On the Kolmogorov-Smirnov Test for Normality with Mean and Variance Unknown," *Journal of American Statistical Association*, Vol. 62 Issue 318, 1967, pp. 399-402.

[66] G. G. Judge, R. C. Hill, W. E. Griffiths, H. Lutkepohl, and T. Lee, *Introduction to the Theory and Practice of Econometrics*, 2nd ed., New York, NY., John Wiley & Sons, 1988.

[67] Wikipedia, http://en.wikipedia.org/wiki/Jarque-Bera_test, last accessed 28 December 2006.

[68] V. Rothschild, and N. Logothetis, *Probability Distributions*, New York, NY., John Wiley and Sons, 1986.

[69] F. H. Zuwaylif, *General Applied Statistics* 3rd ed., Reading, MA., Addison-Wesley Publishing Company, 1979.

[70] C. W. Therrien, *Digital Random Signals and Statistical Signal Processing.* Englewood Cliffs, NJ., Prentice Hall, 1992.

[71] A. Leon-Garcia, *Probability and Random Processes for Electrical Engineering*, 2nd ed., Reading, MA., Addison-Wesley, 1994.

[72] J. B. Weber, K. Kowalske, C. Robertson, F. Kragh and C. Brown, "Detection of Frequency-Hopped Waveforms Embedded in Interference Waveforms with Noise," *ICC*, accepted for publication, 2007.

[73] J. B. Weber, K. Kowalske, C. Robertson, and F. Kragh, "Performance of a Digital AD-hoc Chip Rate Estimator (ACRE) Given a Direct Sequence Spread Spectrum Pulse Shaped Signal," *IEEE MILCOM*, pp. CB, 2006.

INITIAL DISTRIBUTION LIST

1. Defense Technical Information Center
   Ft. Belvoir, Virginia

2. Dudley Knox Library
   Naval Postgraduate School
   Monterey, California

3. Chairman
   Department of Electrical and Computer Engineering
   Naval Postgraduate School
   Monterey, California

4. Prof. Clark Robertson
   Department of Electrical and Computer Engineering
   Naval Postgraduate School
   Monterey, California

5. Prof. David C. Jenn
   Department of Electrical and Computer Engineering
   Naval Postgraduate School
   Monterey, California

6. Prof. Monique P. Fargues
   Department of Electrical and Computer Engineering
   Naval Postgraduate School
   Monterey, California

7. Prof. Frank Kragh
   Department of Electrical and Computer Engineering
   Naval Postgraduate School
   Monterey, California

8. Prof. Carlos F. Borges
   Department of Mathematics
   Naval Postgraduate School
   Monterey, California

9. Dr. Kyle E. Kowalske
   Department of Defense
   Washington, D.C.

10. LT John Weber
United States Navy
Monterey, California